Simulations of Sawtoothing in the CTH Stellarator-Tokamak Hybrid

by

Nicholas A. Roberds

A dissertation submitted to the Graduate Faculty of
Auburn University
in partial fulfillment of the
requirements for the Degree of
Doctor of Philosophy

Auburn, Alabama
August 6, 2016

Keywords: Sawteeth, Simulation, Numerical, Tokamak, Stellarator

Approved by

James Hanson, Chair, Professor of Physics
David Maurer, Associate Professor of Physics
Luca Guazzotto, Associate Professor of Physics
Kaijun Liu, Assistant Professor of Physics

Abstract

Numerical extended MHD simulations are used to gain insight into the effect of three-dimensional shaping from the Compact Toroidal Hybrid (CTH) stellarator field on sawteeth. Numerical solutions having repeated sawtooth relaxations are obtained for a sequence of configurations with increasing helical stellarator field strength. The experimentally observed trend of the sawtooth period τ_{saw} decreasing as the helical field strength is increased is recovered in the simulations. The linear growth rate of the visco-resistive internal kink mode, which drives the sawteeth, increases as the helical field strength is increased.

The NIMROD code was used to compute the numerical solutions. Careful attention to numerical convergence was required to obtain accurate numerical solutions. Increased spatial resolution, especially in the toroidal direction, was required to resolve the reconnection current layer during relaxations for non-axisymmetric cases. Temporal convergence issues were identified and an improved semi-implicit operator, having better convergence properties for non-axisymmetric cases, was implemented. The numerical convergence considerations needed to obtain the results may be relevant to simulations of other phenomena in devices with non-axisymmetric plasmas such as perturbed tokamaks, RFPs and stellarators.

Experimental soft x-ray data of sawtooth relaxations was analyzed with computed tomography. A novel variation on the Fourier-Bessel method was used. The basis functions are functions of VMEC flux coordinates, so that known information about the structure of the magnetic field is used in the reconstructions.

Acknowledgments

I would like to thank my parents Brad and Stacy Roberds who supported and inspired me to study physics and work hard. I thank my wife Caroline for her love and support. I would also like to thank my sister Holly. This work would not have been possible without them. I owe my sincere gratitude to James Hanson, Luca Guazzotto and David Maurer for their expert advice and flexibility.

Table of Contents

List of Figures

List of Tables

Chapter 1

Introduction

When a gas is heated to a sufficiently high temperature, molecules break down and electrons dissociate from their atoms. A heated gas that has reached such a state is called a plasma. A useful property of plasmas is that they can be manipulated with magnetic fields. In a uniform magnetic field a single charged particle orbits a field line at the Larmor radius, which is inversely proportional to the strength of the field, but moves with constant velocity in the direction parallel to the field. Charged particles in a strongly magnetized plasma tend to travel parallel to field lines, so it is possible to confine a plasma to a region of space with magnetic fields. There are several exciting possibilities for technological application of magnetic plasma confinement in the future. This work is concerned with magnetically confined nuclear fusion [1], but another possible application is efficient space propulsion concepts like the VASIMR rocket [2]. Magnetic fusion involves confining a plasma to a region with magnetic fields and heating it until nuclear reactions occur because collisions between ions are energetic enough to overcome the Coulomb barrier. There are many concepts for producing plasmas with the properties needed for nuclear fusion and several fuels have been identified.

Most magnetically confined nuclear fusion concepts are based on a fuel that is a mixture of deuterium and tritium (DT), because the plasma conditions needed for DT reactions are the least severe. The fusion of a deuterium nucleus with a tritium nucleus produces an energetic alpha particle and neutron. A DT plasma with the right properties may reach an ignited state [3]. An ignited plasma is heated by high energy alpha particles produced from nuclear reactions, maintaining the high temperature necessary for continued nuclear reactions and alpha particle production without any external heating [1]. The high energy

neutrons, having no electric charge, escape the plasma. The neutrons may be thermalized and the energy used for some purpose like driving a steam turbine to produce electricity. The JET and TFTR experiments have successfully created conditions that resulted in several megawatts of fusion power [4,5]. However, experimental observation and study of an ignited, magnetically confined plasma is presently beyond the state of the art. The ITER experiment, currently under construction, is intended to study strongly self-heated plasmas. It is a possiblility that ITER may reach ignited DT plasma conditions [6].

Two successful concepts, the tokamak and the stellarator, emerged from the early work on magnetic fusion energy (MFE). Presently the tokamak is the most evolved concept for magnetically confined fusion, but progress continues on stellarators. In contrast to earlier cylindrical pinch concepts, tokamaks and stellarators are both topologically toroidal. A simple toroidal coordinate system, (r, θ, ϕ) where r is the radial coordinate, θ poloidal and ϕ toroidal, is commonly used to study these devices. The transformation equations for these coordinates are

$$\begin{aligned} r &= \sqrt{(R - R_0)^2 + (Z - Z_0)^2} \\ tan(\theta) &= \frac{Z - Z_0}{R - R_0} \\ tan(\phi) &= \frac{y}{x}, \end{aligned} \tag{1.1}$$

where R, Z, ϕ are cylindrical coordinates, x, y, z are Cartesian coordinates and R_0, Z_0 are constants, which are often chosen to be the location of the magnetic axis in cylindrical coordinates. This coordinate system is distinct from proper toroidal coordinates in which Laplace's equation is separable.

The magnetic field of both the tokamak and the stellarator is in the toroidal direction with a weak poloidal component and they differ principally in how the poloidal component of the magnetic field is generated [7]. In tokamaks, the poloidal component is produced by driving an electric current the long way around the torus. There are a number of ways to drive this current but the most ubiquitous way is by magnetic induction using a transformer coil in the middle of the torus. A stellarator produces the poloidal field with carefully shaped

magnet coils that surround the vacuum vessel. Often a helically deformed vacuum vessel is needed in stellarators. It follows that the tokamak is traditionally axisymmetric, having no variations in the toroidal direction, while the stellarator is necessarily non-axisymmetric.

Sawtoothing is a commonly observed phenomenon in tokamaks, first reported in [8]. It is a repeated relaxation in the core of the plasma that effectively limits the amplitude of the current density. The relaxations are called sawteeth because a soft x-ray pinhole camera pointed toward the plasma core during sawtooth activity will produce a sawtooth-like signal. It is worthwhile to note that another type of repeated relaxation, called an edge localized mode (ELM), is seen in tokamaks. ELMs effectively limit the pressure gradient at the edge of the plasma. The first numerical simulation of repeated ELM relaxations was only conducted recently [9].

It has been found that two-dimensional shaping in the poloidal plane ($\phi = const.$) of the plasma in tokamaks can be used to control a number of properties of a plasma discharge. Two-dimensional shaping has been used to control the properties of sawtoothing in several experiments including TCV and DIII-D [10, 11]. It was also found that confinement of thermal energy in TCV and DIII-D can be optimized with two-dimensional shaping [12, 13]. More recently control coils with non-axisymmetric fields have proven useful in controlling ELMs [14].

Consideration of three-dimensional equilibrium shaping in tokamak design would allow many more degrees of freedom than are possible if axisymmetry is required. This flexibility may prove valuable in finding solutions to future challenges [15]. The NCSX [16] design study considered a quasiaxisymmetric stellarator with a significant amount of toroidal plasma current generated by the bootstrap effect. The design was optimized with the effect of the plasma current included in the optimization. Although NCSX is usually referred to as a compact stellarator, it can also be accurately described as a quasiaxisymmetric tokamak [15]. The Compact Toroidal Hybrid (CTH) [17] is a small stellarator-tokamak hybrid at Auburn

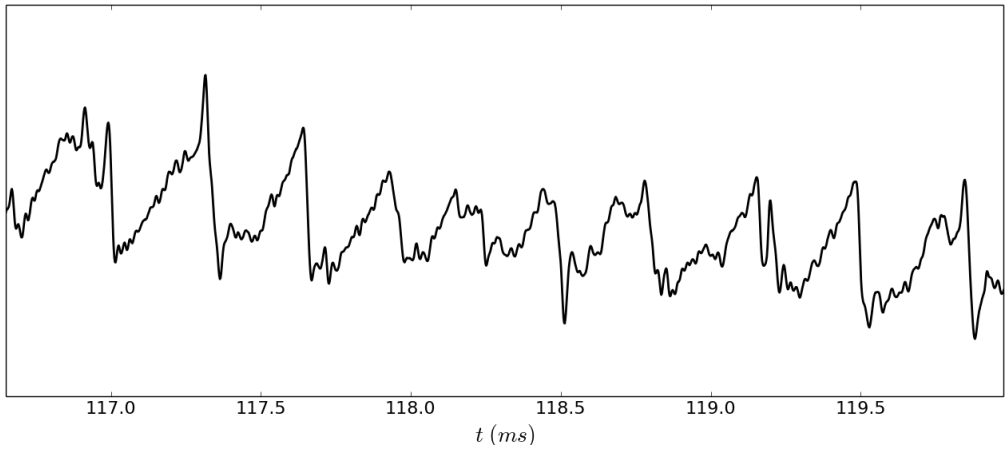

Figure 1.1: Signal from central chord of a CTH soft x-ray camera, shot 14110630. Sawteeth can be clearly seen.

University. Most recent studies on CTH consider regimes of operation that are more accurately described as tokamak-stellarator hybrid operation, where tokamak-like phenomena in the plasma are studied. Several CTH publications have reported on ways of controlling the behavior of tokamak-like phenomena such as disruptions and vertical displacement events by using shaping from the CTH stellarator field [18–20].

Although sawtoothing is typically associated with tokamaks, it has long been known that sawteeth can be observed in current carrying stellarators under certain conditions. For example, sawtoothing has been reported in the W7-AS, Heliotron E and L-2 stellarators [21–23]. Sawtoothing is often seen in CTH. A soft x-ray signal from CTH is shown in Fig. 1.1 and sawteeth can be clearly seen. In CTH, three-dimensional shaping from the helical stellarator magnet coil can be used to control the properties of sawteeth.

In this work, the effect of three-dimensional shaping from CTH's stellarator magnet coil on sawteeth is studied with numerical solutions to a set of extended magnetohydrodynamic (MHD) equations. In the remainder of chapter 1, theory and history relevant to the task at hand are introduced. The NIMROD code [24] is used to compute the numerical solutions. In chapter 2 the model equations to be solved and the numerical methods used by NIMROD are introduced. Experimental observations are briefly discussed in chapter 3 and in chapter 4 we

go on a slight digression to introduce a novel method of tomographic emissivity reconstruction. Experimental soft x-ray signals are reconstructed to provide insight into the dynamics of sawtoothing in CTH. In chapter 5, MHD solutions of repeated sawtooth relaxations in a CTH-like tokamak, and some key challenges in obtaining these solutions, are described. Then MHD simulations of sawteeth in CTH stellarator-tokamak hybrid configurations are considered in chapter 6. The effect of the helical stellarator field on the sawtoothing is studied by considering at a sequence of configurations having increasing strength of stellarator field. Some of the experimentally observed trends are captured by the solutions. Numerical convergence issues in obtaining the solutions are discussed. The numerical convergence properties of the non-axisymmetric hybrid configurations were different from the axisymmetric tokamak configuration. The discussion of numerical convergence may be relevant to other NIMROD simulations of non-axisymmetric configurations. The convergence challenges motivated an improvement to NIMROD's numerical method by including non-axisymmetric fields in the semi-implicit operator.

1.1 Basic Tokamak and Stellarator Concepts

In magnetic fusion, the structure of the magnetic fields is the single most important aspect of confinement. The efficiency with which a configuration confines thermal energy is quantified with the energy confinement time τ_E. It is computed during thermal equilibrium by taking the ratio of the total thermal energy E_{th} over the total heating power Q,

$$\tau_E = \frac{E_{th}}{\int_V Q \; dV}. \tag{1.2}$$

The field of energy and particle transport in magnetized plasmas is extensive and many of the most important frontiers in magnetic fusion research are presently in this field. The starting point is often to describe the plasma in terms of a distribution function $f(\vec{r}, \vec{v}, t)$ that evolves according to the Boltzmann transport equation [25]. This approach of solving

a partial differential equation (PDE) with seven independent variables is usually intractable and reduced models such as the gyrokinetic model are often used [26]. However, in some cases the very simple single particle view can be extremely useful. In this model the hot magnetized plasma is considered to be a collection of non-interacting charged particles. The path of the guiding center of a particle, over which the high frequency Larmor gyration of the particle is averaged out, is computed.

Consider, in cylindrical coordinates, a toroidal configuration like a tokamak or a stellarator. The center of the torus is at $R = Z = 0$ and the axis of the torus is given by $R, Z = R_0, 0$. A toroidal magnetic field, $\vec{B} = \mu_0 I/(2\pi R)\hat{\phi}$ may be generated by a wire with current I along the line $R = 0$. Although the guiding centers of charged particles follow field lines in a uniform magnetic field, the guiding centers will drift across field lines in an inhomogeneous magnetic field. Particle drifts arise in inhomogeneous fields due to the finite Larmor radius that particles orbit field lines with. This toroidal magnetic field will not provide good particle and energy confinement because of guiding center drifts. The solution to this problem is to add a poloidal component to the fields so that particles revolve between the inboard and outboard sides of the device as their guiding centers follow the field line. Particle drift motion across field lines, which is quite slow compared to the motion along the field lines, averages out and confinement is greatly enhanced.

The amount of twist the fields have due to the poloidal field is quantified with the rotational transform ι and its inverse, the safety factor q,

$$\begin{aligned} \iota &= \frac{\Delta\theta}{2\pi} \\ q &= \frac{1}{\iota}, \end{aligned} \tag{1.3}$$

where $\Delta\theta$ is the poloidal angle traveled by the field line in one toroidal revolution. A $q = 2$ fieldline in a tokamak is illustrated in Fig. 1.2. Typically, the rotational transform is used in discussions about stellarators and the safety factor in discussions about tokamaks.

Figure 1.2: A magnetic field line (black) makes a poloidal revolution every two toroidal revolutions ($q = 2$) due to the poloidal field from a toroidal plasma current (blue).

In a stellarator, $\iota(r)$ generally increases monotonically with r and in a tokamak $\iota(r)$ decreases with increasing r as suggested by Fig. 1.3. The shape of $\iota(r)$ is important for the stability of a confined plasma. To see this, one can consider a cylindrical plasma with a circular cross section as a conducting fluid with the magnetohydrodynamic (MHD) model. A periodic cylinder geometry is often used instead of toroidal geometry as an approximation, and in these cases a polar cylindrical coordinate system is used (r, θ, z) where z is the axial coordinate. For such a plasma, all equilibrium quantities are only a function of the radial coordinate r. A stability analysis gives the following criterion called Suydam's criterion,

$$p^{'} + \frac{rB_z^2}{8}\left(\frac{\iota^{'}}{\iota}\right)^2 > 0, \tag{1.4}$$

where $^{'}$ denotes differentiation. A cylindrical MHD equilibrium that does not satisfy Suydam's criterion everywhere will have unstable interchange modes. The radial gradient of the pressure $p^{'}$, which is typically negative, is destabilizing while the shear $\iota^{'}$ is stabilizing. This criterion has been generalized to toroidal geometry by Mercier, where unstable ballooning modes will be present if Mercier's criterion is not meet. In a tokamak this situation usually leads to a disruption and termination of the discharge [27]. The limit on radial pressure gradient in a stellarator is somewhat higher than that given by an MHD model and the consequences for exceeding the limit is not as disastrous as in a tokamak [7]. Stellarators are generally less susceptible to instabilities and disruptions than tokamaks.

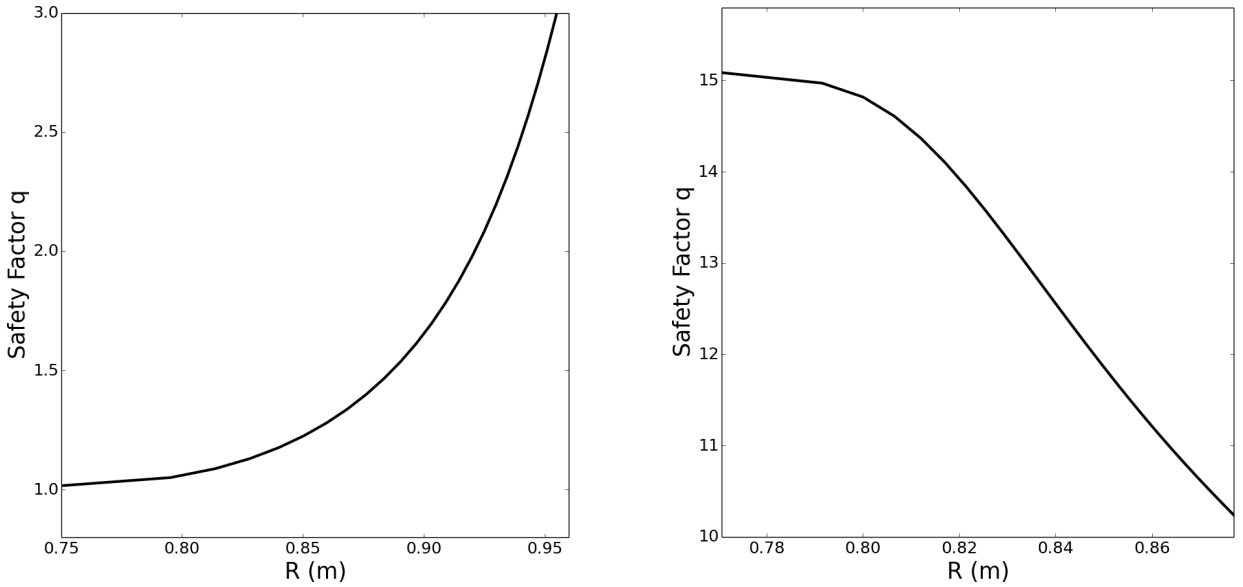

(a) Tokamak (b) Stellarator

Figure 1.3: Safety factor profiles for a tokamak (left) and stellarator (right) are plotted along a chord going from the center to the edge of the plasma. These particular tokamak and stellarator profiles come from equilibria computed using CTH magnet coils.

The volume inside tokamaks and stellarators may be broken up into regions where the magnetic field has different structural properties. Magnetic fields may form closed, nested flux surfaces, where field lines trace out toroidal tubular surfaces (flux tubes) that surround the magnetic axis at the center of the plasma. Regions of closed nested flux surfaces are generally associated with good energy and particle confinement. Field lines may trace out surfaces that bifurcate and enclose volumes containing nested flux surfaces. These regions of nested flux surfaces do not enclose the magnetic axis and are called islands. There may also be regions of stochasticity, where field lines do not conform to flux tubes at all and instead fill the entire stochastic region. Due to the rapid motion of hot plasma particles parallel to field lines, heat transport is enhanced across islands and stochastic regions.

1.2 Magnetohydrodynamics

It is often productive to describe tokamak or stellarator plasmas with a fluid model. Fluid equations may be rigorously obtained from first principles by defining velocity moments

of the Boltzmann particle distribution function $f(\vec{r}, \vec{v}, t)$ and then obtaining equations that describe the evolution of these moments by integrating the Boltzmann transport equation. Usually, only equations for the first two or three moments are obtained. Then a set of closure relations, which describe higher moments appearing in the equations in terms of the first few, are chosen to get a closed set of equations. If an exact closure is used, the fluid equations will describe the exact evolution of the moments.

The simplest fluid model for fusion plasmas is ideal MHD [28]. Ideal MHD describes a single, inviscid, perfectly conducting fluid. Interestingly, some of the approximations made in arriving at the ideal MHD equations from the Boltzmann equation are not valid for fusion plasmas. One approximation is that of high collisionallity. Plasma particles must have a short mean free path length compared to the length scales of interest. Tokamak and stellarator plasmas are highly collisionless and particles can have mean free paths of several kilometers. Nevertheless, ideal MHD gives qualitatively correct descriptions of some tokamak phenomena. This is because the small gyroradius size of tokamak plasma particles leads to localization in the direction perpendicular to field lines, so that the plasma has a collisional-like behavior in the perpendicular direction [29].

One may arrive at the equations of ideal MHD by postulating them as a set of conservation laws instead of starting with the Boltzmann equation in the process summarized above:

$$\begin{aligned}
\frac{\partial \rho}{\partial t} + \nabla \cdot (\rho \vec{V}) &= 0 && Conservation\ of\ Mass \\
\rho(\frac{\partial \vec{V}}{\partial t} + (\vec{V} \cdot \nabla)\vec{V}) + \nabla p - \frac{\nabla \times \vec{B} \times \vec{B}}{\mu_0} &= 0 && Conservation\ of\ Momentum \\
\frac{\partial p}{\partial t} + \vec{V} \cdot \nabla p + \frac{5p}{3} \nabla \cdot \vec{V} &= 0 && Conservation\ of\ Entropy \\
\frac{\partial \vec{B}}{\partial t} - \nabla \times (\vec{V} \times \vec{B}) &= 0 && Conservation\ of\ Magnetic\ Flux \\
\nabla \cdot \vec{B} &= 0.
\end{aligned} \tag{1.5}$$

Conservation of flux is an essential feature of ideal MHD. The flux through a surface S that is co-moving with the fluid, $\int_S \vec{B} \cdot \hat{n}\, dS$, remains constant. It follows from this that the magnetic field lines are "frozen in" to the plasma. The motion of magnetic field lines follows the fluid motion of the plasma exactly. Because of the frozen in field property, it makes sense to show plots derived from the magnetic fields, such as Poincaré plots, when discussing the fluid displacement of the plasma. A consequence of the frozen in property is that the topology of the magnetic field lines cannot change during the evolution of the plasma.

More complicated fluid equations than ideal MHD may be needed to describe certain phenomena such as sawtoothing. For example, the generalized Ohm's law of ideal MHD is $\vec{E} = -\vec{V} \times \vec{B}$. An additional term is often added to Ohm's law to account for finite resistivity. In the ideal MHD model a simple adiabatic closure for the heat flux, $\vec{q} = 0$, is used so that entropy is conserved. However it is sometimes necessary to choose a heat flux closure that incorporates some information about the dynamics of the plasma parallel to the magnetic field. Two-fluid models are sometimes needed where the electron and ion species are described with two separate, interacting fluids.

1.3 MHD Equilibrium

The global configuration of tokamak and stellarator plasmas is usually quite accurately described by equilibrium solutions to the ideal MHD equations. Computer programs like EFIT [30] and V3FIT [31] exist to find the MHD equilibrium that best matches data from experimental sensors. If an ideal plasma is in static equilibrium, we have $\vec{V} \to 0$, $\partial/\partial t \to 0$ and the equations for static equilibrium are obtained by substituting these facts into the equations of ideal MHD:

$$\begin{aligned} \nabla p &= \vec{J} \times \vec{B} \\ \nabla \times \vec{B} &= \mu_0 \vec{J} \\ \nabla \cdot \vec{B} &= 0. \end{aligned} \tag{1.6}$$

Note that the condition of an equilibrium being static with $\vec{V} = 0$ is usually just a simplifying assumption and there exist dynamic equilibria with $\vec{V} \neq 0$.

Due to the magnetic divergence equation, an axisymmetric equilibrium must have nested flux surfaces everywhere with no islands or regions of stochasticity. Axisymmetric ideal equilibria may be efficiently computed by numerically solving the Grad-Shafranov equation. Obtaining three-dimensional (3D) equilibria however, is more difficult. A 3D equilibrium will, in general, have magnetic islands and regions of magnetic stochasticity as well as nested flux surfaces. In this work, we make use of the ideal MHD three-dimensional equilibrium code VMEC [32]. VMEC assumes that equilibria have nested flux surfaces, which is not a bad approximation in many cases of interest. More complete 3D equilibrium codes are available that allow changes in the magnetic topology, but these often use VMEC equilibria as a starting point.

1.4 Linearized MHD

To find the waves and instabilities of an equilibrium, the evolution of small perturbations to the equilibrium fields must be considered

$$\begin{aligned} \vec{V}(\vec{r},t) &= \vec{V}_1(\vec{r},t) \\ \vec{B}(\vec{r},t) &= \vec{B}_0(\vec{r}) + \vec{B}_1(\vec{r},t) \\ p(\vec{r},t) &= p_0(\vec{r}) + p_1(\vec{r},t) \\ \rho(\vec{r},t) &= \rho_0(\vec{r}) + \rho_1(\vec{r},t). \end{aligned} \tag{1.7}$$

The equilibrium fields are denoted with a 0 subscript and perturbed fields with a 1 subscript. These expressions are substituted into Eq. 1.5, and then Eqs. 1.6 are invoked. Terms of second order in the perturbation are eliminated because they are vanishingly small. This

process yields the following linearized equations of MHD,

$$\begin{aligned}
\rho_0 \frac{\partial \vec{V}_1}{\partial t} &= -\nabla p_1 + \vec{J}_0 \times \vec{B}_1 + \vec{J}_1 \times \vec{B}_0 \\
\frac{\partial \vec{B}_1}{\partial t} &= \nabla \times (\vec{V}_1 \times \vec{B}_0) \\
\frac{\partial p_1}{\partial t} &= -\vec{V}_1 \cdot \nabla p_0 - \frac{5p_0}{3} \nabla \cdot \vec{V}_1 \\
\frac{\partial \rho_1}{\partial t} &= -\nabla \cdot (\rho_0 \vec{V}_1) \\
\vec{J}_1 &= \nabla \times \vec{B}_1 \\
\nabla \cdot \vec{B}_1 &= 0.
\end{aligned} \tag{1.8}$$

Eigenfunctions and eigenvalues of the linearized MHD equations can be obtained given an equilibrium and the boundary conditions. To this end, one often seeks to "uncouple" the momentum equation from the other equations, so that only $\vec{V}_1$ appears. After one solves for $\vec{V}_1$, the other perturbed quantities can be easily computed [25]. This may be accomplished by first differentiating both sides of the momentum equation,

$$\frac{\partial^2 \vec{V}_1}{\partial t^2} = \frac{1}{\mu_0 \rho_0} \Big[(\nabla \times \frac{\partial \vec{B}_1}{\partial t}) \times \vec{B}_0 - \frac{\partial \vec{B}_1}{\partial t} \times (\nabla \times \vec{B}_0) - \mu_0 \nabla \frac{\partial p_1}{\partial t} \Big]. \tag{1.9}$$

Now invoke Eq. 1.8 to express occurrences of $\partial \vec{B}_1/\partial t$, $\partial p_1/\partial t$ and $\partial \rho_1/\partial t$ in terms of v_1. The result is the following decoupled velocity equation, which will be of interest later in this work

$$\begin{aligned}
\frac{\partial^2 \vec{V}_1}{\partial t^2} = \frac{1}{\mu_0 \rho_0} \Big[\vec{B}_0 \times \nabla \times \nabla \times (\vec{B}_0 \times \vec{V}_1) - (\nabla \times \vec{B}_0) \times \nabla \times (\vec{B}_0 \times \vec{V}_1) + \\
\mu_0 \nabla (\vec{V}_1 \cdot \nabla p_0) + \mu_0 \nabla (\frac{5p_0}{3} \nabla \cdot \vec{V}_1) \Big].
\end{aligned} \tag{1.10}$$

If $\vec{V}_1(\vec{x}, t)$ is an eigenfunction then $\dfrac{\partial^2 \vec{V}_1}{\partial t^2} = -\omega^2 \vec{V}_1(\vec{x}, t)$. When ω is real-valued, $\vec{V}_1(\vec{x}, t)$ is said to be a wave having frequency ω. An eigenfunction with a complex-valued frequency with a positive imaginary part, $\omega = \omega_r + i\gamma$, grows in amplitude exponentially with time and

is said to be an instability with growth rate γ. If an equilibrium has at least one unstable eigenfunction the equilibrium is said to be unstable.

Familiarity with the waves of ideal MHD in a uniform equilibrium is essential for work concerning numerical calculations in MHD. Given uniform and constant equilibrium fields $\vec{B}_0$, p_0, ρ_0 and $\vec{V}_0 = 0$, there are three distinct types of MHD waves. Each type of wave has a different dispersion relation. The phase speeds of these waves is strongly dependent on the angle the wave vector $\vec{k}$ makes with the equilibrium magnetic field. The sound wave and the Alfvén wave propagate fastest in the direction of $\vec{B}_0$ with parallel phase speeds of $v_{s,\parallel}$ and $v_{A,\parallel}$ respectively. The fast wave propagates fastest in the direction perpendicular to $\vec{B}_0$ with perpendicular phase speed $v_{f,\perp}$. Expressions for these phase speeds given by

$$\begin{aligned} v_{s,\parallel} &= \sqrt{\frac{5p_0}{3\rho_0}} \\ v_{A,\parallel} &= \frac{B_0}{\sqrt{\mu_0\rho_0}} \\ v_{f,\perp} &= \sqrt{v_{A,\parallel}^2 + v_{s,\parallel}^2}. \end{aligned} \tag{1.11}$$

1.4.1 Instabilities

Instabilities are possible when the equilibrium is inhomogeneous in space. They can be thought of as waves with an imaginary component in the frequency so that they grow in amplitude exponentially with increasing time. Magnetic or thermodynamic energy is taken from the equilibrium and converted to kinetic energy as the instability grows. It should be noted that in tokamaks and stellarators, instabilities are usually nearly incompressible in the poloidal plane with $\nabla_\perp \cdot \vec{V}_1 \approx 0$. In these devices, the toroidal magnetic field is dominant and a large amount of energy is needed to compress toroidal field lines [33].

When the condition that the plasma be perfectly conducting is relaxed, and non-zero plasma resistivity η is allowed, new types of unstable eigenfunctions may exist in the equilibrium. An equilibrium which is ideally stable or only weakly unstable may be resistively unstable. Sawteeth and disruptions are often driven by resistive modes. When resistivity is

included it is assumed to be very small so that it only needs to be considered in the thin region around the resonant surface.

A vast amount of early work has been done in investigating the ideal and resistive MHD stability of simple, parameterized equilibrium profiles in a periodic cylinder geometry. Analytic and semi-analytic study of these idealized cases can be very tedious and can be found in the literature. There will not be a detailed discussion of them here. However, a brief discussion of some key results and considerations is in order.

When speaking of instabilities in tokamaks, it is common to refer to the poloidal and toroidal "mode numbers" denoted m and n respectively. This follows from the fact that in a periodic cylinder geometry, which is meant to approximate a very low aspect ratio torus, an equilibrium with circular flux surfaces has eigenmodes with the form $\vec{V}_1 = \hat{\vec{V}}_1(r,t)e^{i(\gamma t + m\theta - n\phi)}$. When a toroidal geometry or non-circular equilibrium flux surfaces are considered, the complex valued eigenfunction $\hat{\vec{V}}_1$ will have a spatial dependence on both r and θ, and the mode will not be characterized by a definite value of m. In this work, as we will see later, modes will not be characterized by a definite value of n when there is three-dimensional shaping of the equilibrium.

Another thing commonly mentioned regarding unstable modes in a tokamak is the resonant surface of a mode. The resonant surface is a surface on which $F = \vec{k} \cdot \vec{B} = 0$. In the straight tokamak approximation, this condition can be written as follows,

$$F = \frac{nqB_z}{R_0}\left(q + \frac{m}{n}\right) = 0, \tag{1.12}$$

where B_z is the axial field. The resonant surface of a mode with m, n is therefore a flux tube having the value of the safety factor $q = -m/n$ located at minor radius r_s. One way to explain the significance of the resonant surface is to note that solving the eigenfunction problem for a circular straight tokamak comes down to solving an ordinary differential equation (ODE).

The ODE will have a singular point at $r = r_s$. One can consult Goedbloed [34] for a very thorough introduction to one-dimensional ideal MHD stability.

Internal Instability with $m = 1$

The $m = 1$ internal kink instability is often implicated in driving sawtooth relaxations. The eigenfunction represents a rigid displacement of the plasma column inside $q = 1$ with a $n = 1$ toroidal variation in the direction of displacement. Early analytical work using a simple resistive MHD model with a periodic cylinder geometry recovered three distinct regimes of the $m = 1$ mode; the ideal internal kink, the resistive internal kink and the $m = 1$ resistive tearing mode [35]. The shapes of the eigenfunctions for these instabilities differ in a thin region around the resonant surface at $q = 1$. The scaling of growth rates with the Lundquist number S also differ across these regimes, where S is the ratio of the characteristic Alfvén transit time over the characteristic resistive diffusion time,

$$S = \sqrt{\frac{\mu_0}{\rho_0}} \frac{B_0 a^2}{\eta R}. \tag{1.13}$$

While the ideal internal kink growth rate is independent of S, the resistive internal kink has a growth rate $\gamma \propto S^{-1/3}$ and the $m = 1$ resistive tearing mode has a growth rate $\gamma \propto S^{-3/5}$. In [36] the $m = 1$ tearing mode instability was discovered and a dispersion relation for the $m = 1$ instability was derived that gives the ideal, resistive and tearing growth rates in the appropriate limits.

It was seen by Hastie [37] that in a toroidal geometry the $m = 1$ mode transitions from a resistive internal kink like mode to a tearing like mode at large S. This was also seen in the course of the present work. In Fig. 1.4 a resistive internal kink like eigenfunction at $S = 10^5$ and an $m = 1$ tearing like eigenfunction at $S = 10^7$ are pictured. The pictured eigenfunctions were computed by NIMROD, for the same equilibrium, in a CTH-like axisymmetric tokamak. Besides having a different scaling for γ vs. S, the resistive internal kink eigenfunction has

an interchange parity and the tearing mode has a tearing parity. A brief and enlightening explanation of the parity of resistive linear modes can be found in [38]. If the resistive solution for $V_{1,r}$ that is matched to the ideal solutions outside the resonant layer is an even function (in the coordinate system with $x = 0$ in the middle of the resonant layer), the mode is said to have interchange parity, and if it is an odd function the mode is said to have tearing parity.

Tearing and Ideal External Kink Instabilities with $m > 1$

Tokamaks are susceptible to ideal external kink modes and resistive tearing modes. These modes are driven by gradients in the toroidal plasma current and their non-linear evolution and interaction can lead to major disruptions of the plasma confinement [39]. They are sometimes referred to as global modes because their eigenfunctions are not well localized to the vicinity of the resonant surface $q = m/n$, and their stability criteria and growth rates depend on the overall profile shape not just the conditions at the resonant surface. The ideal external kink arises in an ideal MHD analysis of the tokamak in which there is a non-conducting vacuum region surrounding the plasma and the resonant surface $q = m/n$ is located in this vacuum region. Tearing modes arise in a resistive MHD analysis of the tokamak when the resonant surface $q = m/n$ is located inside the plasma.

In [40] there are several graphs showing the stability of equilibria having a parameterized toroidal current density profile $J = J_0(1 - (r^2/a^2))^\nu$. Broad, square-like, current density profiles are generally more susceptible to both tearing and kink instabilities than peaked profiles. The result is of interest in the problem at hand as sawtooth relaxations tend to broaden the current profile.

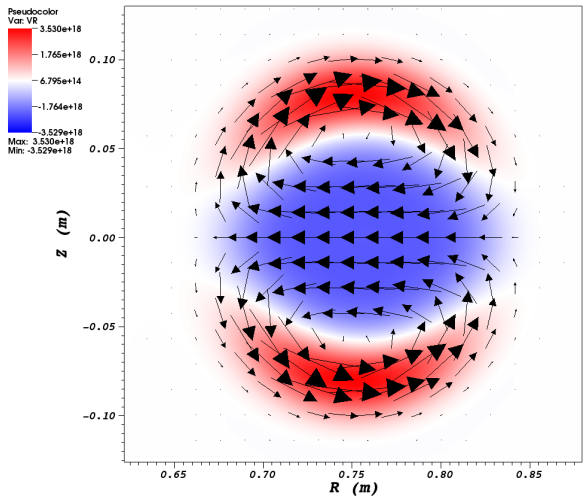

(a) Resistive kink, $S = 10^5$

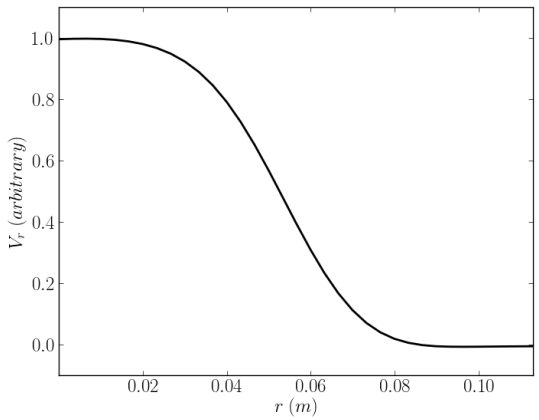

(b) Resistive kink, $S = 10^5$

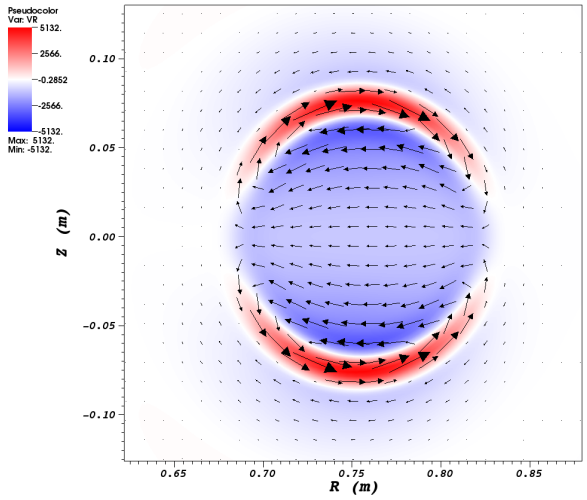

(c) Tearing, $S = 10^7$

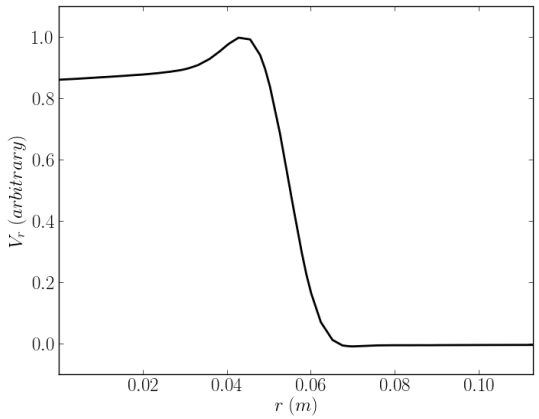

(d) Tearing, $S = 10^7$

Figure 1.4: As S is increased, the character of the unstable $m = 1$ mode transitions from a resistive internal kink to a tearing mode. In (a) and (c), the perturbed flow $\vec{V}_1$ computed by NIMROD is shown for a CTH-like tokamak, with color indicating the magnitude of the R component. In (b) and (d), the radial component of the flow is plotted along a chord running from the magnetic axis towards the inboard side of the torus.

1.5 Magnetic Reconnection

In a perfectly conducting solid, magnetic fields are frozen in the material for all time. This is evident when we consider Faraday's law and Ohm's law in the center of mass frame,

$$\begin{aligned} \vec{E} &= \eta \vec{J} = 0 \\ \frac{\partial \vec{B}}{\partial t} &= -\nabla \times \vec{E} = 0. \end{aligned} \tag{1.14}$$

If non-zero resistivity is allowed, diffusion of the magnetic fields will occur. That a diffusion equation describes the evolution of the magnetic field can be seen by also considering Ampere's Law,

$$\begin{aligned} \nabla \times \nabla \times \vec{B} = -\nabla^2 \vec{B} &= \mu_0 \nabla \times \vec{J} \\ \frac{\partial \vec{B}}{\partial t} &= -\eta \nabla \times \vec{J} \\ \frac{\partial \vec{B}}{\partial t} &= \frac{\eta \nabla^2 \vec{B}}{\mu_0}. \end{aligned} \tag{1.15}$$

We can figure an approximate timescale τ_r on which this process occurs in the conductor,

$$\begin{aligned} \frac{\partial}{\partial t} \rightarrow \frac{1}{\tau_r},\ \nabla\times \rightarrow \frac{1}{L} \\ \tau_r = \frac{\mu_0 L^2}{\eta}. \end{aligned} \tag{1.16}$$

Now consider, instead, a perfectly conducting fluid. In this case, magnetic field lines are constrained to move with the fluid. Field lines may only deform continuously, so that the topology of the magnetic structure is frozen for all time. From the study of fluids, it is well known that viscous flows have a general tendency to develop vortices. In MHD, there is a general tendency for flows in a conducting fluid to form discontinuities in the magnetic field along sheet like structures. When small, non-zero resistivity is allowed, these lead to localized regions of intense current density where field line breaking and "reconnection" occurs. This phenomenon is called reconnection and allows reorganization of the magnetic topology in a highly conducting fluid much faster than the characteristic diffusion time τ_r. In this work,

we are interested in "spontaneous reconnection", in which the fluid motions that lead to formation of current sheets and reconnection are driven by internal instabilities. It should be noted that both the ideal and resistive $m = 1$ instabilities may drive reconnection [41].

The classical model for studying the resistive saturation of a current sheet is the Sweet-Parker model [42]. Pictured in Fig. 1.5 is a reconnection layer of length $2L$ and width 2δ. The inflow and outflow velocities are u_0 and v_0 respectively and the strength of the magnetic field in the inflow region, which is oppositely sheared on either side of the reconnection layer, is B_0.

Because this work involves the numerical simulation of reconnection, it will be of interest to see how the dimensions of the Sweet-Parker current sheet depend on the plasma parameters and to obtain a time-scale on which the reconnection occurs. First we must obtain some relations between the quantities that describe the current sheet. By considering Ohm's law,

$$\vec{E} = -\vec{V} \times \vec{B} + \eta \vec{J}, \tag{1.17}$$

we see that there is an electric field pointing out of the paper in Fig. 1.5. Outside of the current sheet we have $\vec{J} = 0$, while at the center of the current sheet we must have $\vec{V} = 0$ by symmetry. This gives relations for the electric field outside the current sheet and at the center of the current sheet,

$$\begin{aligned} E_{outside} &= u_0 B_0 \\ E_{center} &= \eta j_{center}. \end{aligned} \tag{1.18}$$

Now consider Faraday's law. Because the current sheet is stationary, the electric field must have a constant value everywhere giving

$$u_0 B_0 = \eta j_{center}. \tag{1.19}$$

Furthermore, by using $\nabla\times \rightarrow \frac{1}{\delta}$ in Ampere's law we have

$$\frac{B_0}{\mu_0 \delta} \approx j_{center}. \tag{1.20}$$

From Eq. 1.19 and Eq. 1.20 we obtain an expression for the inflow velocity in terms of current sheet parameters,

$$u_0 = \frac{\eta}{\mu_0 \delta}. \tag{1.21}$$

Now from conservation of mass we must have,

$$u_0 L = v_0 \delta. \tag{1.22}$$

And from conservation of energy we have,

$$\frac{\rho v_0^2}{2} = \frac{B_0^2}{2\mu_0}. \tag{1.23}$$

The outflow velocity v_0 is therefore equal to the upstream Alfvén speed u_A,

$$v_0 = \frac{B_0}{\sqrt{\mu_0 \rho}} \equiv u_A. \tag{1.24}$$

Using equations 1.21, 1.22 and 1.24 the Sweet-Parker reconnection rate M can be found

$$\begin{aligned} M &\equiv \frac{u_0}{v_0} \\ &= \sqrt{\frac{\eta}{\mu_0 L u_A}} \quad = \sqrt{\frac{1}{S}}. \end{aligned} \tag{1.25}$$

The $\sqrt{1/S}$ scaling for reconnection leads to a much faster process at large S compared to the $1/S$ scaling for resistive diffusion.

Also consider the inverse aspect ratio of a Sweet-Parker sheet $A = L/\delta$. From Eq. 1.22 and Eq. 1.25 we have $A = \sqrt{S}$. As the Lundquist number increases, the current sheet

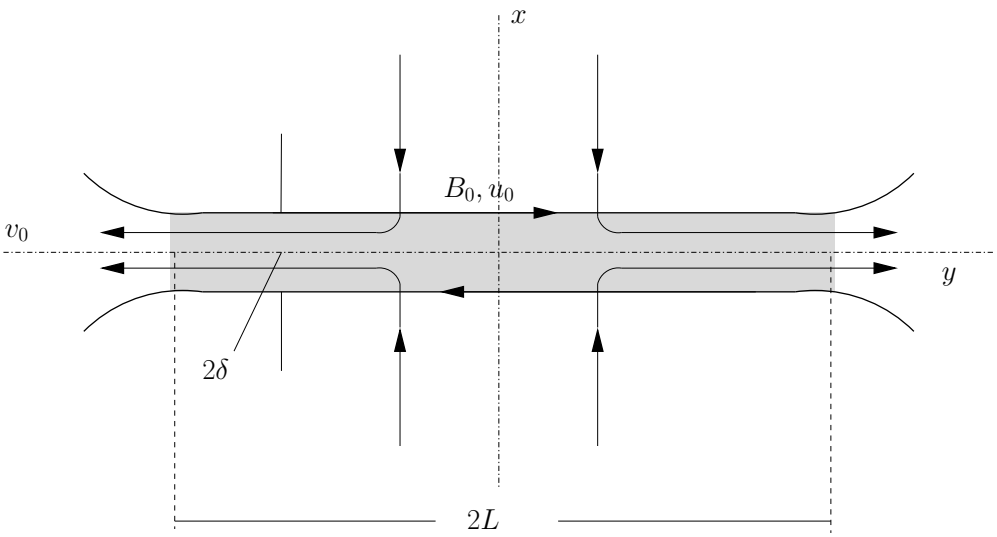

Figure 1.5: Sweet-Parker reconnection current sheet, characterized by width δ, length L, inflow velocity and upstream magnetic field u_0, B_0 and outflow velocity v_0

becomes more nearly singular. An important consequence of this is that simulations of plasmas with higher Lundquist numbers require a higher spatial resolution to resolve a reconnection event.

1.6 Sawteeth

Sawtooth relaxations, sometimes called crashes, or their absence affects the operation of tokamaks in several ways. The relaxations quickly eject thermal energy and particles inside the mixing radius into the outer region of the plasma. The ejected energy then diffuses outward to the plasma edge. This affects the energy and particle confinement of the configuration, and a larger mixing radius implies a more badly degraded confinement.

Sawtoothing can play an important role in determining tokamak profile shapes and the regions of parameter space that permit disruption free operation. Current density profiles that have a broad square-like shape, with a large flat region in the middle and steep gradients at the edge, tend to be more unstable to global MHD kink and tearing modes. Sawtooth relaxations tend to make current density profiles broad as they limit the central value of $|\vec{J}|$.

Sawtooth relaxations may even be useful in controlling reactor plasmas to prevent buildup of helium ash in the core.

An insightful qualitative description of the sawtooth relaxation using the resistive MHD model was proposed by Kadomtsev [43] and is described here. The Kadomtsev model is a classic example of magnetic reconnection. When the current density increases to the point where q_0 drops below unity in the plasma core, the linear mode that drives the sawtooth becomes unstable and grows exponentially with growth rate γ. After the mode grows to a large size and distorts the equilibrium fields enough to influence further evolution, the mode is said to be in its non-linear phase of evolution. The non-linear evolution of the sawtooth mode is to drive spontaneous reconnection. The plasma core inside the $q = 1$ surface is driven into a Sweet-Parker like resistive reconnection layer and an $m/n = 1/1$ island grows rapidly on the side of the core opposite the reconnection layer. The island continues to grow rapidly even after it becomes large in contrast to the evolution of, for example, the islands that form due to an unstable $m/n = 2/1$ tearing mode. The process ends in a state with closed nested flux surfaces and $q \geq 1$. All of the flux in the core is completely reconnected and the center of the island becomes the new magnetic axis. Kadomtsev's qualitative description of sawtooth relaxations explains the observed drops in temperature and density in the plasma core. The relaxation ejects thermal energy and mass density from the core by advection and rapid parallel heat conduction.

After a relaxation, the flattened profile becomes peaked again as the core reheats on the energy confinement time scale τ_E, and q_0 drops below unity again as the current density resistively diffuses back into the core on the resistive diffusion time scale τ_r. In this way, the sawtooth relaxation occurs repeatedly with average period τ_{saw}.

The $m = 1$ resistive kink mode is often implicated in sawtoothing. As mentioned earlier, the eigenfunction of this mode represents a nearly incompressible rigid displacement of the plasma column inside $q = 1$ with an $n = 1$ toroidal variation in the direction of displacement. Despite being commonly referred to as a $m = 1$ mode, this mode is not characterized by a

particular value of m when the equilibrium cross section is non-circular or the geometry is toroidal. The eigenfunction is $m = n = 1$ only for a plasma with a circular cross section in a periodic cylinder geometry.

The Kadomtsev picture of sawtoothing in a resistive MHD model was very successful at describing many properties of the sawtooth in early tokamak experiments. However as measurements became more accurate and tokamak plasmas got hotter, discrepancies between the model and experimental observations appeared. First, relaxations cause a much more rapid drop in the central plasma temperature of hot tokamaks than predicted. Wesson offered an explanation for these fast sawtooth crashes using a resistive MHD model [44]. Wesson's model describes a sawtooth relaxation based on the non-linear evolution of the quasi-interchange (QI) mode. The QI mode eigenfunction is not a rigid displacement of the core, and is sometimes described as a convection cell. The nonlinear evolution of the QI does not involve much reconnection, so it does not have Sweet-Parker scaling and the crash can proceed much faster in high temperature, low resistivity plasmas given a resistive MHD model. However, more accurate experimental methods for measuring q profiles in tokamaks were developed later. It was found that the profiles during sawtoothing discharges are not necessarily flat with $q \approx 1$ as needed by Wesson's description of the sawtooth. Nevertheless, Wesson-like relaxations have been observed experimentally on occasion [45]. Eventually it was found that two-fluid model equations or non-ideal terms in Ohm's law (Eq. 1.17) besides the resistive term ηJ, such as the Hall and electron inertia terms, can account for the fast crashes [46, 47]. These terms in Ohm's law can allow much faster reconnection at low resistivity.

Another discrepancy is that the central safety factor was found to be well below unity $q_0 < 1$ after a relaxation. At this time, the most accepted explanation is that there is only partial reconnection of the core. The process of reconnection is halted sometime during the relaxation. Large, hot tokamaks with significant populations of fast particles sometimes see so called "giant sawteeth" [48]. Giant sawteeth are much larger relaxations and may cause

disruptions. They are a concern for ITER. In hot tokamaks, under some circumstances, minority hot particle species can stabilize the sawtooth instability. The central safety factor q_0 drops well below unity during the long period of stabilization, until instability is triggered, and the resulting crash is very large.

There have been many previous numerical studies of sawtooth oscillations in tokamaks. In the mid 70s, there was success in validating Kadomtsev's model by the simulation of a single sawtooth relaxation with a reduced MHD model in a periodic cylinder geometry [49]. Later, simulations using strongly anisotropic temperature diffusion were successful in demonstrating periodic sawtooth relaxations [50]. Strong heat conduction parallel to the magnetic field was found to suppress a convection cell that forms after relaxations and causes the solution to reach a helical steady state that does not oscillate. MHD simulations have been shown to give realistic crash times and sawtooth period times for small Ohmically heated tokamaks with Lundquist numbers $S < 10^7$ [51].

Many recent works focus on sawtooth relaxations in large, hot tokamaks with $S > 10^7$. In these cases more sophisticated model equations such as two-fluid MHD are needed. Simulations of periodic MHD sawtoothing have been useful as a benchmark problem recently in [52]. In [53], MHD problems formulated to reach a non-oscillating helical steady-state, that maintain $q_0 \approx 1$ without relaxing, were used to explain certain experimentally observed sawtooth-free discharges in tokamaks.

There have also been some numerical studies of sawteeth in current carrying stellarators. The first non-linear numerical studies of sawteeth in current carrying stellarators are due to Wakatani. These simulations used a model based on a low-β, large aspect ratio expansion [54], where β is the ratio of thermodynamic pressure to magnetic pressure. The effect of the helical stellarator field was accounted for by representing the flux function $\psi = \psi_{vac} + \psi_\sigma$, where ψ_{vac} is due to the stellarator field and ψ_σ is due to the plasma current. Relaxations conforming to Kadomtsev's description of the sawtooth relaxation were recovered in [55].

1.6.1 Effect of Shaping on Sawteeth

It has long been known that two-dimensional shaping of tokamak profiles can affect the properties of sawteeth including τ_{saw}. Early observations noted the effect of triangularity the on sawtooth period [56]. Studies of sawtoothing in TCV attribute a β trigger for ideal MHD instability as the reason for correlation between τ_{saw} and profile shaping [10, 57]. Variation of τ_{saw} in DIII-D with shaping was attributed to a transition from a resistive internal kink like mode to a quasi-interchange like mode [11].

This chapter briefly introduced many basic tokamak and stellarator concepts which the reader will need to be aware of in subsequent discussions. Much of this introduction focused on simple ideal or resistive MHD model equations. In the next section introduces NIMROD the numerical methods used by NIMROD, which will also be needed in subsequent discussions. The model equations used for the numerical study will also be introduced. Although these model equations use a more sophisticated closure than resistive MHD, the considerations presented in the present chapter are still relevant.

Chapter 2

NIMROD Numerical Methods and Model Equations

Analytic methods are often preferred for studying problems in linear ideal MHD, especially when there are singularities in the solution. However, when seeking solutions for nonlinear problems or problems with extended MHD model equations or realistic geometry numerical calculations on a computer are usually required.

In this section the model equations used to study CTH sawteeth are introduced. For many MHD problems in magnetic fusion, especially axisymmetric tokamak problems, the numerical methods of NIMROD allow efficient computation of an approximate solution. However, it was found in the course of this work that some of the numerical convergence properties are different for MHD problems having fields that are not nearly axisymmetric. Some improvements, which are described later, were made so that non-axisymmetric MHD problems may be solved with more ease and efficiency. To facilitate these discussions, several aspects of the numerical method are summarized in this section. Note that while NIMROD is generally applied to problems in magnetic fusion, it has the flexibility to be applied to other problems in MHD. In appendix C NIMROD is successfully used to compute solutions to fluid shocktube problems.

2.1 Model Equations

In this work a set of extended resistive MHD equations are evolved with NIMROD, which has been applied to study CTH previously [58, 59]. Because CTH is a small, relatively low temperature experiment, historical precedent suggests that an extended resistive MHD model with anisotropic temperature diffusion and sources is appropriate for this study. The equations, which will be solved in a toroidal geometry, are formulated in terms of the

magnetic field $\vec{B}$, temperature T, number density n and flow velocity $\vec{V}$:

$$\begin{aligned}
\rho\Big(\frac{\partial \vec{V}}{\partial t} + (\vec{V}\cdot\nabla)\vec{V}\Big) &= \vec{J}\times\vec{B} - \nabla p - \nabla\cdot\overleftrightarrow{\Pi} \\
\frac{3n}{2}\Big(\frac{\partial T}{\partial t} + \vec{V}\cdot\nabla T\Big) &= -\frac{p}{4}\nabla\cdot\vec{V} - \nabla\cdot\vec{q} + Q \\
\frac{\partial n}{\partial t} + \nabla\cdot(n\vec{V}) &= -\nabla\cdot(D\nabla\nabla^2 n) \\
\frac{\partial \vec{B}}{\partial t} &= \nabla\times(\vec{V}\times\vec{B} - \eta\vec{J}) + \kappa_{divb}\nabla\nabla\cdot\vec{B} \\
p &= nk_B(T + T_e) \\
\vec{J} &= \frac{\nabla\times\vec{B}}{\mu_0} \\
\vec{E} &= -\vec{V}\times\vec{B} + \eta\vec{J}.
\end{aligned} \tag{2.1}$$

Although this is a single fluid model, the temperature T is actually considered to be an ion temperature. The electron temperature, used in the calculations for pressure p and resistivity η, is given by $T_e = 3T$. This definition is motivated by the fact that the electron temperature is higher than the ion temperature in CTH plasmas. The Boltzmann constant is $k_B = 1.6\times10^{-19}\ J/eV$. Several non-ideal dissipation, diffusion and source terms are included in these model equations. A hyperdiffusivity controlled with the parameter D is used to keep spurious oscillations from forming in the density. An error diffusion term proportional to κ_{divb} is used to maintain nearly zero magnetic divergence in the solution fields. The heat flux, viscous stress tensor, resistivity and heat source are given by

$$\begin{aligned}
\vec{q} &= -n\Big(\chi_{\parallel}\hat{b}\hat{b} + \chi_{\perp}\Big(\overleftrightarrow{I} - \hat{b}\hat{b}\Big)\Big)\cdot\nabla T \\
\chi_{\perp} &= \frac{\chi_{\perp,0}}{B^2}\sqrt{\frac{T_{ref}}{T}} \\
Q &= \eta J^2 \\
\overleftrightarrow{\Pi} &= -\nu\rho\Big(2\nabla\vec{V} + (\nabla\vec{V})^T - \frac{2}{3}\nabla\cdot\vec{V}\Big) \\
\eta &= \eta_0\Big(\frac{T_{ref}}{T_e}\Big)^{3/2}.
\end{aligned} \tag{2.2}$$

The heat flux $\vec{q}$ is highly anisotropic. Heat conduction parallel to the magnetic field is several orders of magnitude larger than in the perpendicular direction. While the parallel heat conduction coefficient $\chi_{\parallel}$ has a constant value, the perpendicular heat conduction coefficient $\chi_{\perp}$ is coupled to the temperature and magnetic field. The heat source Q is Ohmic. The viscous stress tensor $\overleftrightarrow{\Pi}$ is proportional to the coefficient of viscosity ν and the mass density $\rho = m_i n$, where m_i is the ion mass. η has a Spitzer temperature dependence $\eta \propto T_e^{-3/2}$.

2.2 Time Discretizations

Understanding the temporal convergence properties of non-axisymmetric NIMROD simulations was perhaps the most critical obstacle to getting correct results. Therefore, temporal discretization and time stepping methods will be described in some detail. Consider the equations solved by NIMROD written in the following form,

$$\frac{\partial \vec{u}}{\partial t} = \vec{L}(\vec{u}) \tag{2.3}$$

where $\vec{L}$ is a differential operator and $\vec{u}$ is the solution vector. Given the boundary conditions and initial conditions $\vec{u}^n$ at time t^n, we would like to know the solution $\vec{u}^{n+1}$ at time t^{n+1}. Given that $\Delta t \equiv t^{n+1} - t^n$ is small, a naive and straightforward approach to obtain an approximate solution would be to use the following truncated expansion to obtain an approximate expression for the time derivative,

$$\begin{aligned} \vec{u}^{n+1} &\approx \vec{u}^n + \Delta t \left(\frac{\partial \vec{u}}{\partial t}\right)^n \\ \vec{u}^{n+1} &= \vec{u}^n + \vec{L}(\vec{u}^n)\Delta t. \end{aligned} \tag{2.4}$$

If Δt is very large, it does not make sense to use a series expansion for the approximation. In this case the time interval may be broken up into many small time steps and the above process can be followed repeatedly to obtain an approximate solution at the desired time. Retaining more terms in the series expansion would allow larger step sizes, so that fewer

steps must be taken. However, accuracy of the truncated series approximation is not the only consideration in determining the largest possible time step Δt. The above procedure is an example of an explicit method sometimes called the forward Euler method. When using an explicit method, the size of the time step Δt is limited by the Courant-Friedrichs-Lewy (CFL) condition for numerical stability,

$$C = \frac{v\Delta t}{\Delta x} \leq C_{max}, \tag{2.5}$$

where v is the speed of the fastest wave or flow in the system and Δx is the spacing of the spatial computational grid. If the CFL condition is violated, one will arrive at a spurious numerical solution that does not approximate the real solution.

When $C_{max} = 1$, the CFL condition can be interpreted as a statement that waves or flows may not travel a distance longer than the spacing of the computational grid Δx in one time step Δt. This is extremely restrictive when finding numerical MHD solutions for tokamak or stellarator problems because they are very stiff. In stiff problems the phenomena of interest occur much more slowly than the fastest normal modes in the system. The propagation of fast waves and Alfvén waves is many orders of magnitude faster than the evolution of resistive tearing modes or the global resistive diffusion of the magnetic field. A very large number of time steps would need to be taken to study such problems with an explicit numerical method. The Lundquist number S, defined as the ratio of the characteristic times of Alfvén wave propagation and resistive diffusion, is a measure of how separated these time scales are. In this work we consider problems having Lundquist numbers $S \approx 10^5$. The definition for Alfvén transit time used in this work is $\tau_A = R/v_{A,\|}$. Resistive diffusion of the magnetic fields is an essential part of the expected solution.

NIMROD uses an implicit method for the advection and diffusion terms that appear in the equations. When an implicit method is used, time step size Δt is not limited by the CFL condition and the solution may be computed with fewer time steps. For very stiff

problems, implicit methods may offer a way to obtain a numerical solution that is more computationally efficient than an explicit method. The backwards Euler method is a simple example of an implicit method. The time derivative is approximated using a backwards Taylor series expansion,

$$\begin{aligned} \vec{u}^n &\approx \vec{u}^{n+1} - \Delta t \left(\frac{\partial \vec{u}}{\partial t} \right)^{n+1} \\ \vec{u}^{n+1} &= \vec{u}^n + \vec{L}(\vec{u}^{n+1}) \Delta t. \end{aligned} \tag{2.6}$$

The drawback of the implicit method is that computing $\vec{u}^{n+1}$ at each time step is more difficult. In the above example, the differential operator must be evaluated at the advanced time t^{n+1}. This can be formulated as a large matrix inversion problem. The size and form of the matrix to be inverted depend on the spatial discretization. For example, suppose high order finite differences are used, where many terms are kept in the truncated Taylor series, for the spatial derivatives. Computing the spatial derivative at a particular point will involve the values of the solution field at many grid points along the direction of differentiation. The resulting matrix is less diagonally dominant and more poorly conditioned than if only the first order term was kept for the spatial finite differences. In general, higher order spatial discretizations lead to more poorly conditioned implicit time advance matrices.

Note that while the implicit method is numerically stable with large Δt, accuracy may be bad with large Δt. Step size should be not be too large with respect to the timescale relevant to the physical phenomena of interest. Additionally, using second order or higher finite differences in the time discretization may be necessary for accuracy with large Δt [60]. Explicit methods are often limited to a very small time step so that a finite difference that is only first order accurate in Δt may be used effectively.

2.2.1 Semi-Implicit Methods

NIMROD uses a semi-implicit method that removes the CFL condition on time step size for MHD waves. Semi-implicit methods are intended to have the strengths of both explicit and implicit methods. A large Δt is possible while retaining numerical stability, but

the matrix inversion problem of finding $\vec{u}^{n+1}$ should be easier than a fully implicit method. Additionally, semi-implicit methods are sometimes easier to implement than a fully implicit method. The idea is to effectively modify the temporal truncation error with an implicit term that introduces a phase error. The phase error slows down the fastest normal modes of the system at large Δt so that the CFL condition is not violated [61]. For accuracy at large Δt, semi-implicit operators should have eigenmodes similar to fast normal modes in the physical system.

One of the first applications of the semi-implicit method to MHD was by Harned and Kerner [62]. Subsequent improvements to this method lead to the semi-implicit method used in NIMROD. The Harned and Kerner method will be introduced and the historical progression to the semi-implicit operator used by NIMROD followed. First, consider the MHD momentum equation written in the following form, where $\vec{F}$ is the MHD force operator,

$$\rho \frac{\partial \vec{V}}{\partial t} = \vec{F}(\vec{B}, \vec{V}, p, \rho). \tag{2.7}$$

Now consider an explicit method to solve this equation,

$$\vec{V}^{n+1} = \vec{V}^{n} + \frac{\Delta t}{\rho^n} \vec{F}(\vec{B}^n, \vec{V}^n, p^n, \rho^n). \tag{2.8}$$

The following truncated Taylor series expansion was used to approximate the time derivative,

$$\left(\frac{\partial \vec{V}}{\partial t}\right)^n = \frac{\vec{V}^{n+1} - \vec{V}^n}{\Delta t} \underbrace{-\Delta t \left(\frac{\partial^2 \vec{V}}{\partial t^2}\right)^n + \ldots}_{\text{Truncation Error}}. \tag{2.9}$$

The truncated terms are said to be part of the truncation error.

For tokamak problems, the size of the time step Δt is severely limited by fast waves traveling in the radial direction. The method developed by Harned and Kerner effectively modifies the truncation error to treat fast wave behavior implicitly. Time steps are then no longer subject to the fast wave CFL restriction. Consider the uncoupled linearized MHD

velocity equation Eq. 1.10, restated here for convenience,

$$\frac{\partial^2\vec{V}_1}{\partial t^2} = \frac{1}{\mu_0\rho_0}\Big[\vec{B}_0\times\nabla\times\nabla\times(\vec{B}_0\times\vec{V}_1)-(\nabla\times\vec{B}_0)\times\nabla\times(\vec{B}_0\times\vec{V}_1)+\mu_0\nabla(\vec{V}_1\cdot\nabla p_0)+\mu_0\nabla(\frac{5p_0}{3}\nabla\cdot\vec{V}_1)\Big].$$

Now rewrite this equation for the case where the equilibrium fields are uniform, so that terms having gradients of equilibrium fields vanish.

$$\frac{\partial^2\vec{V}_1}{\partial t^2} = \frac{1}{\mu_0\rho_0}\Big[\vec{B}_0\times\nabla\times\nabla\times(\vec{B}_0\times\vec{V}_1)+\mu_0\frac{5p_0}{3}\nabla\nabla\cdot\vec{V}_1\Big]. \tag{2.10}$$

We would like to keep only terms involved in representing fast waves traveling perpendicular to the magnetic field. These waves satisfy $\vec{k}\cdot\vec{B}_0 = 0$. First consider the following expression

$$\nabla\times(\vec{B}_0\times\vec{V}_1) = \vec{B}_0\nabla\cdot\vec{V}_1 - (\vec{B}_0\cdot\nabla)\vec{V}_1. \tag{2.11}$$

Given that normal modes in a homogeneous equilibrium have a spatial dependence $\vec{V}_1 \propto e^{i\vec{k}\cdot\vec{x}}$, we can invoke $\nabla\to i\vec{k}$. Terms having a factor of $\vec{k}\cdot\vec{B}_0$ are eliminated

$$\nabla\times(\vec{B}_0\times\vec{V}_1) \to i\vec{B}_0\vec{k}\cdot\vec{V}_1 - \cancelto{0}{i(\vec{B}_0\cdot\vec{k})\vec{V}_1}. \tag{2.12}$$

Now rewrite the first term in 2.10 using 2.12 and $\vec{k}\cdot\vec{B}_0 = 0$

$$\vec{B}_0\times\nabla\times\nabla\times(\vec{B}_0\times\vec{V}_1) = \vec{B}_0\times\nabla\times(\vec{B}_0\nabla\cdot\vec{V}_1),$$

$$= \vec{B}_0\times(\nabla\nabla\cdot\vec{V}_1\times\vec{B}_0),$$

$$= \nabla\nabla\cdot\vec{V}_1(\vec{B}_0\cdot\vec{B}_0) - \vec{B}_0(\vec{B}_0\cdot\nabla\nabla\cdot\vec{V}_1),$$

$$\to -\vec{k}\vec{k}\cdot\vec{V}_1(\vec{B}_0\cdot\vec{B}_0) + \vec{B}_0(\cancelto{0}{\vec{B}_0\cdot\vec{k}}\vec{k}\cdot\vec{V}_1).$$

Therefore, after invoking assumptions that the equilibrium fields are uniform and only modes with $\vec{k} \cdot \vec{B}_0 = 0$ are excited, Eq. 1.10 can be written

$$\frac{\partial^2 \vec{V}_1}{\partial t^2} = \Big[\frac{B_0^2}{\mu_0 \rho_0} + \frac{\frac{5p_0}{3}}{\rho_0}\Big]\nabla\nabla \cdot \vec{V}_1. \tag{2.13}$$

We arrive at the semi-implicit method by modifying the explicit scheme of Eq. 2.8. Terms having the same form as Eq. 2.13 are added to the perpendicular part of Eq. 2.8

$$\vec{V}_\perp^{n+1} - (\Delta t)^2 A_0 \nabla(\nabla \cdot \vec{V}_\perp^{n+1}) = \vec{V}_\perp^n + \frac{\Delta t}{\rho^n}\vec{F}_\perp(\vec{B}^n, \vec{V}^n, p^n, \rho^n) - (\Delta t)^2 A_0 \nabla(\nabla \cdot \vec{V}_\perp^n), \tag{2.14}$$

while the parallel part of Eq. 2.8 is left unchanged

$$\vec{V}_\parallel^{n+1} = \vec{V}_\parallel^n + \frac{\Delta t}{\rho^n}\vec{F}_\parallel(\vec{B}^n, \vec{V}^n, p^n, \rho^n). \tag{2.15}$$

Eq. 2.14 can be written using a more compact notation

$$\vec{V}_\perp^{n+1} - (\Delta t)^2 A_0 \nabla(\nabla \cdot \Delta\vec{V}_\perp) = \vec{V}_\perp^n + \frac{\Delta t}{\rho^n}\vec{F}_\perp(\vec{B}^n, \vec{V}^n, p^n, \rho^n), \tag{2.16}$$

where $\Delta\vec{V}_\perp \equiv \vec{V}_\perp^{n+1} - \vec{V}_\perp^n$.

Equations Eq. 2.16 and 2.15 constitute a semi-implicit method. They are consistent in the sense that the original PDE, Eq. 2.7, is recovered in the limit $\Delta t \to 0$ and it can be shown that it is numerically stable with time steps Δt larger than the fast wave CFL limit given a sufficiently large semi-implicit factor A_0. $\vec{L} \equiv A_0 \nabla\nabla \cdot \Delta\vec{V}_\perp$ is said to be the "semi-implicit operator".

The subsequent improvement to the above semi-implicit method allowed time steps Δt larger than the Alfvén CFL limit to be taken. This semi-implicit operator is based on

Eq. 2.10, but without using $\vec{k} \cdot \vec{B}_0 = 0$

$$\begin{aligned} \vec{L} = \vec{C}_0 \times \nabla \times \nabla \times (\vec{C}_0 \times \Delta\vec{V}) + C_{iso}\nabla^2(\Delta v), \\ \textit{terms with } C_i C_j,\ i \neq j \textit{ are set to zero.} \end{aligned} \tag{2.17}$$

Because $\vec{C}_0$ is a uniform vector field it cannot be aligned with the magnetic field in most problems of interest. It can be shown that when $\vec{C}_0$ is not parallel to $\vec{B}$, the terms $C_i C_j$ with $i \neq j$ are destabilizing [60]. These terms $i \neq j$ are therefore set to zero in the operator.

Reference [63] introduced a semi-implicit operator having a form that is not motivated by Eq. 1.10,

$$\vec{L} = C_0 \nabla^2(\Delta v). \tag{2.18}$$

This semi-implicit operator is commonly called the isotropic operator. While the isotropic operator provides numerical stability, it was found that accuracy is bad for tearing mode problems if a large Δt is used. The growth rates of the tearing modes were artificially lowered.

The next improvement to the semi-implicit operator Eq. 2.17 was introduced by Lerbinger and Luciani [64],

$$\begin{aligned} \vec{L} = \frac{C_{lin}}{\mu_0 \rho_{eq}} \Big[\vec{B}_{eq} \times \nabla \times \nabla \times (\vec{B}_{eq} \times \Delta\vec{V}) - (\nabla \times \vec{B}_{eq}) \times \nabla \times (\vec{B}_{eq} \times \Delta\vec{V}) \\ + \mu_0 \nabla(\Delta\vec{V} \cdot \nabla p_{eq}) + \mu_0 \nabla(\frac{5 p_{eq}}{3} \nabla \cdot \Delta\vec{V}) \Big] + C_{nl}\nabla^2(\Delta v). \end{aligned} \tag{2.19}$$

Lerbinger's operator is based on Eq. 1.10 with the actual equilibrium fields of the problem under consideration, instead of assuming uniform equilibrium fields. A Laplacian term is also added, however the coefficient of the Laplacian operator C_{nl} is very small. The isotropic operator prevents numerical instability during highly nonlinear periods of evolution when deviation from the equilibrium fields is significant. Because only a small amount of isotropic operator is used, accuracy is not degraded.

NIMROD uses a semi-implicit method that is very similar to Lerbinger's method,

$$\vec{L} = \frac{1}{\mu_0 \rho_{si}} \Big[C_{mhd} \vec{B}_{si} \times \nabla \times \nabla \times (\vec{B}_{si} \times \Delta \vec{V}) - C_{j0} (\nabla \times \vec{B}_{si}) \times \nabla \times (\vec{B}_{si} \times \Delta \vec{V}) + C_{pres} \mu_0 \nabla (\Delta \vec{V} \cdot \nabla p_{si}) + C_{pres} \mu_0 \nabla (\frac{5 p_{si}}{3} \nabla \cdot \Delta \vec{V}) \Big] + C_{nl} p_{nl} \nabla^2 (\Delta \vec{V}). \quad (2.20)$$

However, instead of using equilibrium fields in Eq. 1.10, the entire $n = 0$ part of the solution fields is used. This makes for better applicability to simulations occurring over long time intervals in which the equilibrium fields can change significantly. The coefficients C_{mhd}, C_{pres}, C_{j0} and C_{nl} are specified by the user and generally at least one of these coefficients must be greater than or equal to unity for numerical stability at large Δt.

When the fields used in the NIMROD semi-implicit operator, denoted with the subscript si, deviate from the solution fields the isotropic term is necessary for numerical stability at large Δt. Typically the semi-implicit operator fields are taken to be the $n = 0$ component of the solution fields. When considering an axisymmetric device such as a tokamak, a small isotropic coefficient $C_{nl} p_{nl}$ provides stability during deep nonlinear phases of the evolution. NIMROD dynamically adjusts the size of the isotropic term using the non-axisymmetric pressure $p_{nl}(R, Z) = \max_{\phi} \left| (B^2 - B_0^2)/\mu_0 + 5(p - p_0)/3 \right|$. The non-axisymmetric equilibrium fields considered in this work lead to a large value for p_{nl} and a large isotropic coefficient is known to affect temporal convergence properties. The capability to use the full 3D solution fields in the semi-implicit operator was added in this work. With the full solution fields in the semi-implicit operator, a large isotropic term is not needed for numerical stability for problems with non-axisymmetric equilibria. Convergence properties and implementation details of the 3D semi-implicit operator are discussed in sections 6.3.2 and 6.3.2, and the source code is given in appendix B.

2.3 Spatial Discretization

NIMROD represents the solution fields in a basis function expansion, $f = \sum_{i,n} C_{i,n} f_{i,n}$, where $C_{i,n}$ are the expansion coefficients and $f_{i,n}$ are the basis functions. The basis functions are 2D Lagrange C^0 finite elements [65] of degree p in the poloidal plane with harmonic dependence in the toroidal direction, so they may be written $f_{i,n} = \hat{f}_i^p(x_1, x_2)e^{in\phi}$. This discretization often enables high accuracy and good computational efficiency for magnetic fusion problems.

A 2D Lagrange C^0 finite element of degree p is a two-dimensional piecewise polynomial of degree p. The values of the polynomial coefficients are constrained so that the function they represent in a basis function expansion has C^0 continuity over the poloidal plane. Note that poloidal basis functions $\hat{f}_i^p(x_1, x_2)$ are complex valued, with separate Lagrange finite elements for the real and imaginary parts. Coordinates x_1, x_2 are logical coordinates, and elements with different i subscripts have different mappings from R, Z to x_1, x_2 allowing for arbitrary geometric shapes of the poloidal cross-section of the domain.

When solution fields are smooth, p-type numerical refinement, accomplished by increasing the finite element order p and max Fourier number n, results in exponential convergence. It can be shown for a simple elliptic problem (that doesn't not involve time derivatives), the norm of the error is $|\epsilon| \propto h^p$, where h is the spacing between finite elements and p is the degree of the elements [66]. The exponential convergence from p-type refinement is crucial for efficiently solving the extremely anisotropic thermal diffusion that is essential for simulations in magnetic confinement fusion [67]. H-type refinement, while less efficient than p-type refinement for smooth solutions, is needed to handle solutions with near discontinuities such as those found in the fields when resolving an unstable tearing mode. H-type refinement in NIMROD can be accomplished by increasing the number of finite elements in the poloidal plane or packing them near discontinuities. Reference [66] provides a detailed explanation of finite elements and hp convergence.

Fourier spectral methods can be very powerful, because it is sometimes the case that only a few harmonics are needed to represent the solution. However, it should be noted that Fourier spectral discretizations lead to dense and poorly conditioned matrix inversion problems when advancing the solution fields with an implicit method [68]. Finite difference, finite volume or finite element discretizations typically lead to sparse matrices with better conditioning (losing sparseness as the order of the method is increased).

2.4 Galerkin Method

The Galerkin method is used in evolving the the model equations. This involves taking inner products of the residual with a set of test functions, and choosing the solution which minimizes these quantities. This set of integrals is referred to as a weak form of the original PDEs. The test functions are the complex conjugates of the basis functions $f^*_{i,n}$. The solution fields are advanced by computing the coefficients $C_{i,n}$ so that each inner product has a value of zero. NIMROD solves this linear system with a GMRES [69] iterative solver. Two-dimensional solutions for each Fourier number n are computed and used for preconditioning. A sparse direct solver is effective in computing the 2D solutions since they constitute much smaller problems [70].

Because a Fourier representation is used, the solution fields at any point in the domain are represented with several overlapping basis functions. Computing the residual when advancing the solution fields requires the computation of Fourier convolutions. This is handled efficiently by approximating the Fourier series with a discrete Fourier transform. Solution fields are computed in configuration space at toroidally spaced collocation points. Multiplication and division of solution fields is performed in configuration space, and the result is transformed back to Fourier space with a fast Fourier transform (FFT). Three times the maximum Fourier number n is used in the FFT to reduce aliasing error in approximating the Fourier series. This is sometimes said to be a pseudo-spectral method. Note that some sources have a different definition for pseudo-spectral method, holding that a pseudo-spectral

method is a collocation method so that the test functions are not the basis functions as in the Galerkin method, but rather have Dirac delta functions to pick out the contribution of the residual at collocation points [66].

The integrand routines in NIMROD, which numerically compute the integrand for the inner product of the test functions with the residual, are broken into "right hand side" (RHS) and "dot" routines. The RHS routines compute the contributions to the inner product by the explicit terms which are evaluated using solution fields from the previous time step. The dot routines compute the contributions from terms requiring evaluation of the solution fields at the advanced time, such as time derivatives and implicit terms. Therefore when the GMRES solver is called to minimize the inner product, which gives the solution at the advanced time, the dot routines are called at every GMRES step. It is therefore crucial for performance that the dot routines have an efficient implementation.

Chapter 3

Sawtoothing in CTH

The CTH experiment is a hybrid between a stellarator and a tokamak. The vacuum vessel is a circular cross section torus having a major radius $R_0 = 0.75\ m$ and minor radius $a = 0.3\ m$. The typical toroidal field strength during a discharge is $B_\phi = 0.5\ T$ at the magnetic axis. It has a helical $L = 2$ stellarator magnet coil with five field periods ($N_{fp} = 5$). The CTH magnet coils are illustrated in Fig. 3.1. A detailed description of the device may be found in reference [71]. CTH plasmas have a low $\beta < 0.01$ and the plasmas are limited, not diverted. It can be operated as a pure stellarator with 20 eV ECRH plasmas, or a large plasma current can be driven inductively so that most of the rotational transform comes from the plasma current and the profiles are tokamak-like. Note that discharges in a pure tokamak configuration with a toroidal field of $B_\phi = 0.5\ T$ are not possible with CTH at the time of writing. One reason for this is that the toroidal field magnet coils are not rated for the current required for such a discharge. When a large plasma current is driven for tokamak-like operation, the plasma temperature is estimated to be around 150 eV and MHD activity characteristic of tokamaks such as disruptions may be observed. Perhaps the most reproducible plasma event observed in CTH are sawtooth relaxations.

Soft x-ray cameras enable observation of sawtoothing. On CTH there are three SXR cameras looking into the $\phi = 252°$ plane, each having 20 two-color detectors shown in figure 3.2 [72]. The camera is placed here because the flux surfaces are the least elongated at angles $\phi = 36°, 108°, 180°, 252°, 324°$. Sawtoothing can be seen clearly in the signals from the middle camera at $\theta = 0°$ shown in Fig. 3.3. Besides SXR cameras, CTH has a large number of sensors which measure the properties of the magnetic fields at the vacuum vessel. However, observing sawteeth by measuring magnetic fields outside of the plasma is typically

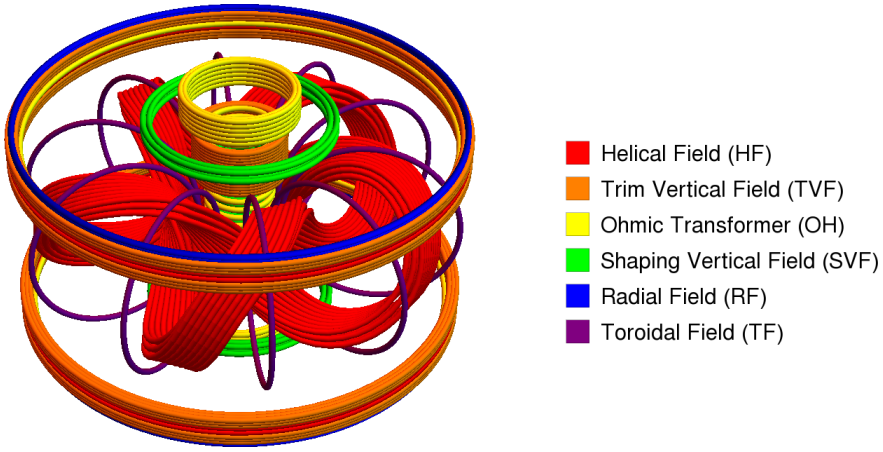

Figure 3.1: Three-dimensional rendering of a wire model for the CTH magnets. This wire model is used in computing the CTH magnetic field for the VMEC equilibrium code.

extremely difficult because the relaxation is localized inside the plasma core. The amount of information about the sawteeth that can be recovered from the magnetics is limited.

A clear correlation between the sawtooth repetition time τ_{saw} and the strength of the helical stellarator field is observed experimentally (Fig. 3.4). In the figure, it can be seen that τ_{saw} decreases as ι_{vac} increases. The quantity ι_{vac}, called the vacuum rotational transform, is used to describe the strength of the perturbing stellarator field. The vacuum transform is defined to be the rotational transform at the limiter when there is no plasma given the currents in the magnet coils, so ι_{vac} tends to increase in value as the current in the stellarator field magnet coil is increased. According to [54] the effect of the stellarator field in a low-β current carrying stellarator can be considered, to first order in a low β large aspect ratio expansion, by including the vacuum rotational transform profile. The ι profile of an $L = 2$ stellarator field is often taken to be constant, as in [73] which considered linear stability in current carrying stellarators.

Although the focus of this work is on numerical simulations, signals from the CTH soft x-ray cameras will be interpreted with tomography techniques in the following chapter. These are the first tomographic reconstructions of sawteeth in CTH. Additionally, a variation on the Fourier-Bessel method is presented that may be more suitable for studying highly shaped plasmas.

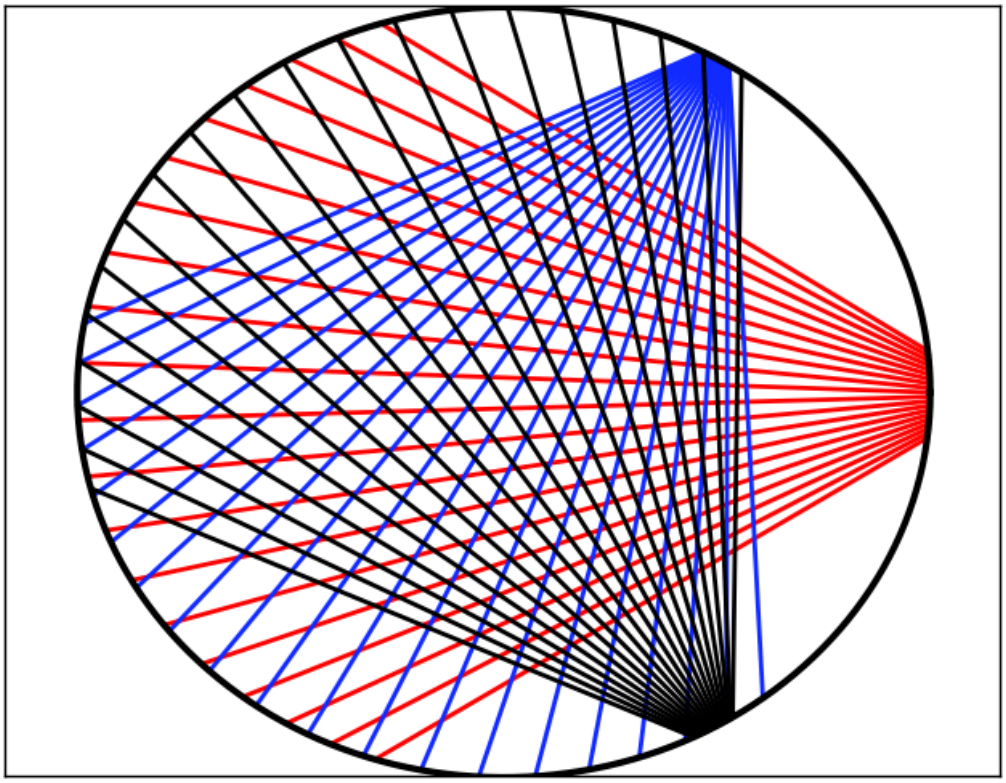

(a)

Figure 3.2: Three SXR cameras are positioned at poloidal angles $\theta = 0°$ (red), $60°$ (blue), $300°$ (black) and toroidal angle $\phi = 252°$. Each camera has 20 two-color detectors which are effectively pinhole cameras. The chords along which each pinhole camera is oriented are pictured.

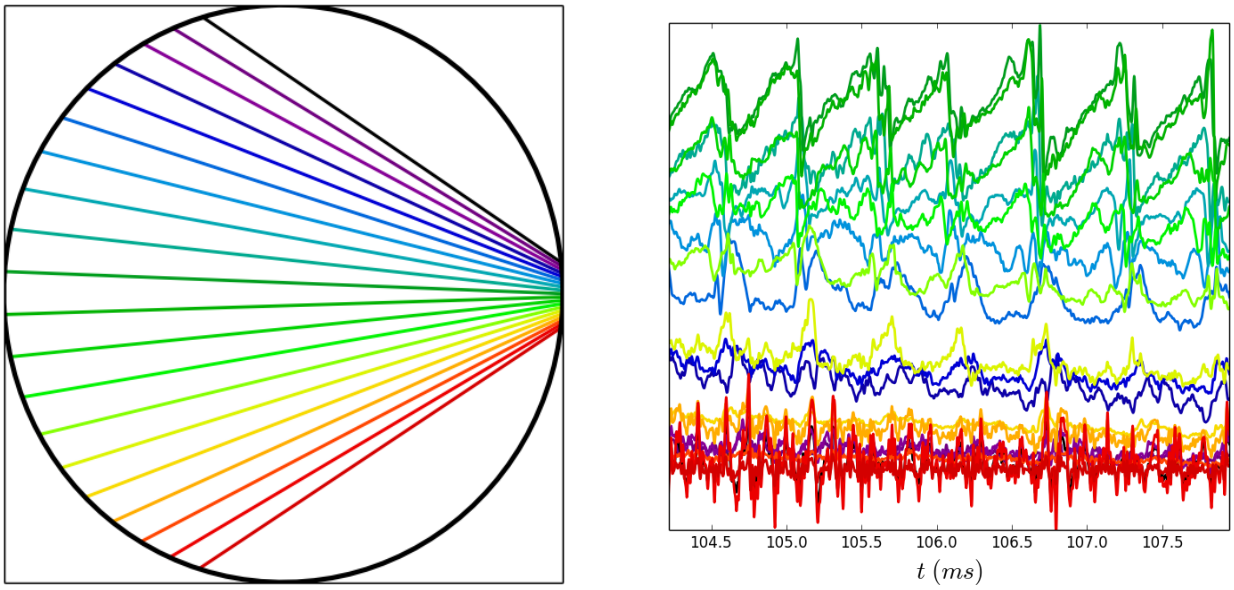

(a) (b)

Figure 3.3: Each pinhole camera chord from $\theta = 0°$ SXR camera is pictured in (a). In (b), the signals from the SXR camera at $\theta = 0°$ are shown during sawtooth activity. Each SXR signal corresponds to the pinhole camera having a chord of the same color. Note that signals with a larger average amplitude are from sensors pointing closer to the center of the plasma core where the temperature and density are higher. Seven relaxations can be seen, corresponding to the sudden drops of the signal from the central chords.

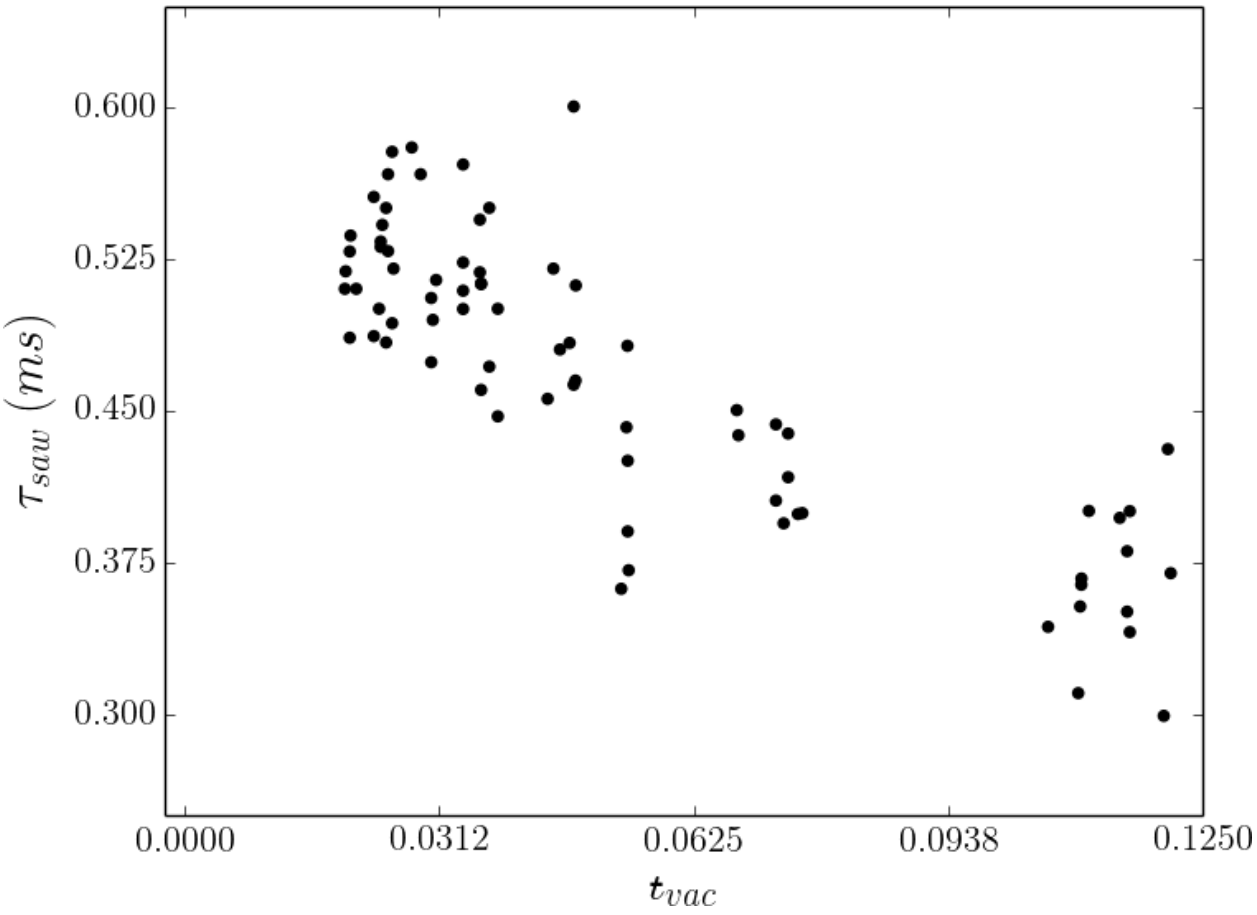

(a)

Figure 3.4: A correlation between τ_{saw} and t_{vac} is observed experimentally. Experimental data provided by Jeffery Herfindal.

Chapter 4

Soft x-ray Tomography of CTH Sawteeth

One method for efficiently interpreting data from SXR cameras is by tomographic reconstructions. Tomographic reconstructions use the signals from all cameras at a given time to reconstruct the two-dimensional emissivity profile $\epsilon(r,\theta)$ of the plasma at the toroidal cross-section where the cameras are located. An effective, simple and popular technique for SXR tomography in tokamaks is the Fourier-Bessel method [74]. This method represents the emissivity in a basis function expansion

$$\epsilon(r,\theta) = \sum_{m,l} \Big(a_{m,l} cos(m\theta) + b_{m,l} sin(m\theta) \Big) J_m(\lambda_m^{l+1} r). \tag{4.1}$$

The basis functions have harmonic dependence on the poloidal angle θ and the minor radius r dependence is given by Bessel functions.

The coefficients $a_{m,l}$, $b_{m,l}$ are chosen to make the signals computed from the emissivity profile $s_i^{(c)}$ agree with the measured SXR signals s_i in a least-squares sense. The model for the computed SXR signals is simply the emissivity integrated over the chord of the pinhole camera c_i,

$$s_i^{(c)} = \int_{c_i} \epsilon \; ds. \tag{4.2}$$

In most cases, the number of basis functions does not match the number of SXR signals so a singular value decomposition (SVD) is used for the least-square fit. In the least squares calculation, singular values less than the cutoff C_{cutoff} are not used. By specifying $C_{cutoff} > 0$, spurious features in the reconstructions can be removed. The choice of the number of basis functions used also has a significant effect on the reconstructions.

The implementation that has been developed in this work allows the user to select a shot from the database and a time interval over which reconstructions are to be computed. It is written in python and makes extensive use of the SciPy library [75]. Experimental SXR signals are automatically downloaded from the MDSplus [76] database used for CTH. Reconstructed emissivity profiles can be output as VTK files to facilitate efficient visualization and quantitative analysis.

4.1 Modified Fourier-Bessel Method using Equilibrium Flux

A problem with using the Fourier-Bessel method for stellarators is that the surfaces of constant toroidal flux are not necessarily nearly circular, but the radial coordinate of the basis functions has circular coordinate curves. Because the equilibrium does not conform to the basis functions in this sense, the quality of reconstructions can be affected. This has been previously addressed by using MHD equilibrium data in the tomography algorithm in order to incorporate information about the stellarator magnetic fields into the interpretation of the SXR signals [77].

Here, a novel variation on the Fourier-Bessel method is considered. The radial coordinate used is the normalized toroidal flux s from a VMEC equilibrium instead of the minor radius r. This shapes the basis functions to conform to the flux surfaces. Known information about the magnetic field is effectively incorporated into the reconstruction since the emissivity is approximately a function of the flux. In the next section, improvements to some aspects of tomography reconstructions are apparent when this modified Fourier-Bessel method is used. The flux surfaces of CTH are not too strongly shaped at $\phi = 252°$, but it is probable that the benefits of this method would be even more apparent given a more strongly shaped cross section.

4.2 Tomographic Reconstructions of Test Data

To demonstrate that the tomography implementation is correct, some test cases are considered. In the first test case, only the 20 chords from the SXR camera at $\theta = 0°$ are used. The SXR signals are assigned the values $sin(4\pi n/19)$ where n is the chord number with $n = 0$ being the top chord and $n = 19$ being the bottom chord. Reconstructed emissivities obtained using the standard Fourier-Bessel method with $C_{cutoff} = 0$ are shown in Fig. 4.1. As the number of basis functions used in the reconstructions is increased, the solution converges to "beams" of positive and negative emissivity along the chords. The beams of positive emissivity are aligned along the chords which have the highest signal values and the beams of negative emissivity lie along the chords with the lowest signal values. Since there are more basis functions than signals for the cases in Fig. 4.1, signals computed from the reconstructed emissivities match the input signals.

Next, test cases which are more representative of intended usage cases are considered. These test cases use data from the NIMROD simulations that are described in subsequent chapters. The i^{th} signal S_i is computed using

$$S_i = \int_{c_i} T_{nim}(s)\ ds, \tag{4.3}$$

where c_i is the i^{th} pinhole camera chord and s is the distance along the chord. A potential problem in tomography of NIMROD data is that the temperature of the numerical solution is not zero at the boundary, $T_e(a) \neq 0$. However, Fourier-Bessel method reconstructions are always zero at the boundary. Instead of attempting to reconstruct the numerical solution for the electron temperature T_e, a quantity T_{nim} defined as

$$T_{nim}(r,\theta) = \begin{cases} T_e(r,\theta) - T_{lcfs} & r \leq r_{lcfs}(\theta) \\ 0 & r > r_{lcfs}(\theta) \end{cases} \tag{4.4}$$

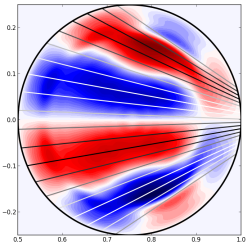

(a) m=5,l=15

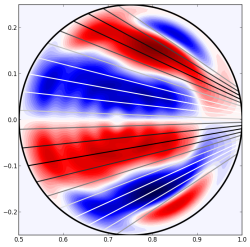

(b) m=10,l=5

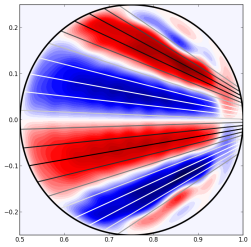

(c) m=10,l=10

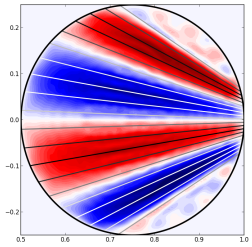

(d) m=20,l=20

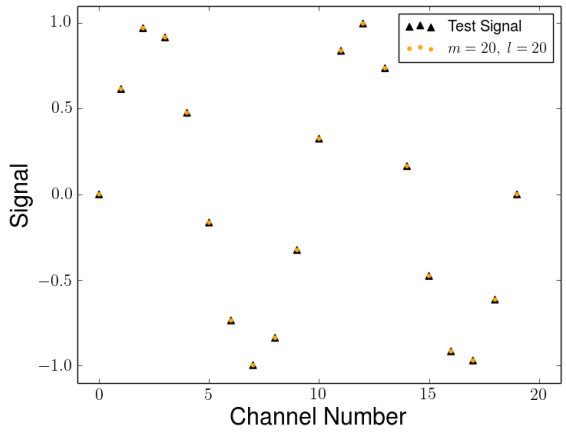

(e) Signals

Figure 4.1: Test cases for the Fourier-Bessel tomography implementation. Chords from the SXR camera at $\theta = 0°$ are assigned the values $sin(4\pi n/19)$ where n is the chord number. In (a) - (d), plots of the chords are overlaid on top of plots the reconstructed emissivities. The number of basis functions is scanned. The value of each chord's signal is indicated by the color of each plotted chord, with black corresponding to a value of 1 and white corresponding to a value of -1. As the number of basis functions is increased, the reconstructions converge to alternating "beams" of positive (red) and negative (blue) emissivity. In (e), the test signals are compared to signals computed from the reconstructed emissivity in (d).

is reconstructed. Because contours of T_e are nearly aligned with contours of magnetic flux, T_{nim} is nearly zero on the LCFS boundary and is nearly a smooth and continuous function over the domain.

The two test cases based on the NIMROD numerical solutions are to reconstruct the temperature profile at $\phi = 252°$ before a relaxation and "after" (when the relaxation is nearly finished). The cases will be called Before and After. Contour plots of T_{nim} for both cases are shown in Fig. 4.2. An SVD cutoff of 0.1 is used while the number of basis functions is scanned over three cases. In the standard Fourier-Bessel reconstructions, a minor radius of $a = 0.24$ is used while the modified reconstructions use a VMEC equilibrium having an LCFS that closely conforms to the LCFS of the NIMROD solution. Reconstructed temperature profiles for the Before and After cases, using both tomography methods, are shown in Fig. 4.3 and Fig. 4.4. An error E_{tom} for tomographic reconstructions is defined as a percent difference averaged over the area inside the NIMROD LCFS,

$$E_{tom} = \frac{\iint_{r<r_{lcfs}(\theta)} \sqrt{\left(\frac{2(T_{nim}(r,\theta) - T_{tom}(r,\theta))}{T_{nim}(r,\theta) + T_{tom}(r,\theta)}\right)^2} \, r \; dr d\theta}{\iint_{r<r_{lcfs}(\theta)} r \; dr d\theta}. \tag{4.5}$$

The error of each reconstruction is tabulated in Table 4.3.

The modified Fourier-Bessel method is significantly more accurate in an average error sense for both cases. However, the modified FB method solution for the Before case is not peaked enough in the center unless many basis functions are used, while the regular FB method solution is quite accurate in the center for the lowest resolution case. Preliminary testing has shown that using $\sqrt{s}$ instead of s as the radial coordinate for the modified method may eliminate the tendancy for reconstructions to be overly broadened in the center. Both methods, but especially the standard FB method, see the introduction of spurious features into the reconstructions as the number of basis functions is increased. It is therefore not immediately clear from these tests which method is better for studying sawtoothing, which is localized to the center of the plasma. When trying to develop an opinion of experimental

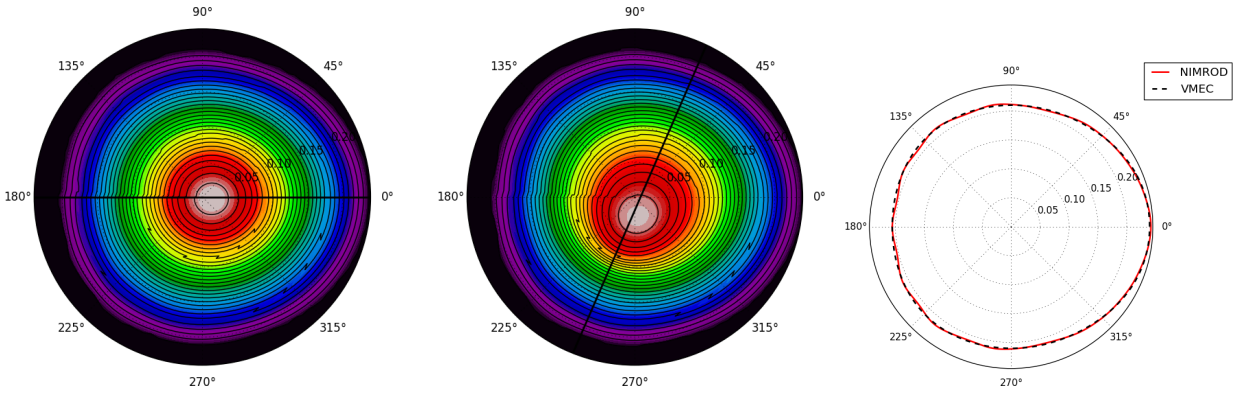

(a) Before (b) After (c) LCFS

Figure 4.2: T_{nim} for the Before and After cases are shown in (a) and (b) respectively. The black chord is a diagnostic chord along which quantities will be plotted for comparison. A comparison of the LCFS computed from the NIMROD solution and the VMEC LCFS is shown in (c).

phenomena with tomography, reconstructions using both methods and several values of m, l and C_{cutoff} should be considered and compared.

Table 4.1: Results for the Before test case, using both methods, are tabulated.

m, l	Fourier-Bessel	Modified FB
5, 12	0.137	0.0723
5, 15	0.138	0.0647
8, 15	0.183	0.113

Table 4.2: Results for the After test case, using both methods, are tabulated.

m, l	Fourier-Bessel	Modified FB
5, 12	0.137	0.0502
5, 15	0.137	0.0487
8, 15	0.160	0.0550

Table 4.3: Error E_{tom} of solutions to test cases Before and After. The modified Fourier-Bessel method solutions have a smaller error.

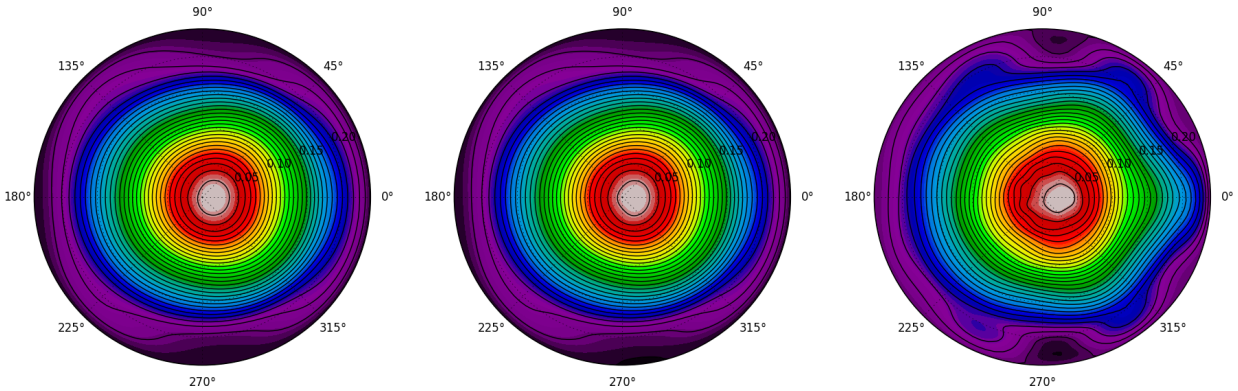

(a) Standard FB, $m = 5, l = 12$ (b) Standard FB, $m = 5, l = 15$ (c) Standard FB, $m = 8, l = 15$

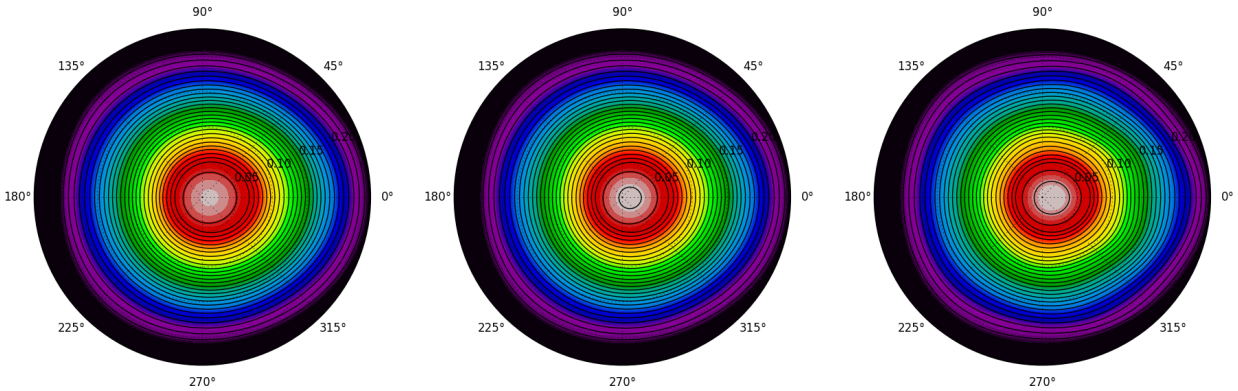

(d) Modified FB, $m = 5, l = 12$ (e) Modified FB, $m = 5, l = 15$ (f) Modified FB, $m = 8, l = 15$

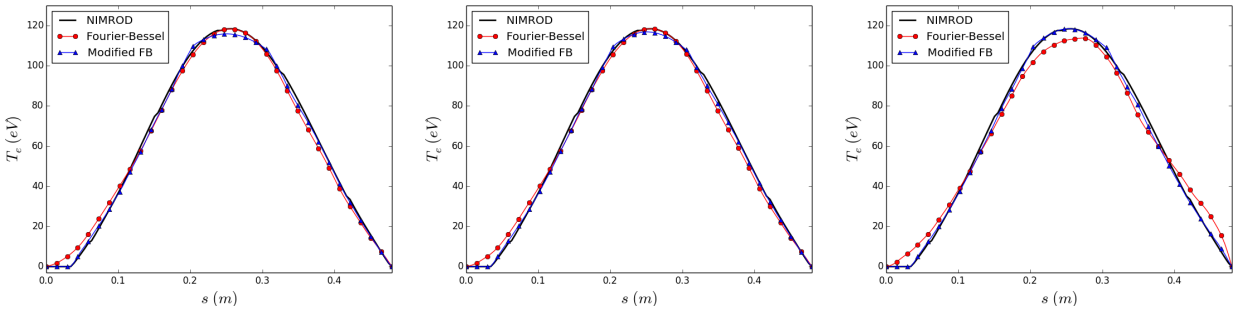

(g) Diagnostic Chord, $m = 5, l = 12$ (h) Diagnostic Chord, $m = 5, l = 15$ (i) Diagnostic Chord, $m = 8, l = 15$

Figure 4.3: Tomographic reconstruction results for the Before test case. The top row contains contour plots of reconstructions using the standard Fourier-Bessel method for three cases having different numbers of basis functions. The middle row contains contour plots using the modified Fourier-Bessel. The last row contains plots of the reconstructed T_e for both methods versus the test data along the diagnostic chord for each case.

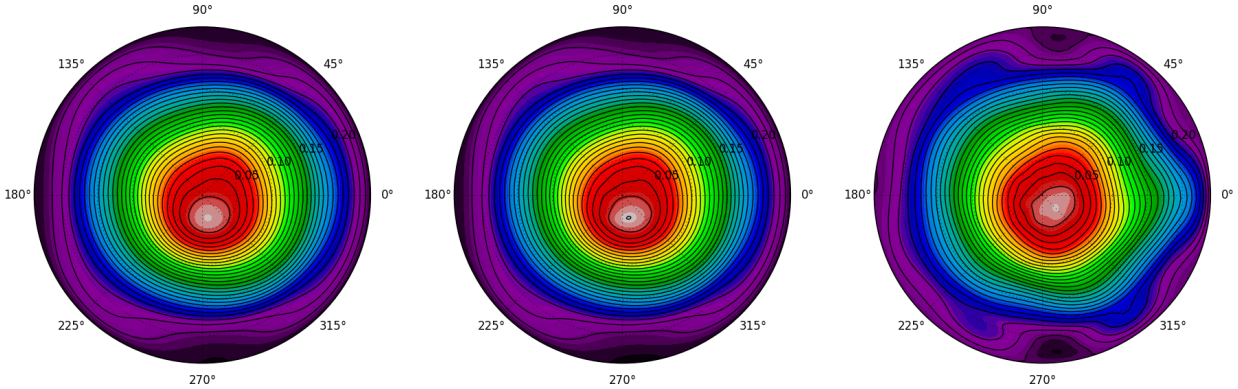

(a) Standard FB, $m = 5, l = 12$ (b) Standard FB, $m = 5, l = 15$ (c) Standard FB, $m = 8, l = 15$

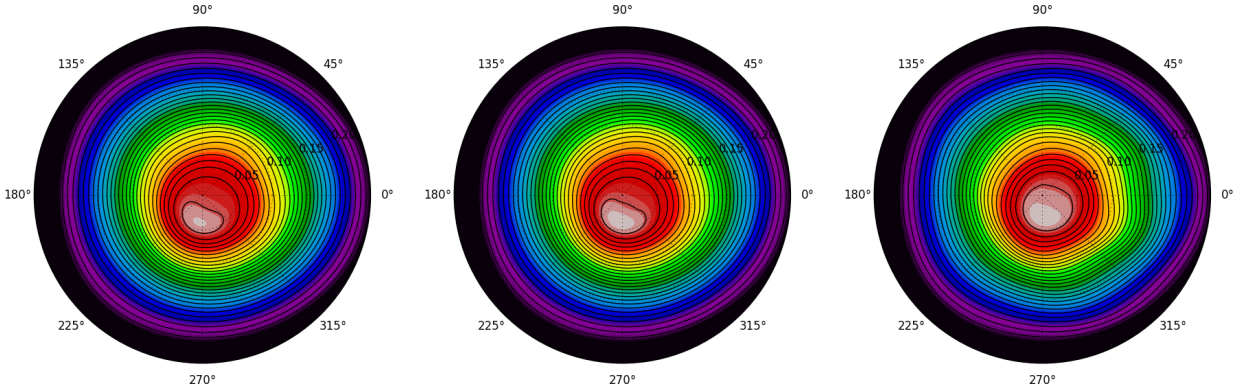

(d) Modified FB, $m = 5, l = 12$ (e) Modified FB, $m = 5, l = 15$ (f) Modified FB, $m = 8, l = 15$

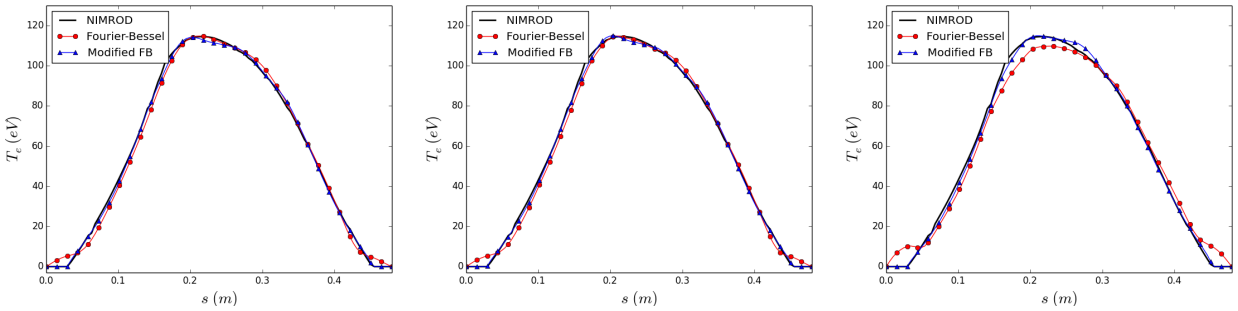

(g) Diagnostic Chord, $m = 5, l = 12$ (h) Diagnostic Chord, $m = 5, l = 15$ (i) Diagnostic Chord, $m = 8, l = 15$

Figure 4.4: Tomographic reconstruction results for the After test case. The top row contains contour plots of reconstructions using the standard Fourier-Bessel method for three cases having different numbers of basis functions. The middle row contains contour plots using the modified Fourier-Bessel. The last row contains plots of the reconstructed T_e for both methods versus the test data along the diagnostic chord for each case.

4.3 Tomographic Reconstructions of CTH Sawteeth

When signals from SXR cameras on CTH are used for tomographic reconstructions, distinct sawtooth relaxations can be clearly seen. The relaxations typically appear as an outward radial displacement and counter-clockwise poloidal rotation of the emissivity peak. The observed poloidal rotation may be due to the predominately $n = 1$ toroidal dependence of the sawtooth relaxation combined with the toroidal plasma flow in the experiment. After the relaxation is complete, the emissivity profile is broadened with a lower amplitude compared to before the relaxation. During the ramp period that follows a relaxation, the emissivity is seen to increase in intensity and become more peaked.

In Fig. 4.5, tomography reconstructions using the standard Fourier-Bessel method during a single sawtooth crash observed in shot 14112125 are shown. It should be noted that one of the central pinhole cameras in the $\theta = 300°$ camera was not functioning and this may affect the reconstructions. The choice of an SVD cutoff $C_{cutoff} = 0.10$ with $m = 5$ and $l = 12$ poloidal and radial basis numbers was informed by the test cases based on NIMROD data. However, there are many apparent artifacts in these reconstructions and they do not provide a clear picture of the sawtooth activity. When the SVD cutoff is raised to $C_{cutoff} = 0.15$ as shown in Fig. 4.6, reconstructed emissivities are smoother and the sawtooth relaxation can be clearly seen as a radial displacement and poloidal rotation of the core. In the last frames, reheating of the core after the relaxation is complete can be seen.

In Fig. 4.8 and Fig. 4.9 reconstructions of the crash using the modified Fourier-Bessel method, with two different values of C_{cutoff} are shown. The VMEC equilibrium used for these reconstructions was obtained using V3FIT. Magnet coil current values and the plasma current were set using the experimentally measured values. The equilibrium has a magnetic axis that runs through the location of maximum emissivity computed from just before the sawtooth crash by the standard Fourier-Bessel method and the edge of the equilibrium conforms to the limiters. Although the cameras are reportedly located at $\phi = 252°$, it is evident in Fig. 4.7 that the VMEC flux surfaces at $\phi = 256°$ better conform to the

reconstructed emissivity profiles in Fig. 4.6. Reconstructions using the flux surfaces at $\phi = 252°$ have many spurious features compared to reconstructions using flux surfaces at $\phi = 256°$. Therefore, the equilibrium flux surfaces at $\phi = 256°$ are used in the modified FB reconstructions.

Sawteeth are highly reproducible in CTH, so one should consider reconstructions of many relaxations from different experimental shots when informing an opinion of CTH sawteeth with tomographic reconstructions. In Figs. 4.10 and 4.11 modified FB reconstructions of a relaxation observed in shot 14110629 are shown for $C_{cutoff} = 0.1$ and 0.15 respectively. The result is remarkably similar to the sawtooth relaxation in shot 14112125 we considered.

This chapter considered some experimental observations of sawteeth in CTH. In the following chapters, CTH sawteeth with be explored by numerical simulation. Numerical sawteeth in an axisymmetric tokamak configuration will be explored first, as many of the considerations needed in obtaining solutions of repeated sawtooth relaxations for axisymmetric cases are also needed for non-axisymmetric configurations with a non-zero helical field.

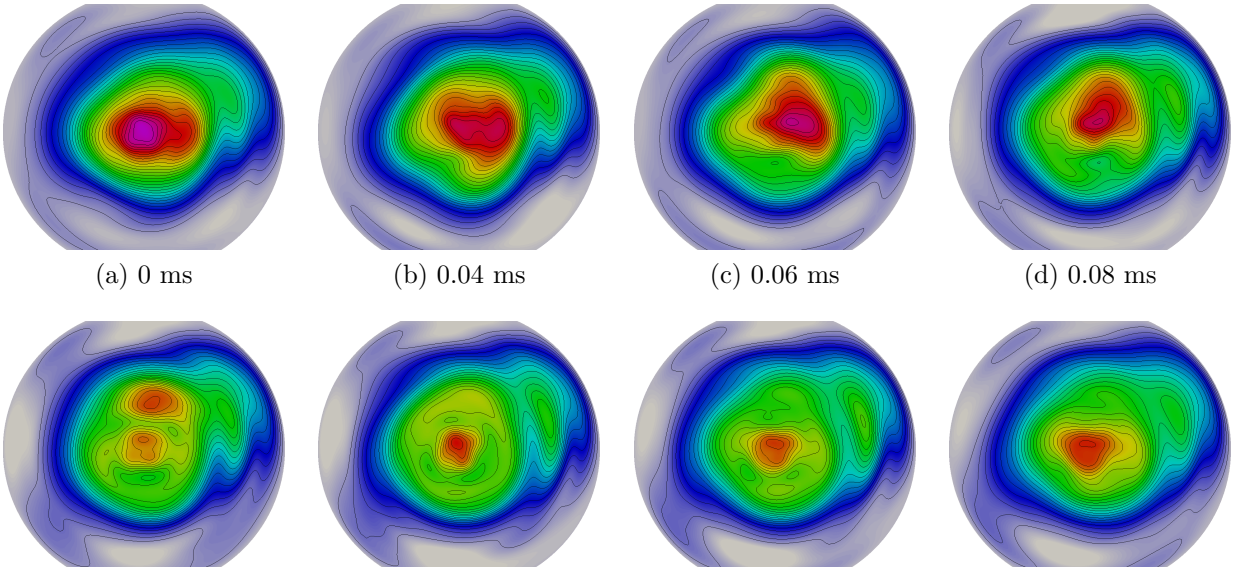

(a) 0 ms (b) 0.04 ms (c) 0.06 ms (d) 0.08 ms

(e) 0.10 ms (f) 0.12 ms (g) 0.16 ms (h) 0.20 ms

Figure 4.5: Tomographic reconstructions of a sawtooth crash from shot 14112125 using the standard Fourier-Bessel method. A minor radius of $a = 0.2$ was used with $m = 5$ and $l = 12$ poloidal and radial numbers and an SVD cutoff of 0.10. There are apparently many spurious features in the reconstructed emissivity profile.

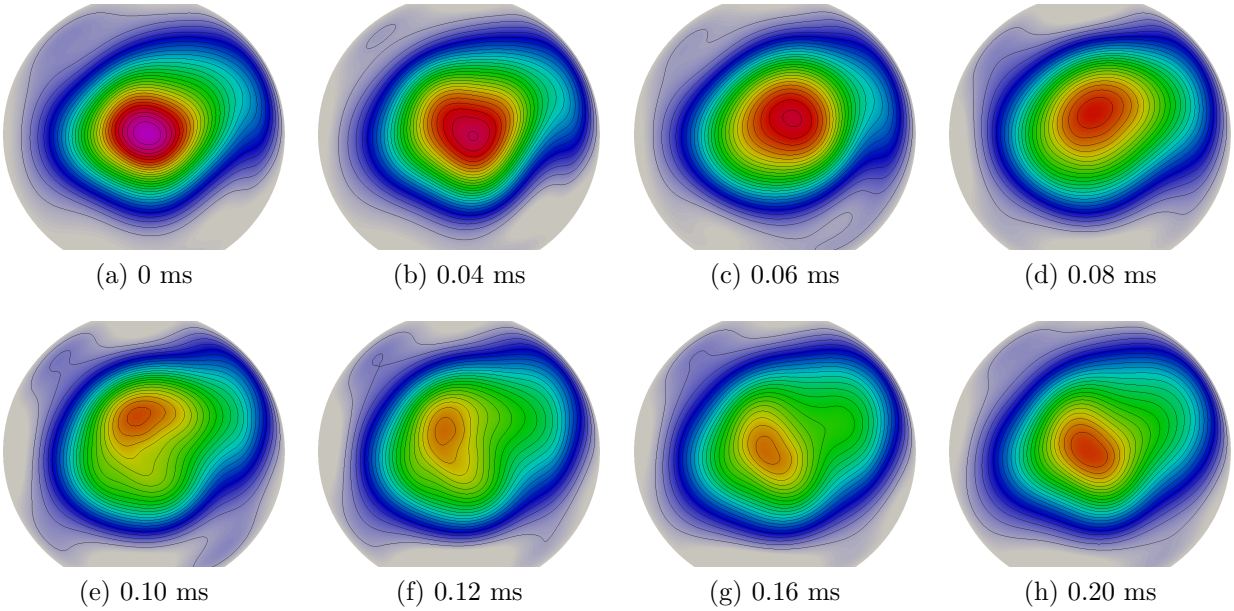

(a) 0 ms (b) 0.04 ms (c) 0.06 ms (d) 0.08 ms

(e) 0.10 ms (f) 0.12 ms (g) 0.16 ms (h) 0.20 ms

Figure 4.6: Compared to the reconstructions in figure 4.5, these reconstructions used an SVD cutoff of 0.15. With the larger SVD cutoff value, most of the spurious features are apparently removed. The radial shift and poloidal rotation of the hot core can be clearly seen.

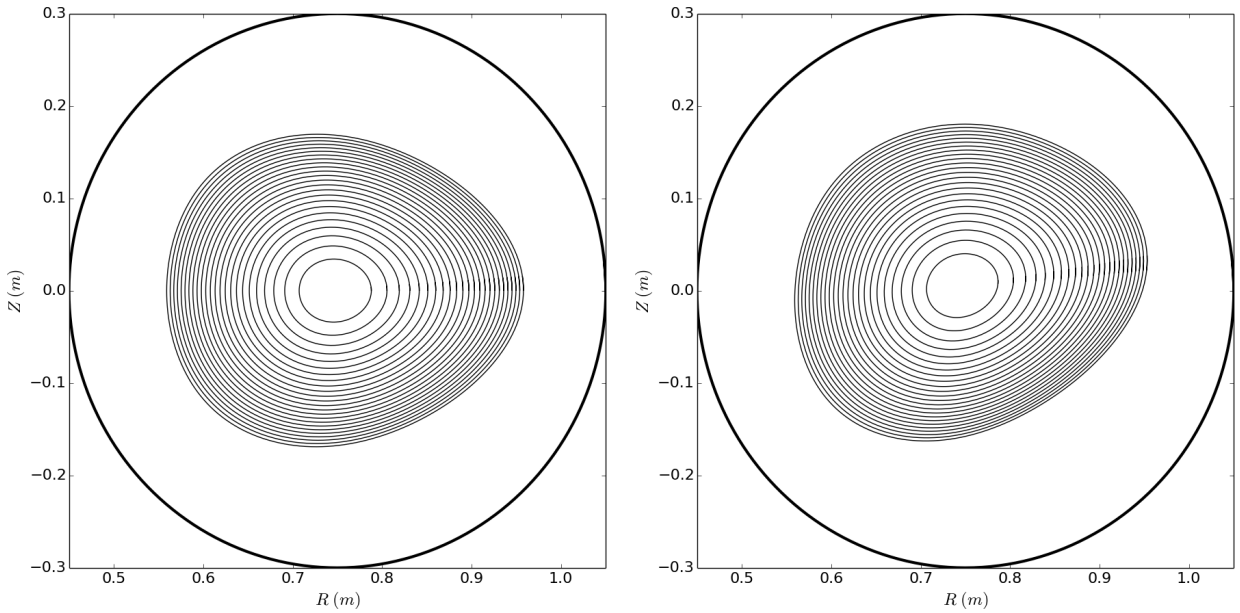

(a) $\phi = 252°$ (b) $\phi = 256°$

Figure 4.7: Flux surfaces of VMEC equilibrium used for tomography of shot 14112125 at $\phi = 252°$ and $\phi = 256°$. The surfaces at $\phi = 256°$ better conform to the emissivity profiles of Fig. 4.6.

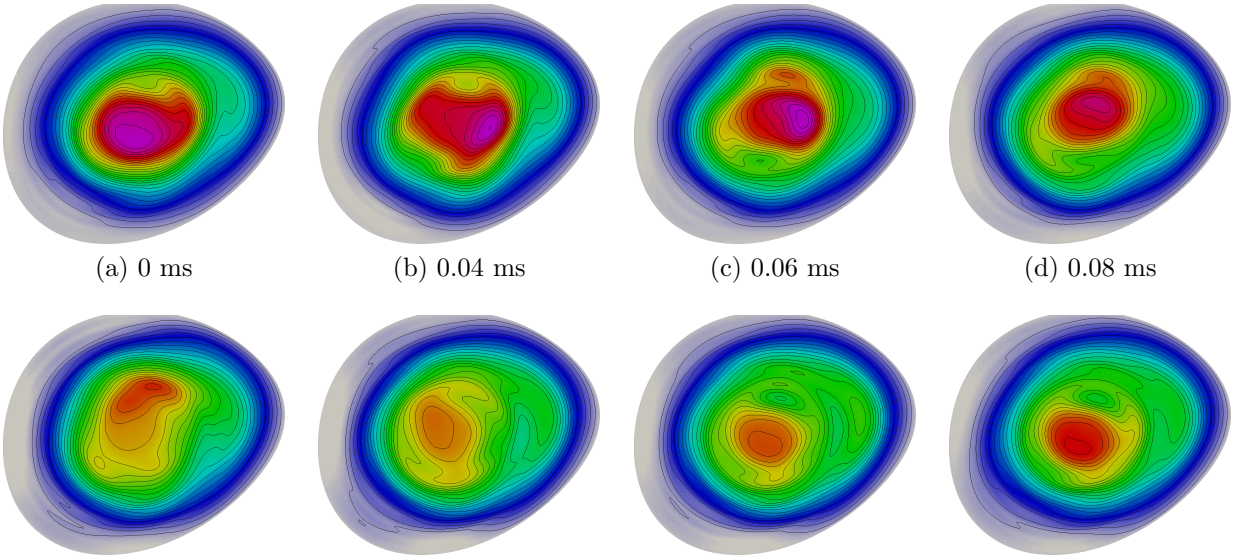

(a) 0 ms (b) 0.04 ms (c) 0.06 ms (d) 0.08 ms

(e) 0.10 ms (f) 0.12 ms (g) 0.16 ms (h) 0.20 ms

Figure 4.8: Reconstruction of the relaxation during shot 14112125. The modified Fourier-Bessel method with $m = 5$, $l = 15$ and $C_{cutoff} = 0.1$.

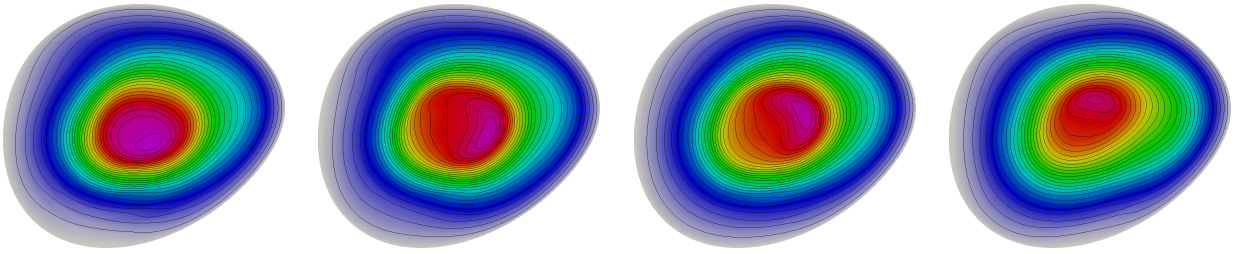

(a) 0 ms (b) 0.04 ms (c) 0.06 ms (d) 0.08 ms

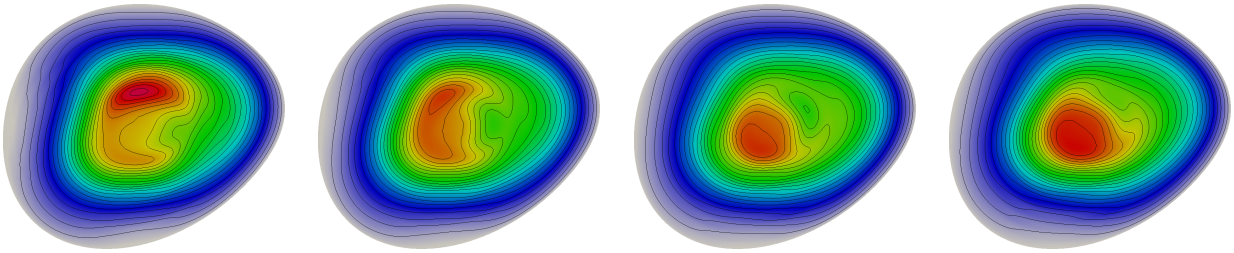

(e) 0.10 ms (f) 0.12 ms (g) 0.16 ms (h) 0.20 ms

Figure 4.9: Reconstruction of the relaxation during shot 14112125. The modified Fourier-Bessel method with $m = 5$, $l = 15$ and $C_{cutoff} = 0.15$.

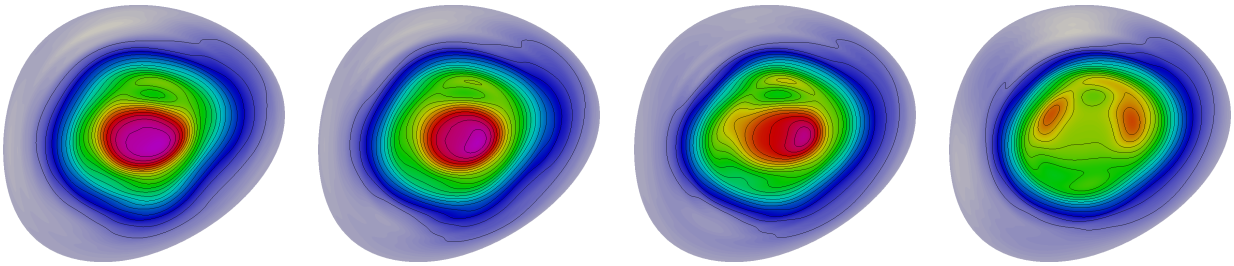

(a) 0 ms (b) 0.02 ms (c) 0.04 ms (d) 0.06 ms

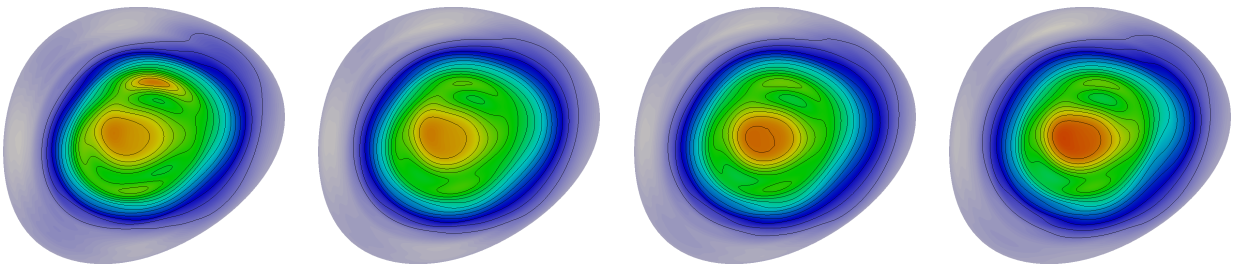

(e) 0.08 ms (f) 0.10 ms (g) 0.12 ms (h) 0.14 ms

Figure 4.10: Reconstructions of a relaxation during shot 14110629. The modified Fourier-Bessel method is used with $m = 5$, $l = 15$ and $C_{cutoff} = 0.10$.

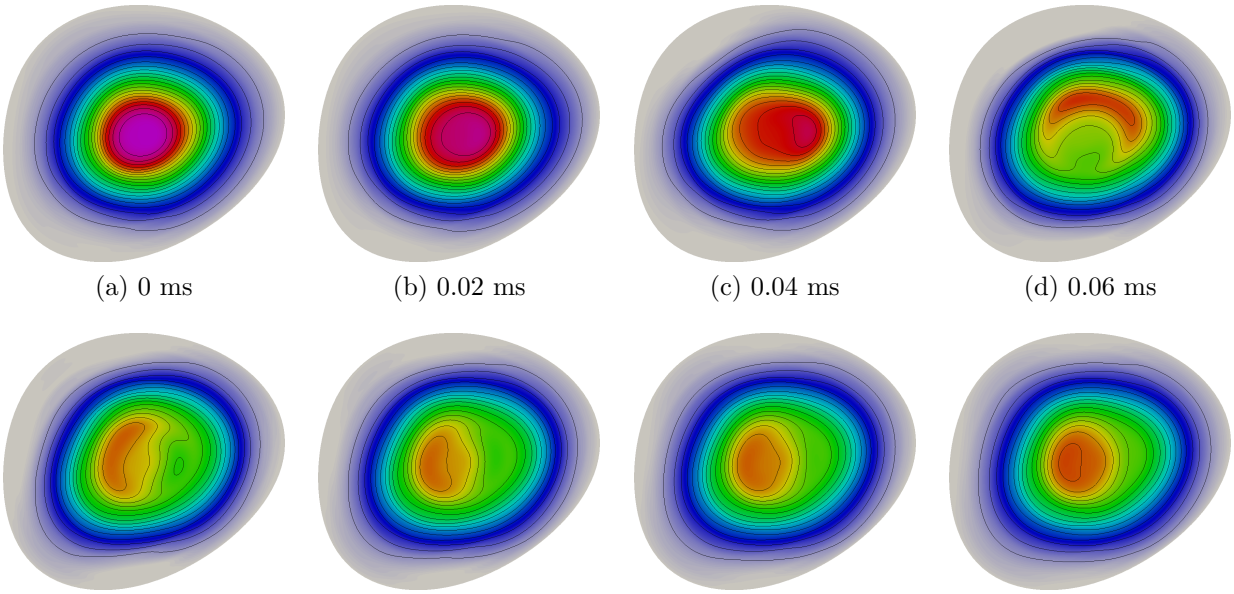

(a) 0 ms (b) 0.02 ms (c) 0.04 ms (d) 0.06 ms

(e) 0.08 ms (f) 0.10 ms (g) 0.12 ms (h) 0.14 ms

Figure 4.11: Reconstructions of a relaxation during shot 14110629. The modified Fourier-Bessel method is used with $m = 5$, $l = 15$ and $C_{cutoff} = 0.15$.

Chapter 5

Simulations of Sawteeth in a Tokamak

Simulations of CTH with no stellarator field, so that it is operating as a tokamak, are considered. There are a few reasons for considering the axisymmetric case before cases representative of CTH experimental discharges. First, axisymmetric MHD simulations of repeated sawteeth are well documented in the literature so this represents a natural starting point. Increasing the stellarator field represents a smooth transition from known to unknown. From a numerical point of view, which is discussed in detail later, the convergence properties become significantly different as the stellarator field is added. Obtaining numerically resolved solutions for the axisymmetric case is much less computationally demanding, making troubleshooting easier. From a practical point of view, NIMROD has features specifically intended for studying axisymmetric MHD problems, making troubleshooting even easier. When considering an axisymmetric equilibrium, NIMROD can be run in a linear mode. In nonlinear runs, axisymmetric diffusive sources can be used to maintain the equilibrium profile shapes over long time scales.

The mathematical problem to be solved is fully specified by the initial conditions, boundary conditions and model equations. The boundary conditions used are,

$$\begin{aligned} n(a) &= n_a \\ T(a) &= T_a \\ \vec{V}(a) &= 0 \\ \delta\vec{B}(a)\cdot\hat{n} &= 0 \\ \oint \vec{E}\cdot d\vec{l} &= V_{loop}(t) \end{aligned} \tag{5.1}$$

Magnetic boundary conditions are such that the normal component of the magnetic field at the boundary is fixed, which corresponds to a perfectly conducting wall with fields from external magnet coils frozen in. If the total plasma current is changed, eddy currents in the perfect conducting wall produce a vertical magnetic field that keeps the plasma roughly centered. A no-slip boundary condition is enforced for the velocity field. Dirichlet boundary conditions are applied to temperature and number density. A time varying loop voltage boundary condition $V_{loop} = V(t)$ is applied to the electric field to control the total plasma current I_{plasma}. A loop voltage, which is an EMF going the long way around the torus, is necessary to maintain constant I_{plasma} in the presence of electric resistivity since these simulations take place over a time interval comparable to the characteristic resistive diffusion time $\tau_r = \mu_0 a^2/\eta$.

Because the sawtooth instability and its nonlinear evolution is almost completely localized to the core of the plasma, use of these simple boundary conditions is justified [78]. Some other phenomena require more sophisticated boundary conditions. For example, simulation of a vertical displacement event requires a resistive wall boundary condition [79, 80].

Ideal MHD equilibria from the 3D equilibrium code VMEC are used for initial conditions. Refer to appendix A for more information on VMEC and the details of how these equilibria are loaded into NIMROD. The initial VMEC temperature profile is chosen so that $T \propto j^{3/2}$. The temperature profile is offset by the amount T_a everywhere in the domain. If a temperature offset is not added secondary activity after relaxations, described later in this section, tends to destroy flux surfaces in the outer region of the plasma. A uniform initial density profile $n = n_a$ is used. The initial current density profile is chosen somewhat arbitrarily with $q_0 > 1$, so that there is initially no sawtooth instability. It should be noted that the steady state behavior of MHD simulations of repeated sawtoothing is known to be somewhat insensitive to initial conditions.

n_a	$10^{19}\ m^{-3}$
T_a	$30\ eV$
T_{ref}	$150\ eV$
ν	$10\ m^2/s$
$\chi_{\perp,0}$	$10\ m^2/s$
$\chi_{\parallel}$	$10^7\ m^2/s$
κ_{divb}	$5 \cdot 10^4\ m^2/s$
η_0	$3.14 \times 10^{-6}\ \Omega m$
I_{plasma}	$105\ kA$
$V_{loop}(t \to \infty)$	$11.6\ V$

Table 5.1: Values of the model parameters used for the tokamak case.

The values for the model equation (Eq. 2.1) parameters are shown in Table 5.1. These parameters lead to self-consistent MHD profiles having plasma parameters that should be roughly consistent to those of CTH plasmas.

Starting from initial conditions, the total plasma current is ramped up to the appropriate value at the beginning of the simulation. There is a long, quiescent "ramp phase" at the beginning with no sawtooth activity. The temperature profile quickly relaxes to a thermal equilibrium that is consistent with the transport model being used. The central safety factor q_0 begins slowly falling below unity on the resistive diffusion time scale. That the relaxation of the temperature profile occurs much more rapidly than the relaxation of the current density profile is explained by noting that the characteristic energy confinement time $\tau_E \approx 0.29\ ms$ is much shorter than the characteristic resistive diffusion time $\tau_r = 55\ ms$. The approximate value for τ_E was computed by using Visit [81] to integrate the thermal energy density $\rho_E = 3nk_B(T_e + T)/2$ and the volumetric heating power ηJ^2 over the region inside the LCFS and taking the ratio of these quantities.

After $q_0 < 1$, the sawtooth mode becomes unstable, gets excited at a low amplitude and grows exponentially until it reaches the non-linear phase of evolution. The eigenfunction (Fig. 5.1) represents a rigid displacement of the central part of the plasma core with a $n = 1$ variation in the direction. There are several types of such instabilities which drive sawteeth.

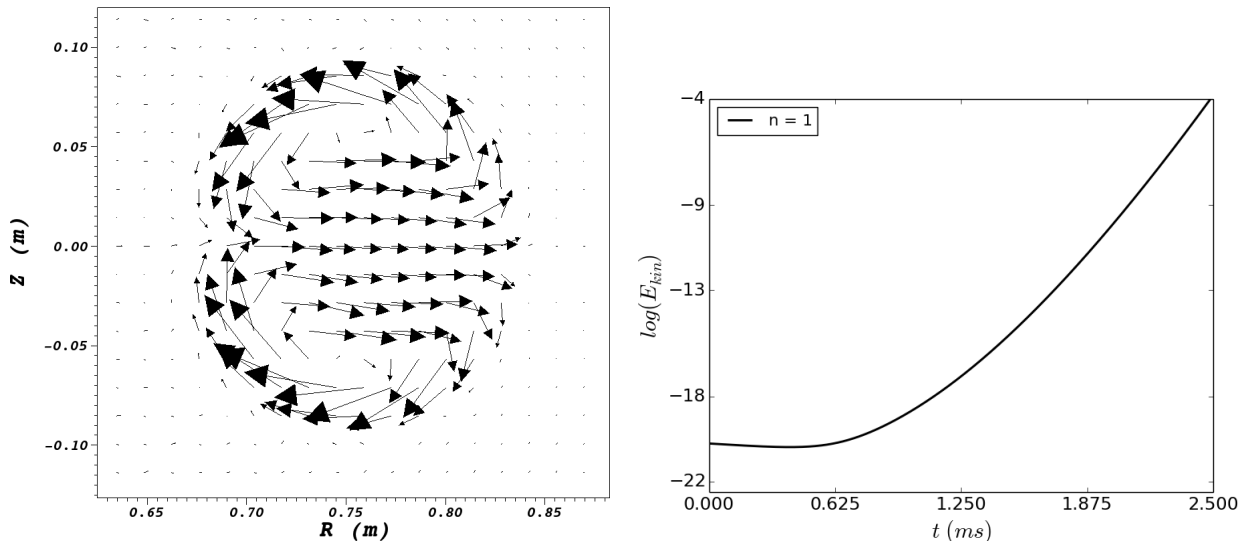

(a) (b)

Figure 5.1: (a) Projection of the velocity field onto the plane at $\phi = 0°$ during the linear phase of evolution. This flow at $\phi = 0°$ can be described as an outward, incompressible, rigid displacement. (b) The kinetic energy of the $n = 1$ Fourier component of the solution fields grows exponentially with a nearly constant slope after the mode is excited. The growth rate of the mode can be figured by finding the slope, where $slope = 2\gamma$.

It was determined that this sawtooth mode is a toroidal generalization of the $m = 1$ visco-resistive internal kink mode. The determination was made by confirming that the growth rate has the correct scaling with S and by looking at the form of the eigenfunction at the resonant surface (see Fig. 1.4). Finding the scaling of the growth rate was accomplished by taking the $n = 0$ profiles of the solution at times during the linear growth phase of the sawtooth mode. Then, these profiles are used as equilibria for running NIMROD in linear mode. The resistivity coefficient η_0 was scanned in a series of linear runs, and the scaling of the growth rate versus Lundquist number found to be nearly $\gamma \propto S^{-2/3}$, as illustrated in Fig. 5.2, which is the scaling for the visco-resistive internal kink [82].

The nonlinear phase of evolution begins when the mode eigenfunction grows sufficiently large compared to the equilibrium fields. It is well described by the Kadomtsev relaxation process. The core inside the $q = 1$ surface is radially displaced outward into a helical reconnection current layer. The near singular current layer and reconnection flows are pictured in Fig. 5.3. A series of Poincaré plots are shown in Fig. 5.4 that illustrate the core reconnecting

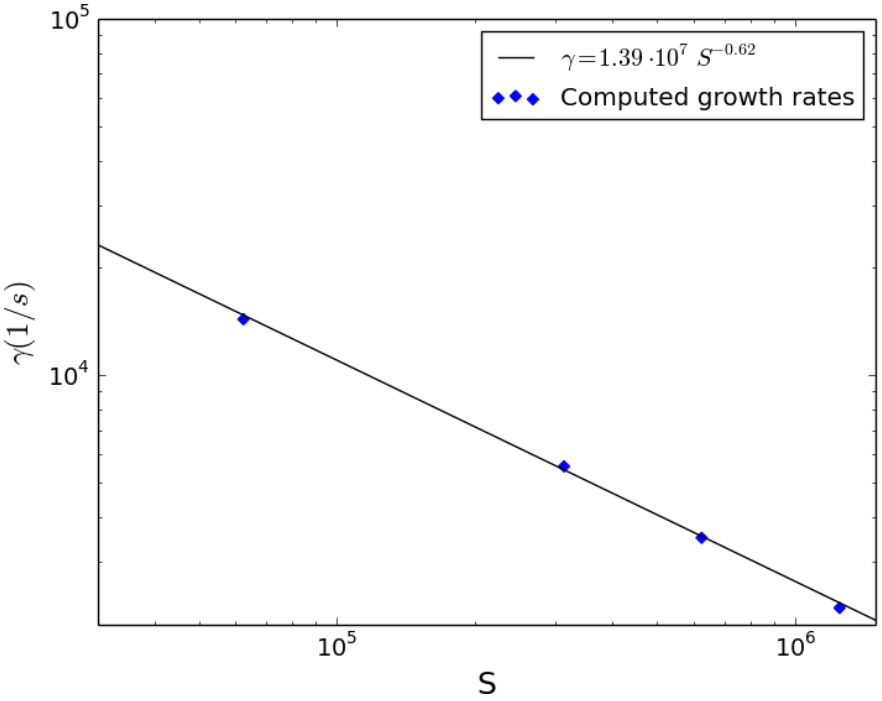

(a)

Figure 5.2: In simulations of a tokamak similar to CTH, the sawtooth instability has approximately visco-resistive internal kink growth rate scaling $\gamma \propto S^{-2/3}$.

and being replaced by a growing island. Recall that the resistivity is very small so that the magnetic field lines are nearly frozen into the plasma in regions outside of the reconnecting current layer. After the process is complete, the central current density is flattened and reduced in amplitude so that $q > 1$. The temperature profile also becomes somewhat flattened with a lower central amplitude. The relaxation ejects thermal energy from the core to the outer region of the plasma. A comparison of the safety factor and temperature profiles before and after the relaxation is shown in Fig. 5.5.

The solution we obtained for the tokamak configuration undergoes 16 nearly periodic relaxations. Presumably, relaxations would continue for as long as the numerical solution is advanced. The energies of each toroidal Fourier number are shown in Fig. 5.6. These quantities serve as a proxy for the amplitude of each Fourier component's contribution to the solution fields. Although the linear mode is represented with only the $n = 1$ fields, all Fourier numbers are involved in representing the nonlinear relaxation. Also, T_e is plotted

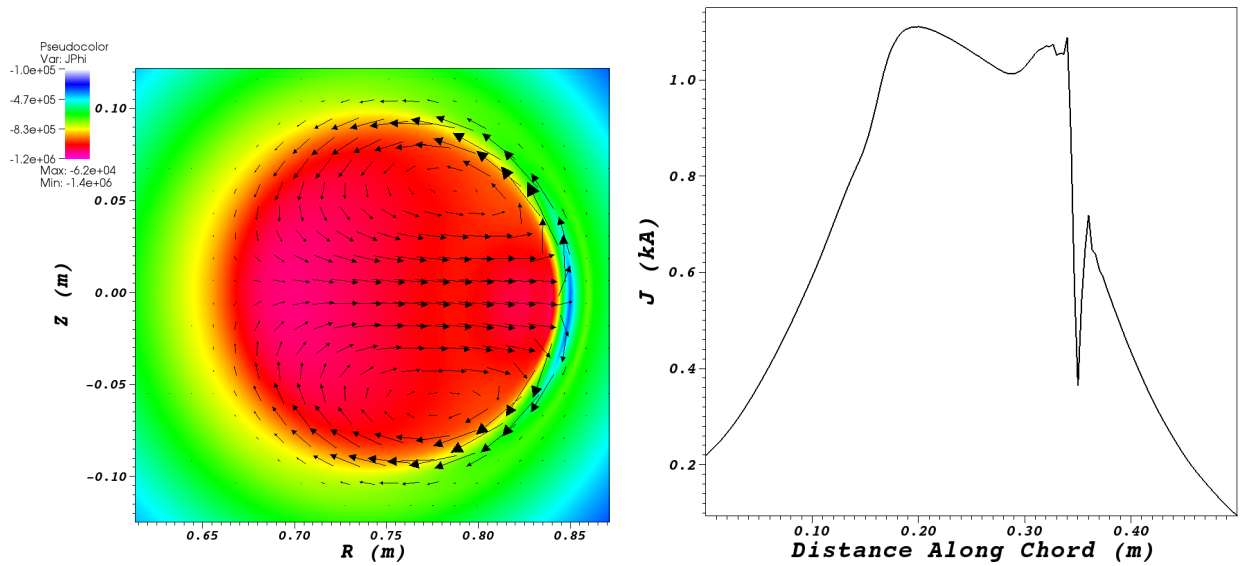

(a) (b)

Figure 5.3: (a) The non-linear evolution of this mode is the formation of a Sweet-Parker like reconnection layer and reconnection of flux inside the core. The arrows indicate the flow, with the relative magnitude given by the size of the arrows. In (b), the toroidal current density is plotted along a chord passing through the plasma core and reconnection layer. The near discontinuity at the reconnection layer can be clearly seen.

versus time at points increasingly distant from the center of the plasma core. In the core, the temperature rapidly drops at relaxations but the region away from the core is rapidly heated by heat being ejected from the core. Experimentally, the mixing radius can be determined by looking at which SXR signals are inverted. SXR signals from sensors pointed into the central core show a slow ramp up with a sharp drop, but signals from sensors pointing to regions outside the mixing radius are inverted with crashes appearing as a sharp upward spike. We note that the temperature trace of the central chord does not really have a sawtooth shape in simulations. In fact, the temperature trace at the center looks more like a square wave. This may be explained by noting that the sawtooth period, approximately $\tau_{saw} = 0.56\ ms$, is a considerably longer than the energy confinement time $\tau_E \approx 0.29\ ms$. Therefore the core re-establishes thermal equilibrium quickly, well before the next relaxation. A more sawtooth-like signal is expected for $\tau_E \gtrsim \tau_{saw}$ [10].

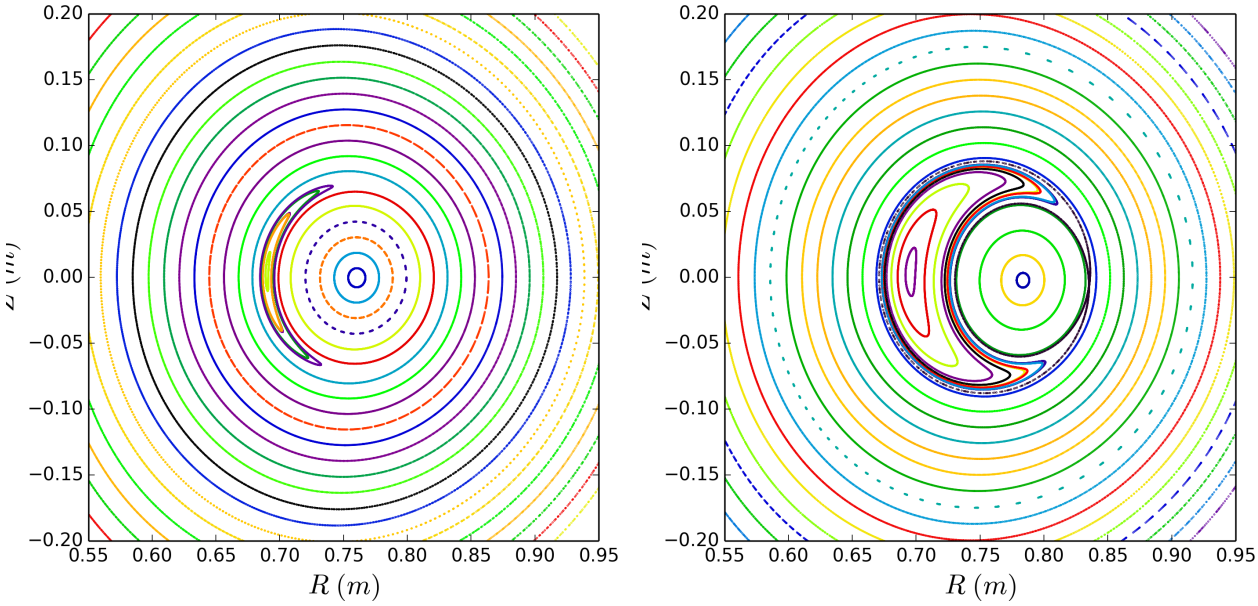

(a) 0 ms

(b) 0.22 ms

(c) 0.28 ms

(d) 0.34 ms

Figure 5.4: Poincaré plots showing the evolution of a sawtooth relaxation. An island at the $q = 1$ surface grows rapidly, pushing the plasma core into a resistive reconnection layer on the other side of the $q = 1$ surface. The final state is shown in (d), where the entire plasma core has completely reconnected and the center of the island has become the new magnetic axis.

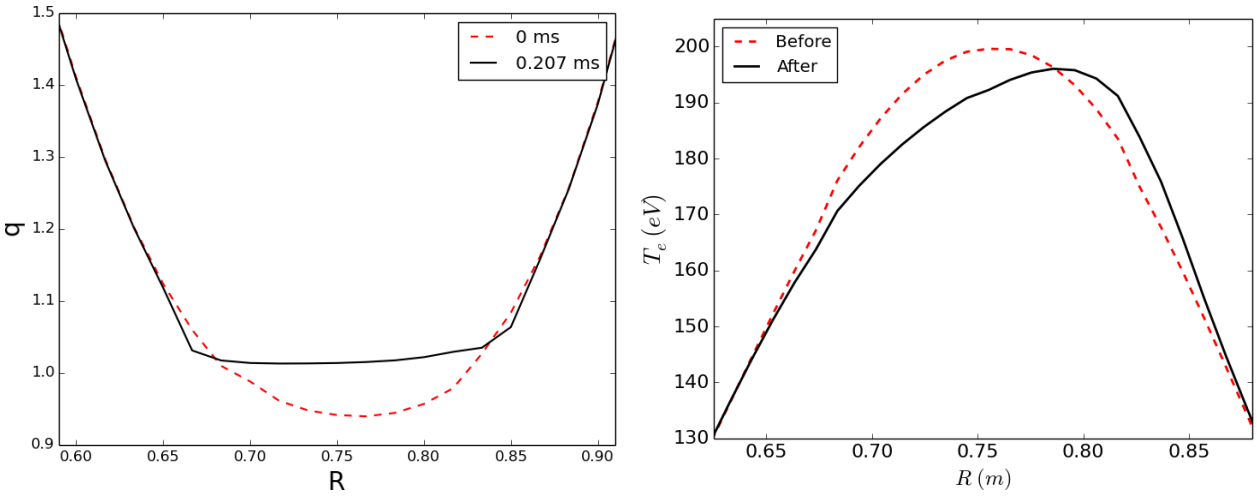

Figure 5.5: The q profile shortly before and shortly after the relaxation is shown in (a). After the relaxation, $q > 1$ and the q profile has a broader, more square-like shape. In (b), the temperature is shown before and after the relaxation.

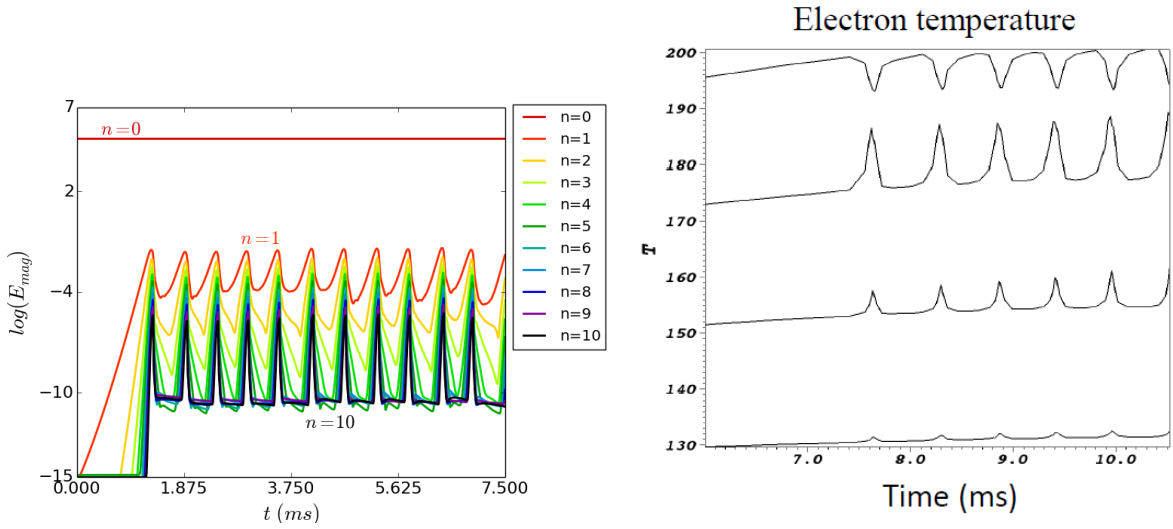

(a) (b)

Figure 5.6: (a) The energies of each toroidal Fourier number of the magnetic field is plotted vs. time. These quantities are a proxy for the relative contribution of each Fourier component to the solution fields. (b) The temperature is plotted vs. time at points increasingly distant from the magnetic axis. The temperature in the core sees repeated crashes that coincide with spikes in the temperature outside the core. This is a classic experimental characteristic of sawteeth that is recovered in the simulations.

The loop voltage asymptotically approaches a steady value of 11.5 V. This is greater than the loop voltage in CTH, which is around 4 V during sawtooth activity. This suggests that the resistivity of CTH plasmas may be somewhat lower than that of the simulated plasma. The central value of the Lundquist number during this simulation is approximately $S_0 \approx 1.7 \times 10^5$.

A number of challenges were overcome in seeking MHD solutions with repeated sawtoothing. First, considerations were made to prevent islands from growing large in the outer region of the plasma. The growth of these islands coincides with a relaxation. The broad profile shape after a relaxation is conducive to tearing modes. The islands overlap and cause much of the domain outside of the mixing radius to have stochastic magnetic fields (Fig. 5.7). This gets worse as the total current is increased, leading to a broader q profile after a relaxation. A large $m/n = 2/1$ island is especially notable. This stochasticity outside the mixing radius has been seen in many previous works on the simulation of repeated sawteeth and is often not addressed. It has been noted that stochasticity outside the mixing radius may not occur after a relaxation when the two-fluid equations are used [83]. Because we are only interested in studying sawtoothing with resistive MHD here, sources and boundary conditions are adjusted to give profile shapes that are not susceptible to this tearing mode activity. $T_e(a)$ is set to 30 eV and the total plasma current is chosen so that the $q = 2$ surface is near the perfectly conducting wall. The change in profile shapes, with a lower value of η at the $q = 2$ surface and wall stabilization are effective in suppressing the tearing modes.

Obtaining solutions that reach an oscillating steady state requires careful selection of dissipation, diffusion and source parameters, including $\chi_\perp$, $\chi_\parallel$, ν and I_{plasma}. We see in Figure 5.8 that the solution with a smaller I_{plasma} undergoes a couple of relaxations but quickly reaches a helical equilibrium that does not oscillate. When I_{plasma} is increased slightly, the solution reaches a steady state with repeated Kadomtsev relaxations. Some amount of trial and error is necessary to get numerical solutions with oscillating steady states. However, many past studies have sought to characterize the regions of parameter

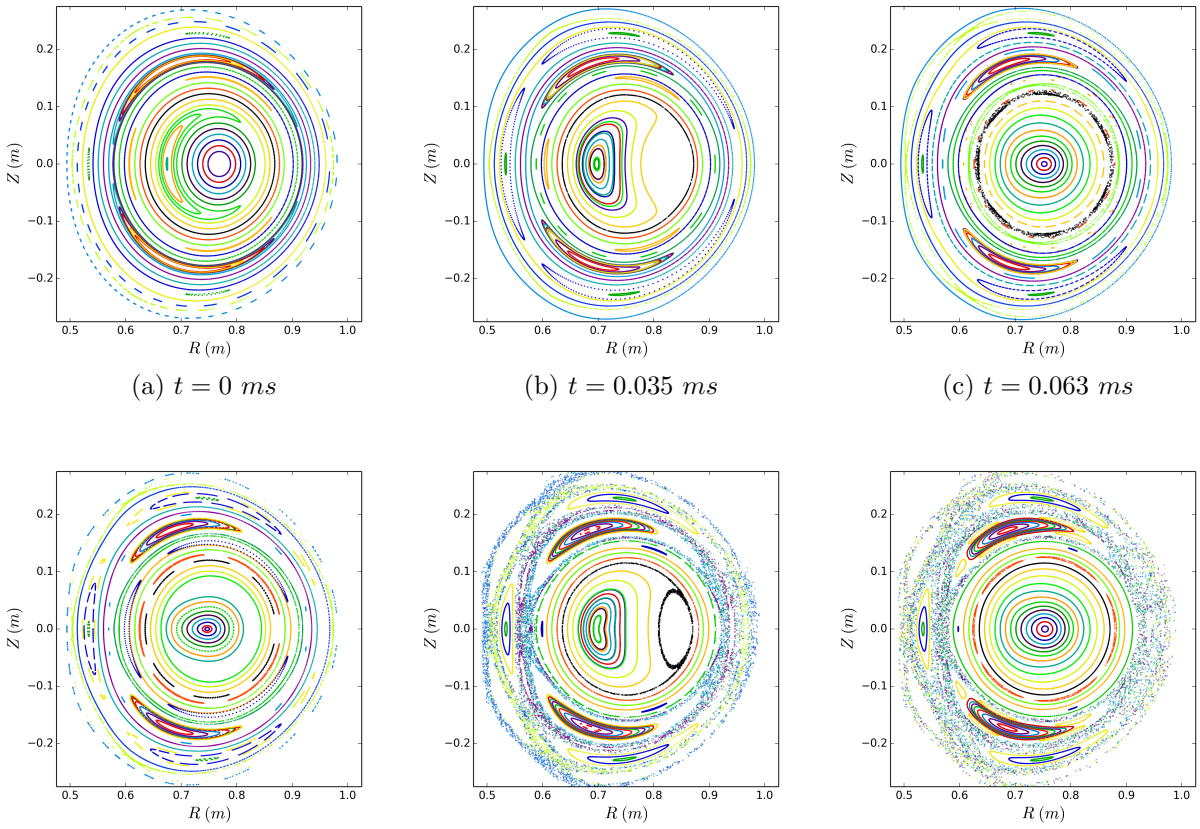

(a) $t = 0\ ms$ (b) $t = 0.035\ ms$ (c) $t = 0.063\ ms$

(d) $t = 0.12\ ms$ (e) $t = 0.23\ ms$ (f) $t = 0.26\ ms$

Figure 5.7: Poincaré plots over an interval having two relaxations are shown. The boundary condition $T_a = 0.5\ eV$ was used. After a relaxation, islands grow and overlap causing stochasticity over large parts of the domain. Increasing the electron temperature at the boundary T_a to 30 eV and setting I_{plasma} changes profile shapes to have shallower gradients and significantly increases the resistivity at rational surfaces near the edge.

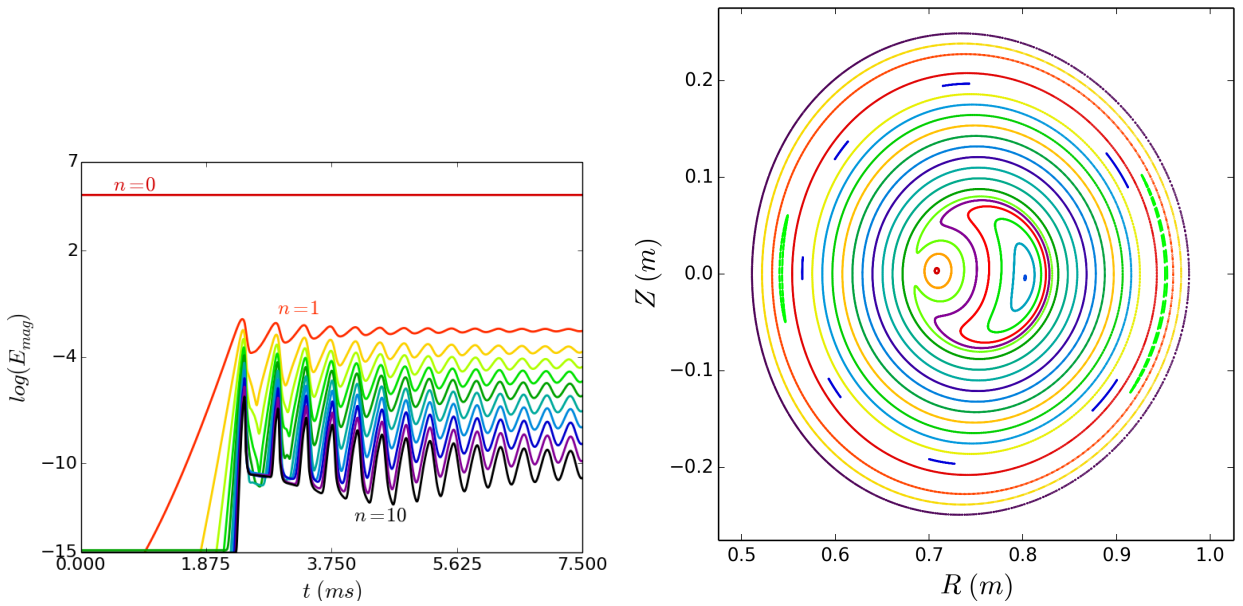

(a) (b)

Figure 5.8: MHD solutions of sawtoothing will only reach a steady state having repeated relaxations in certain regions of parameter space. The pictured solution was obtained by reducing the total plasma current from $I_{plasma} = 105\ kA$ to $I_{plasma} = 102.5\ kA$. Oscillations decay as seen in (a) and the system reaches a helical steady state. A Poincaré plot of the helical steady state is shown in (b).

space where solutions reach an oscillating steady state. As a rule, oscillating solutions are found for small $\chi_\perp$ and poloidal beta β_p [84]. The poloidal beta is defined $\beta_p \equiv 2\mu_0\langle p\rangle / B_\theta^2(a)$, where $\langle p\rangle$ is the volume averaged pressure, and in this study it is useful to think of it as a proxy for the total plasma current I_{plasma}. When larger values of $\chi_\perp$ or β_p are used, solutions will tend to relax to a non-oscillating helical steady state. Also, cases without a sufficiently strong parallel thermal conductivity were found to reach a helical steady state that does not oscillate.

In a simulation where the plasma current was 115 kA instead of 105 kA, rapid rearrangement of flux surfaces was observed immediately after relaxations. This sort of secondary activity leading to a rearrangement of flux surfaces was noted in several other simulations including simulations having a non-zero stellarator field. The secondary activity always

disappears when the plasma current is decreased under some threshold value. No model parameters besides plasma current were changed. See figure 5.9 for Poincaré plots showing how the flux rearranges. In trying to identify this phenomena, it was noted that the evolution of the flux tubes resembles what is pictured in reference [85] which explains the observation that $q_0 < 1$ after sawtooth relaxations in terms of a rapid rearrangement of flux after a Kadomtsev-like reconnection. However, these simulations do not see a significant change in q_0 from the rearrangement.

To investigate the flux rearrangement phenomenon, the $n = 0$ profiles corresponding to plot (b) in fig. 5.9 were taken as an equilibrium and NIMROD was run in linear mode as various model parameters were changed. An $n = 1$ unstable mode was found with an eigenfunction that resembles the quasi-interchange mode. The equilibrium and mode eigenfunction are shown in Fig. 5.10. It was found that there is no instability if an axisymmetric model is used for the resistivity η. This motivated exploring how the growth rate γ varies with the parallel thermal conductivity, since with a Spitzer model a large parallel thermal conductivity has the effect of equalizing variations in η along field lines. Indeed it was found that as $\chi_{\parallel}$ is increased, the growth rate decreases. Therefore, this instability may be related to the rippling instability [86].

In conducting sawtooth simulations, it was noticed that first relaxation is sometimes larger than successive relaxations. This is because, for the first relaxation, the unstable $n = 1$ mode is excited with only a small amount of energy. Linear mode growth then occurs for a considerably longer period of time than following cycles before reaching the non-linear phase of evolution. q_0 continues to drop below unity during the extended period of linear growth, so the first relaxation starts with a lower value of q_0.

The discussion in this chapter presented how numerical solutions of repeated relaxations are obtained for an axisymmetric case. This general procedure will be followed in the next chapter where solutions of repeated relaxations with a non-zero helical field. Several considerations were necessary in obtaining solutions that reach a steady state with repeated

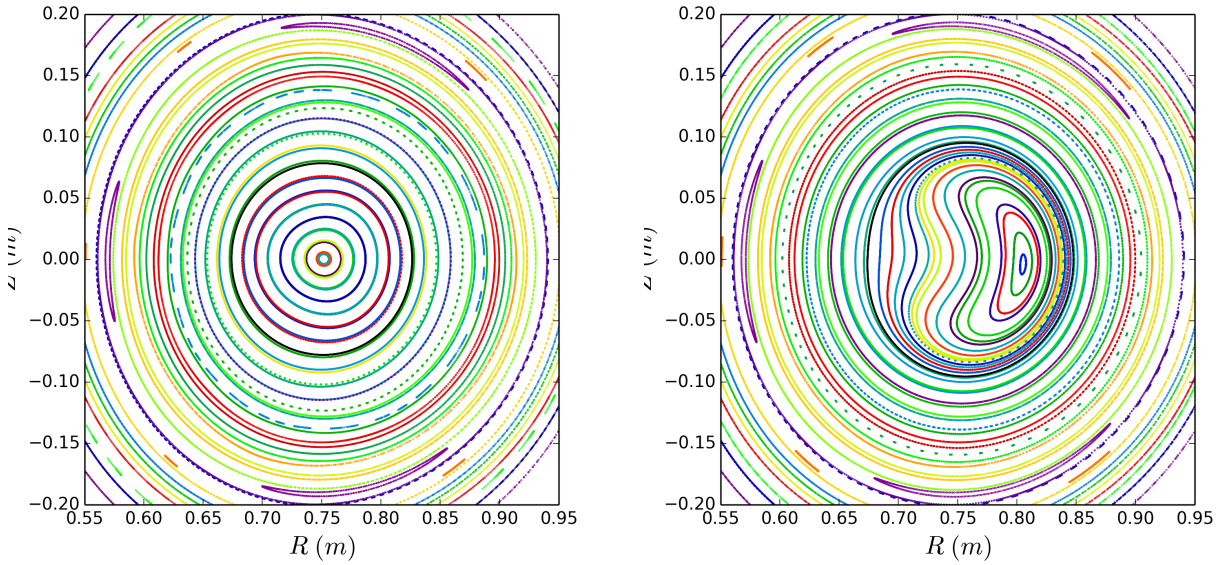

(a) 0 ms (b) 0.063 ms

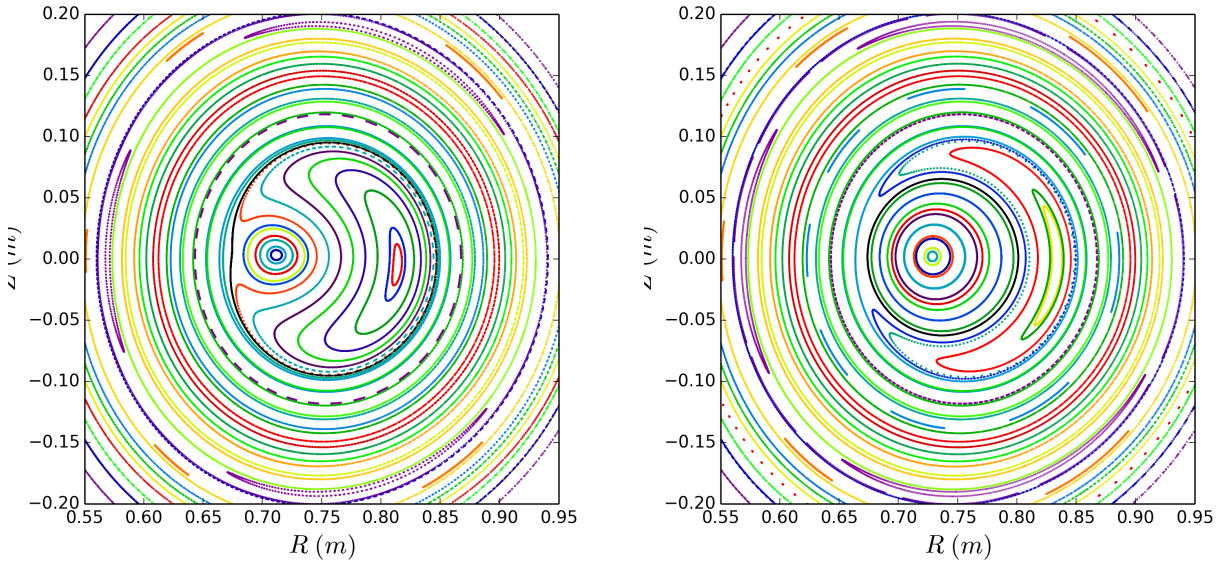

(c) 0.094 ms (d) 0.14 ms

Figure 5.9: Poincaré plots showing rapid rearrangement of flux surfaces immediately after complete reconnection. This occured every relaxation when the plasma current was increased from 105 kA to 115 kA.

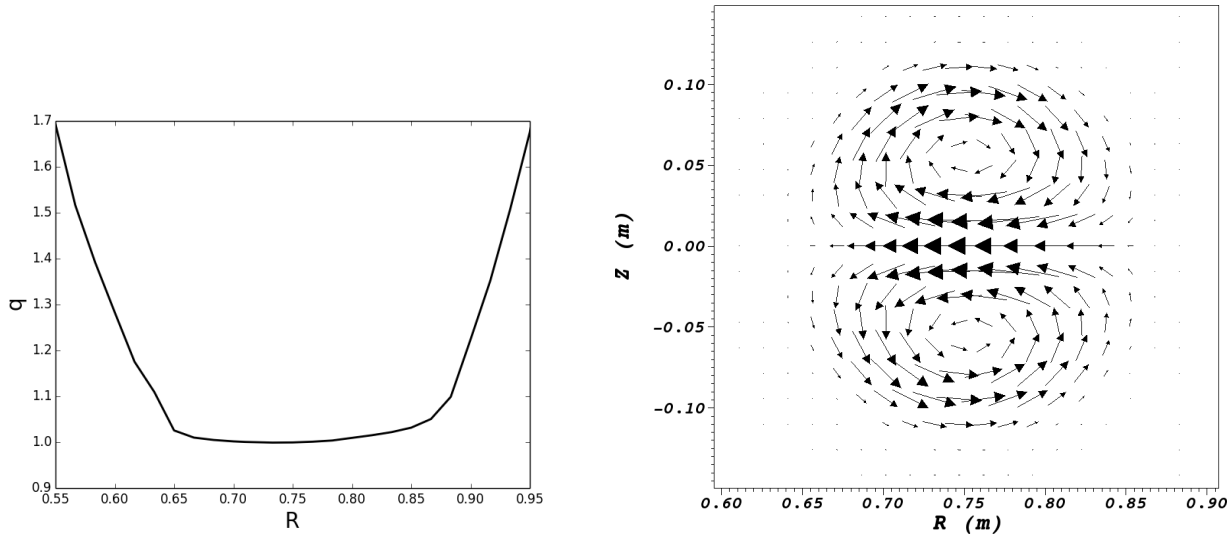

(a) (b)

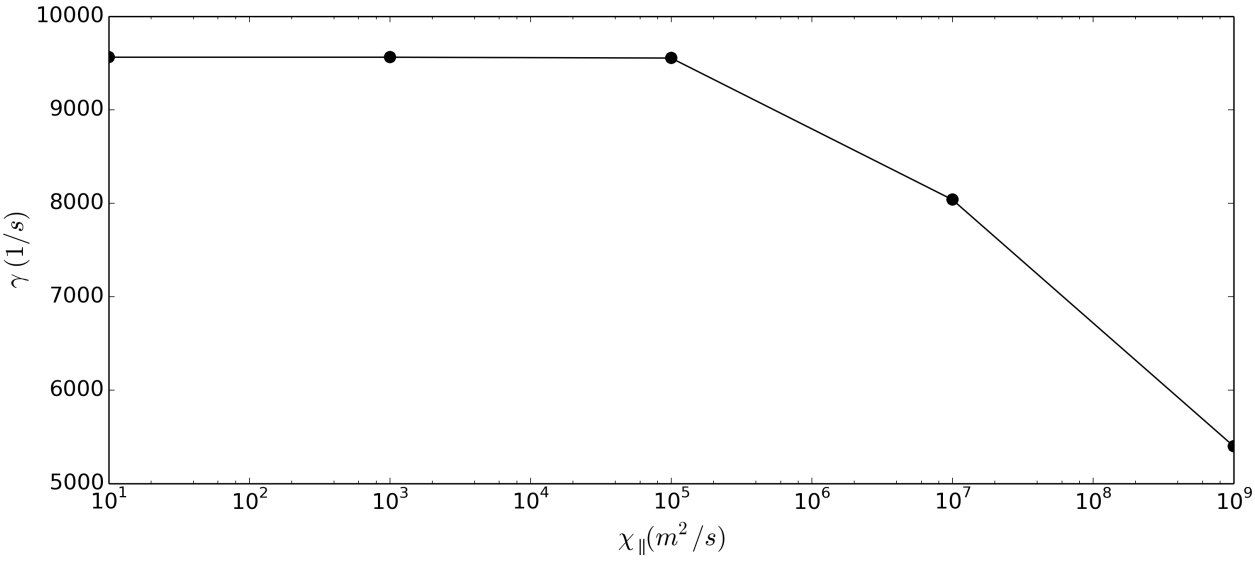

(c)

Figure 5.10: The q profile of the equilibrium used to study the flux rearrangement phenomenon (a) and the projection of the eigenfunction of the unstable $n = 1$ mode, that resembles a quasi-interchange mode, onto the poloidal plane (b). The size and direction of the arrows corresponds to the magnitude and direction of the flow (units are arbitrary since this is a linear eigenmode). In (c), the growth rate is plotted as a function of parallel heat conductivity $\chi_\parallel$.

relaxations. For example, it was seen that the solution will reach a steady state having repeated relaxations only in certain regions of parameter space. The same considerations must be taken for non-axisymmetric cases.

Chapter 6

Simulations of Sawteeth in CTH

Numerical solutions of sawtoothing in cases with three-dimensional, non-axisymmetric shaping from the CTH stellarator field are described in this chapter. These results provide insight into the qualitative differences and similarities between sawtooth relaxations in the non-axisymmetric and axisymmetric cases. It should be noted that the goal is not exact quantitative agreement with observations from the experiment. A key experimental finding is that τ_{saw} is correlated with ι_{vac}. These results provide insight into the first principles behind this correlation.

A family of four configurations with increasing helical stellarator field strength are considered. The configurations range from zero stellarator field with CTH operating as an axisymmetric tokamak to a case representative of an experimental sawtoothing shot with a high amount of stellarator field. In Fig. 6.1, three-dimensional plots of temperature isosurfaces which roughly correspond to the LCFS are shown for each configuration. Increased shaping of the plasma is evident as ι_{vac} is increased.

In all cases the plasma current provides most of the rotational transform as in a tokamak. The safety factor profiles are tokamak-like in the sense that q monotonically increases as one moves radially outward from the magnetic axis. For these configurations, the vacuum stellarator fields needed to compute ι_{vac} are obtained by running V3FIT to compute a VMEC equilibrium that has zero plasma current and pressure. V3FIT varies two parameters, the vertical field coil current I_{tvf} and the toroidal flux at the plasma-vacuum interface *phiedge*, to obtain an equilibrium that conforms to the limiters and is horizontally centered with an average location for the magnetic axis at $R = 0.75\ m$. The horizontal position is controlled with I_{tvf} and *phiedge* controls the minor radius.

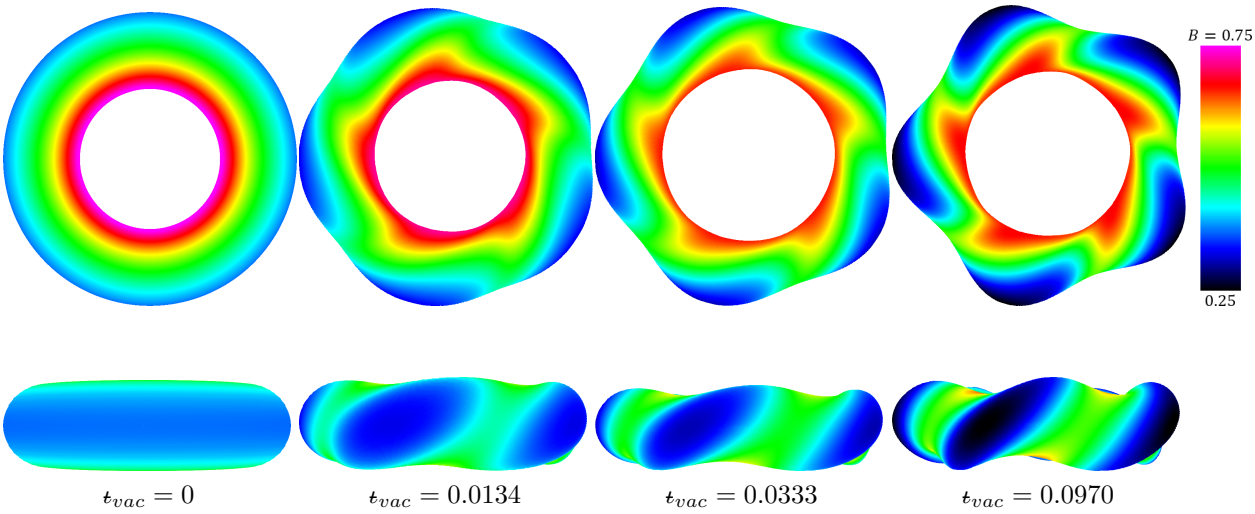

Figure 6.1: Plots of the electron temperature isosurface corresponding to the average temperature of the last closed flux surface for each configuration immediately after a sawtooth relaxation. The standard deviation of the electron temperature within the LCFS is quite small for each case. The color indicates with strength of the magnetic field.

Besides helically deforming the magnetic topology, the stellarator field has the effect of creating chains of small equilibrium islands that tend to become larger with increasing ι_{vac}. Also it can be seen from Table 6.1 that the generalized minor radius of the last closed flux surface tends to decrease with increasing ι_{vac}. There are several definitions one may use for the generalized minor radius of a flux surface, but in this work the following definition is used, where v is the volume enclosed by the flux surface and a_s is the surface area of the flux surface.

$$r_{lcfs} = \frac{2v}{a_s}$$

To make the calculation more convenient, the volume and surface area of the temperature isosurface corresponding to the average temperature of the last closed flux surface is used. The last closed flux surface is well approximated by this temperature isosurface because of the large parallel thermal conduction used in the simulation. With this approximation, calculating r can be easily accomplished with Visit.

ι_{vac}	0	0.0134	0.0333	0.0970
v (m^3)	1.05	0.922	0.665	0.643
a_s (m^2)	11.5	11.6	10.3	11.0
r_{lcfs} (m)	0.184	0.159	0.129	0.117

Table 6.1: The generalized minor radius gets smaller as the strength of the helical field is increased.

Both the equilibrium islands and the reduced minor radius will decrease the energy confinement time τ_E given the transport model under consideration. The rapid parallel thermal conduction allows thermal energy to efficiently flow across island chains. Given an equilibrium having closed nested flux surfaces, the energy confinement time will be proportional to the square of the generalized minor radius because of the diffusive model for perpendicular heat transport as shown here,

$$\begin{aligned}
\tau_E =& \frac{E_{th}}{P_{loss}} \\
=& \frac{\iiint_{r<r_{lcfs}} \rho_E \; dv}{\oiint_{r=r_{lcfs}} \vec{q} \cdot \hat{n} \; da} \\
=& \frac{\langle \rho_E \rangle r_{lcfs}}{2 q_{\perp,lcfs}} \\
\approx& \frac{\langle \rho_E \rangle r_{lcfs}^2}{2 \chi_{\perp,lcfs} T} \\
\tau_E \propto& \; r_{lcfs}^2,
\end{aligned} \tag{6.1}$$

where $\langle \rho_E \rangle$ is the volume averaged thermal energy density and $q_{\perp,lcfs}$ is the perpendicular heat flux at the LCFS. To simplify the calculation, the perpendicular heat flux was considered to be $q_{\perp,lcfs} = \chi_{\perp,lcfs} \left| \nabla T \right|$ where $\chi_{\perp,lcfs}$ is a constant having the appropriate units.

6.1 Sawtooth Relaxation in Helical $\iota_{vac} = 0.0333$ Configuration

For the helically perturbed case with $\iota_{vac} = 0.0333$, boundary conditions and initial conditions were prescribed as discussed for simulations in a tokamak. The simulation used 900 finite elements for the poloidal representation with 30 in the radial direction and 30 in the θ direction, 43 Fourier numbers and a maximum time step of $\Delta t_{max} = 10^{-7}$ $s = 0.31 \tau_A$

where τ_A is the Alfvén toroidal transit time. Transport and diffusion coefficients set to obtain self-consistent equilibria having a Lundquist number $S \approx 10^5$, which is believed to be representative of the plasmas in CTH discharges. From initial conditions with $q_0 > 1$, the total plasma current is ramped from $I_{plasma,0} = 60\ kA$ to $I_{plasma} = 90\ kA$, and q_0 falls below unity after a few milliseconds.

Like the tokamak cases, a visco-resistive internal kink mode becomes unstable after q_0 is driven below unity. The growth rate has a scaling that is approximately $\gamma = \gamma_0 S^{-2/3}$ as shown in Fig. 6.2, and the eigenfunction has resistive kink behavior at the resonant surface. The magnitude of the growth rate is also larger than for the axisymmetric tokamak case, with a 20% difference in growth rate at $S = 10^5$. Finding how the growth rate of the linear mode scales with S for helically perturbed cases is made complicated by the fact that NIMROD currently cannot be run in linear mode when 3D fields are part of the equilibrium. To get around this, a time during the initial ramp up after the growth rate of the unstable mode reaches a steady value is chosen. The loop voltage $V_{loop,0}$ is recorded at this time. The simulation is then restarted with an adiabatic model for the temperature evolution and without the Ohmic heating source. This fixes the temperature, pressure and resistivity profiles. The resistivity coefficient η_0 is changed to adjust the value of S, and the loop voltage is adjusted to $V_{loop} = V_{loop,0}\eta_{0,new}/\eta_{0,old}$ so that the plasma current remains constant. The solution is advanced until the new growth rate stabilizes. When using this process to capture a growth rate for different values of S, the current density profile will resistively evolve so the q profile will not remain fixed. However, for the tokamak case where running in linear mode is possible, the correct growth rates are recovered with high accuracy.

With the addition of the helical stellarator field, modes are not characterized by a particular value of n as they are in a tokamak. It can be said that n is no longer a good quantum number [87]. The unstable internal kink mode in CTH is represented with Fourier numbers $n = 1, N_{fp} \pm 1, 2N_{fp} \pm 1, 3N_{fp} \pm 1, ...$, consistent with the $N_{fp} = 5$ field period of

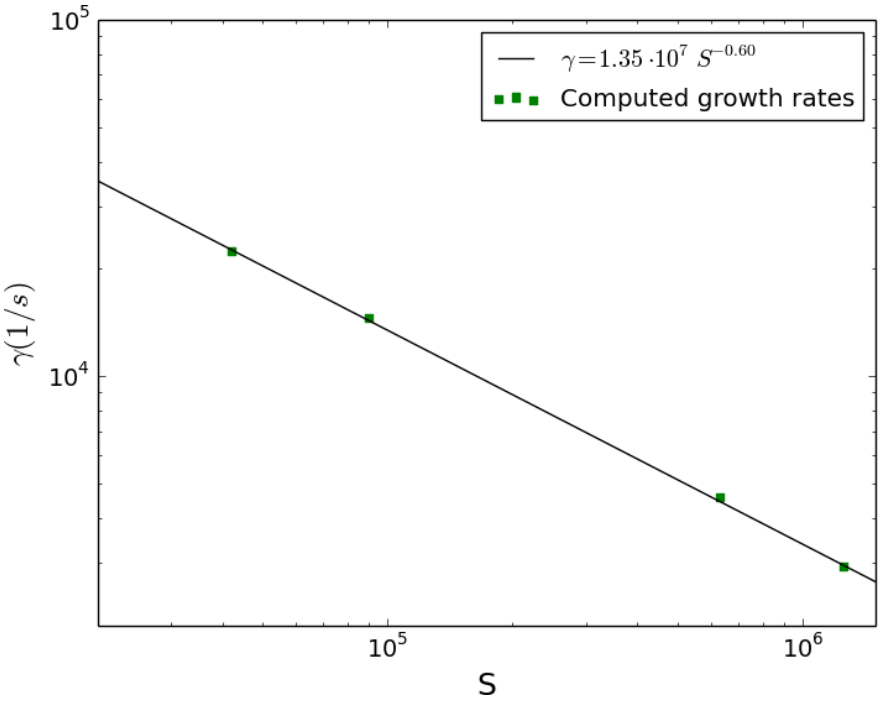

Figure 6.2: Growth rates vs. Lundquist number S for the $\epsilon_{vac} = 0.0333$ case. The equilibrium used comes from the initial ramp up, after the growth rate gets close to its maximum value for the rampup.

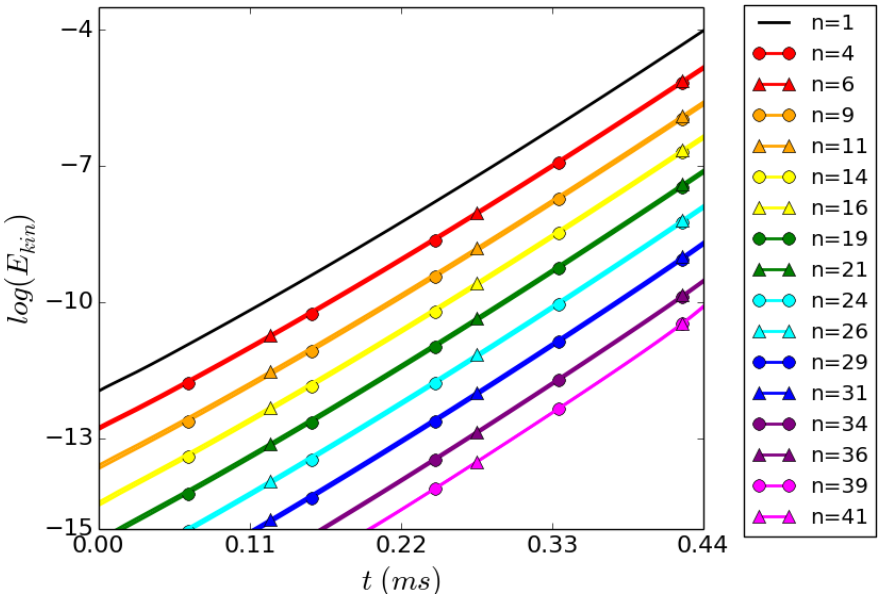

Figure 6.3: Energies of the $n = 1, N_{fp} \pm 1, 2N_{fp} \pm 1, 3N_{fp} \pm 1, ...,$ components of the magnetic field are plotted during the growth of the linear instability in the $\iota_{vac} = 0.0333$ case. The energies exponentiate at the same rate because they are all involved in representing the unstable linear mode. Unlike the axisymmetric case, instabilities in non-axisymmetric cases are not characterized by any particular value of n.

the CTH stellarator field [87]. During the linear growth phase, the energies of these Fourier numbers see exponential growth at the same rate (Fig. 6.3).

The nonlinear evolution of the relaxation for this configuration bears a striking similarity to that of the tokamak case. An island at $q = 1$ grows and the hot core undergoes a radial displacement, with a $n = 1$ toroidal variation in the direction of the displacement (Fig. 6.4). The center of the island becomes the new magnetic axis after the plasma core is completely reconnected, and the safety factor is greater than unity everywhere (Fig. 6.5). Compared to the tokamak case, the island and core are both helically deformed (Fig. 6.6).

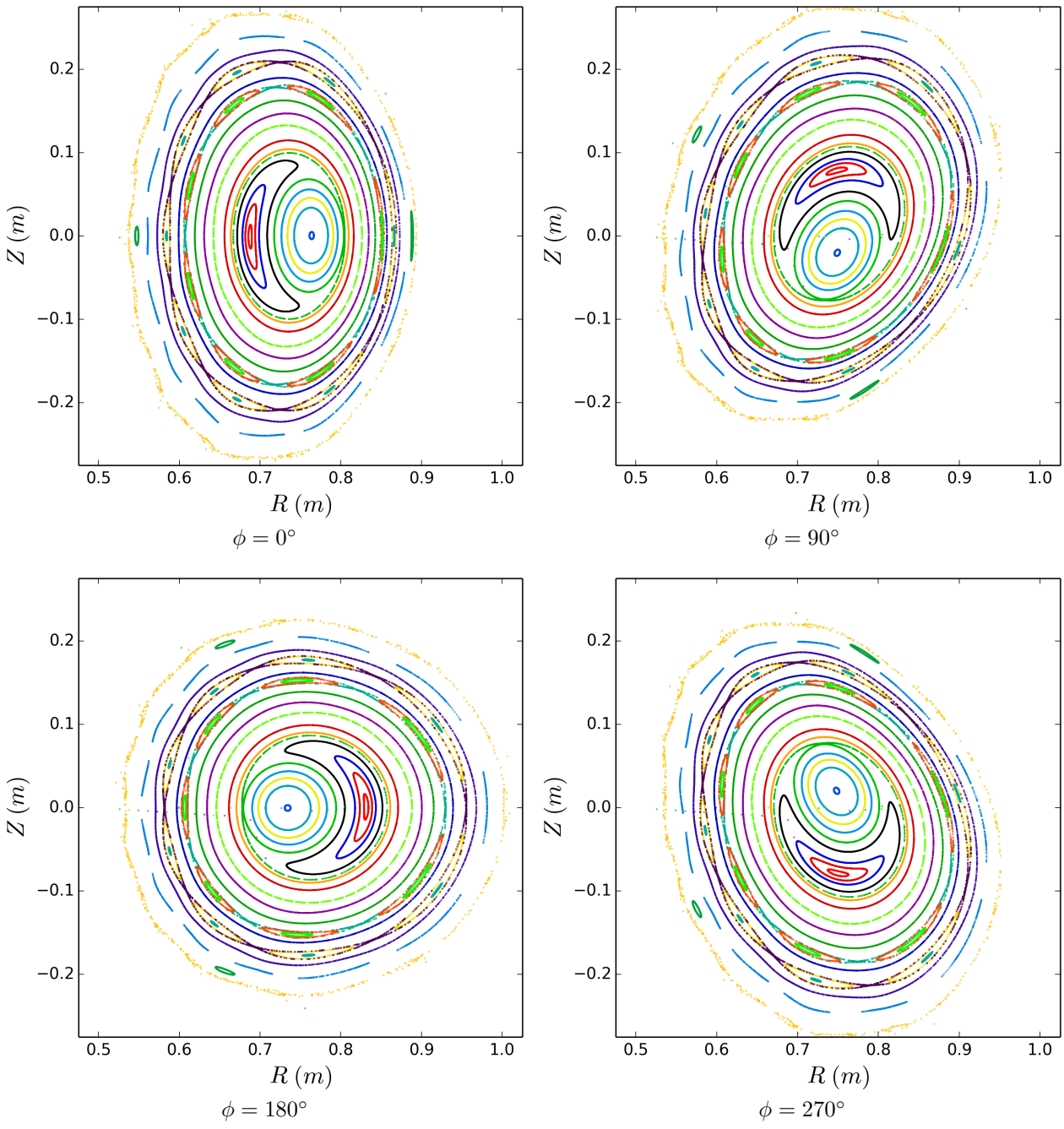

Figure 6.4: Poincaré plots at different toroidal angles during a relaxation for the $\iota = 0.033$ case. The core is undergoing a radial displacement with a $n = 1$ toroidal variation in the direction of displacement.

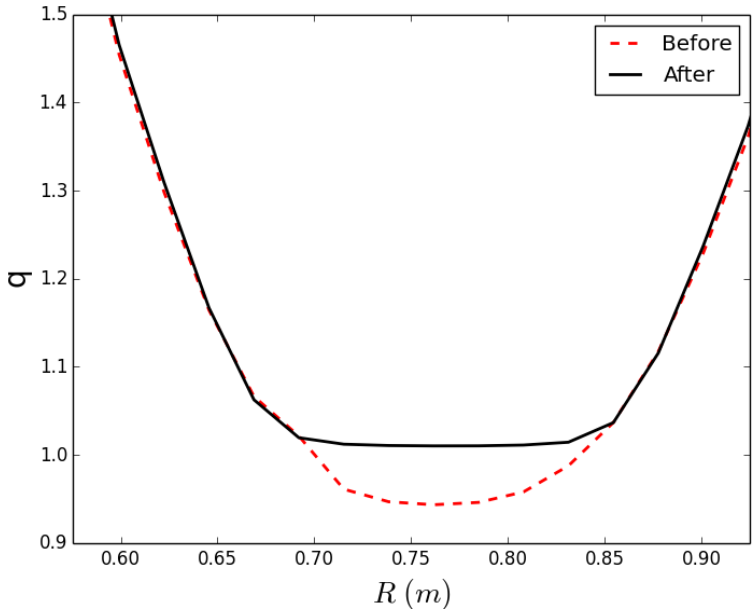

Figure 6.5: After a relaxation in the $\iota_{vac} = 0.033$ case, the q profile is flat with $q \geq 1$ everywhere.

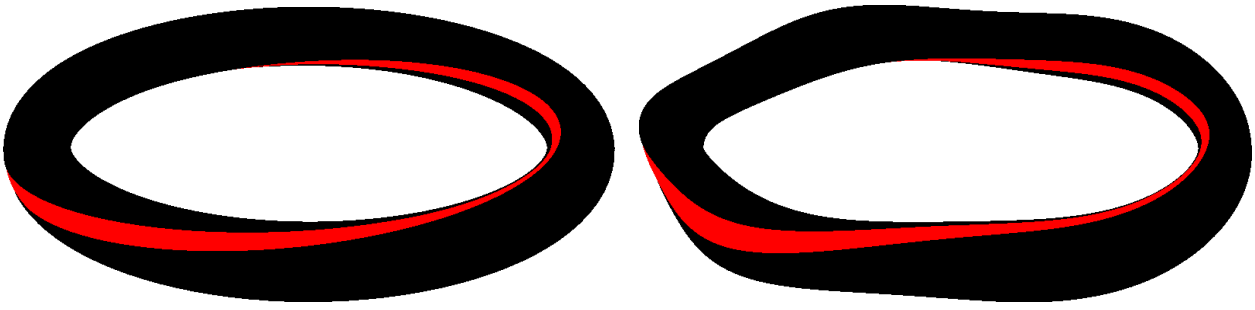

$\iota_{vac} = 0$ (tokamak) $\iota_{vac} = 0.033$

Figure 6.6: Flux tubes are plotted during a relaxation for two of the configurations. Compared to the axisymmetric case, the growing island (black) and reconnecting core (red) in the $\iota_{vac} = 0.033$ case are helically deformed.

6.2 Repeated Sawtooth Relaxations

Numerical solutions having repeated sawtooth relaxations are obtained for each configuration. The numerical parameters for these simulations and the convergence properties are discussed in the next section. Most of the values for model parameters used for the tokamak solution described earlier, tabulated in Table 5.1, were used. However, the parameters $\chi_\perp$ and I_{plasma} were varied to maintain reasonable profile shapes and roughly constant Lundquist number (Table 6.2). Total plasma current I_{plasma} is decreased as t_{vac} is increased to maintain a reasonable edge safety factor $q(a)$ that is not nearly or below unity. This is done experimentally as well. Since an approximate Spitzer resistivity is used, temperature is coupled to S. Due to the larger confinement degrading equilibrium islands and reduced minor radius seen as t_{vac} is increased, $\chi_\perp$ must be reduced as t_{vac} is increased to maintain constant S. It should also be noted that reducing I_{plasma} would result in a somewhat lower plasma temperature given a fixed τ_E.

Poincaré plots at different toroidal angles during a crash are shown for each case in Fig. 6.7. For non-axisymmetric cases, the overall picture of the relaxation process is the same as for the axisymmetric case but with a helically distorted geometry. Also, the reduced minor radius and increased equilibrium island width as t_{vac} is increased are immediately apparent in these images.

Plots of the magnetic energies of each Fourier component for each case are shown in Fig. 6.8. It is apparent from these plots that Fourier components which are multiples of the

t_{vac}	0	0.0134	0.0333	0.0970
τ_{saw} (ms)	0.52	0.48	0.37	0.28
$\chi_{\perp,0}$ (m^2/s)	17.75	15	10	10
I_{plasma} (kA)	117.5	107.5	90	88
S_0 $(\times 10^5)$	1.3	1.2	1.3	1.0
$S_{q=1}$ $(\times 10^5)$	1.3	1.2	1.3	1.0

Table 6.2: Values of $\chi_{\perp,0}$ and I_{plasma} used to obtain sawtoothing solutions for each configuration. The average value of S during the run is also tabulated.

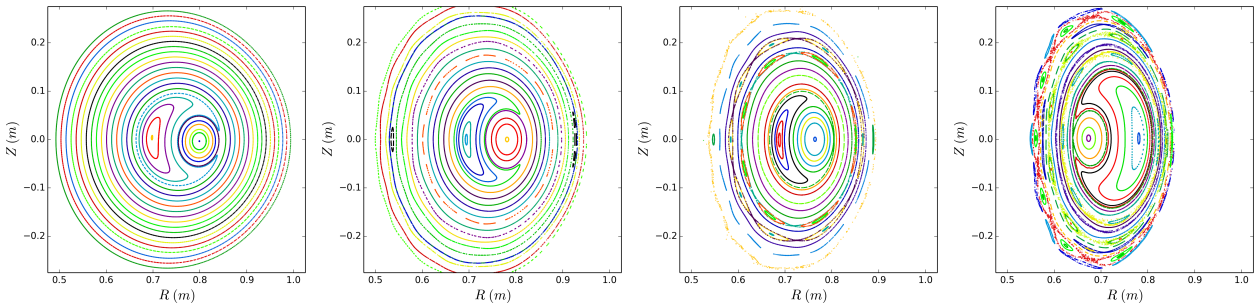

$\iota_{vac} = 0,\ \phi = 0°$ $\iota_{vac} = 0.0134,\ \phi = 0°$ $\iota_{vac} = 0.0333,\ \phi = 0°$ $\iota_{vac} = 0.0970,\ \phi = 0°$

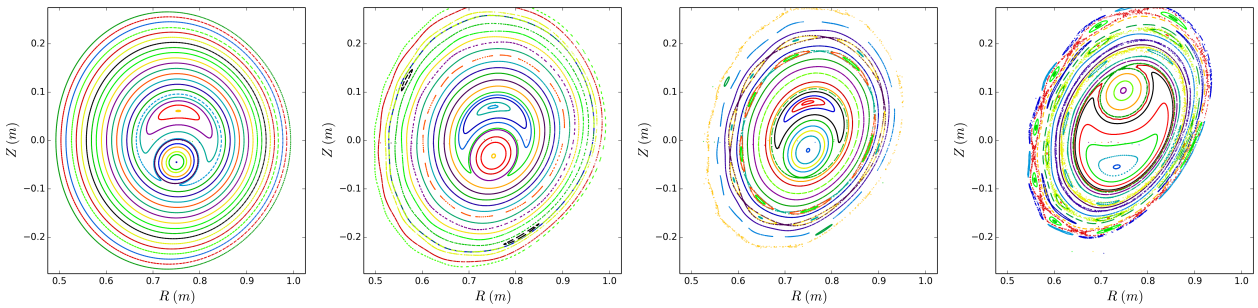

$\iota_{vac} = 0,\ \phi = 90°$ $\iota_{vac} = 0.0134,\ \phi = 90°$ $\iota_{vac} = 0.0333,\ \phi = 90°$ $\iota_{vac} = 0.0970,\ \phi = 90°$

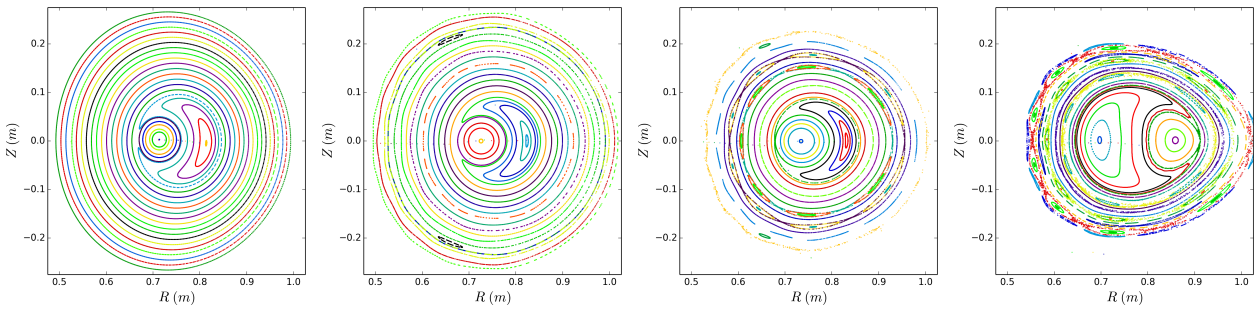

$\iota_{vac} = 0,\ \phi = 180°$ $\iota_{vac} = 0.0134,\ \phi = 180°$ $\iota_{vac} = 0.0333,\ \phi = 180°$ $\iota_{vac} = 0.0970,\ \phi = 180°$

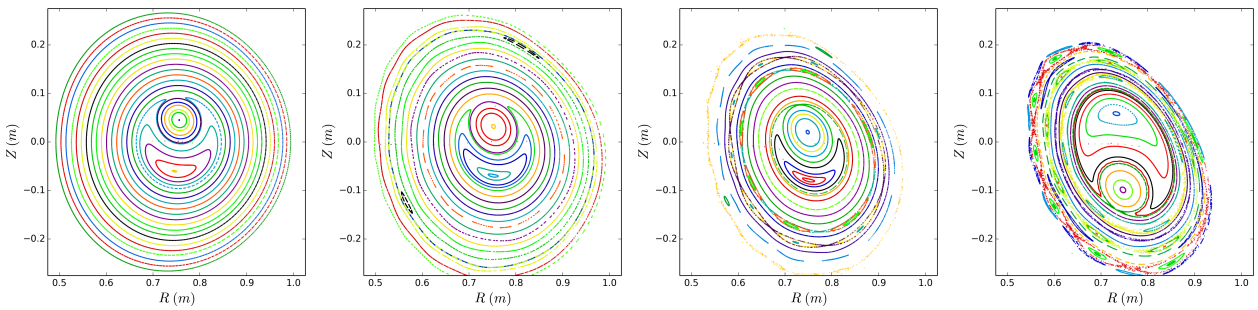

$\iota_{vac} = 0,\ \phi = 270°$ $\iota_{vac} = 0.0134,\ \phi = 270°$ $\iota_{vac} = 0.0333,\ \phi = 270°$ $\iota_{vac} = 0.0970,\ \phi = 270°$

Figure 6.7: Poincaré plots for different configurations at several toroidal angles during a relaxation. The rapidly growing island at $q = 1$ and the plasma core being driven into a resistive reconnection layer on the other side of the $q = 1$ surface can be seen. While the flux surfaces are helically distorted for non-axisymmetric configurations, the direction of displacement of the core has a $n = 1$ toroidal variation in all cases.

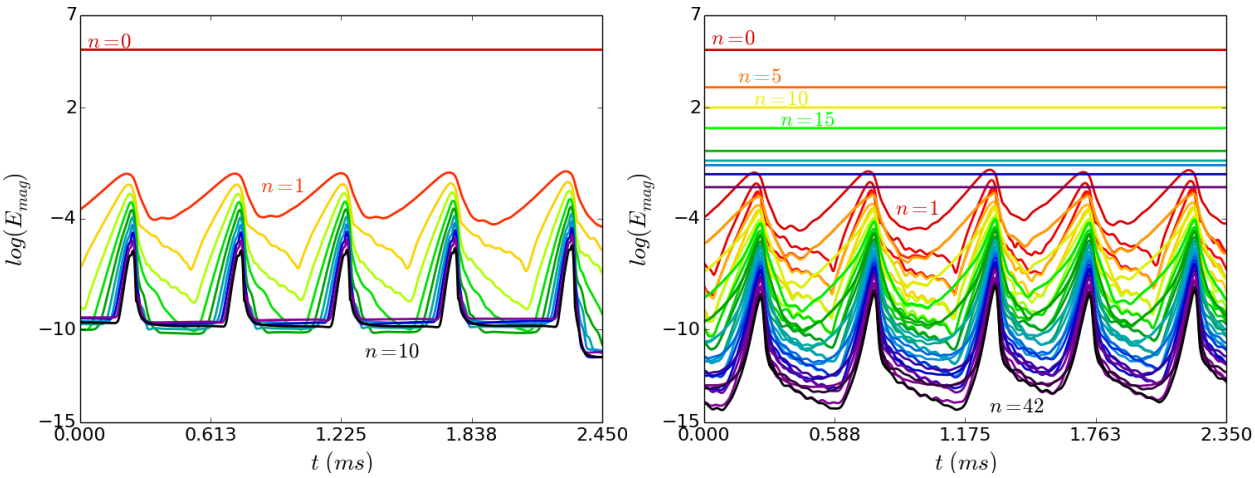

(a) $\iota_{vac} = 0$

(b) $\iota_{vac} = 0.013$

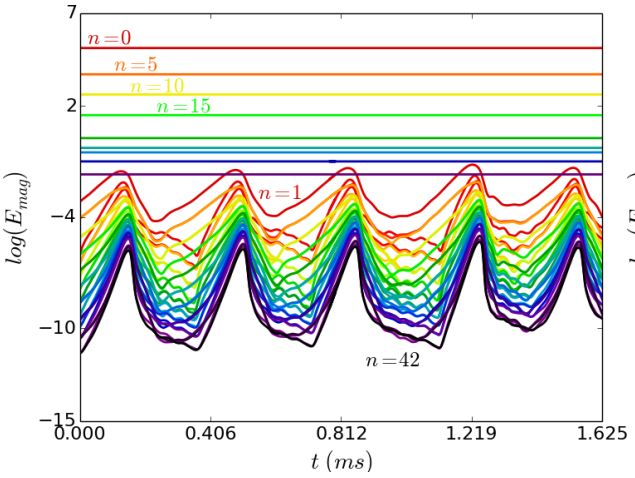

(c) $\iota_{vac} = 0.033$

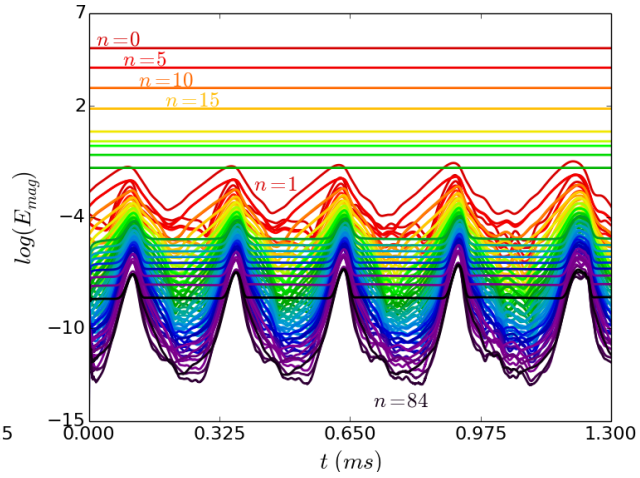

(d) $\iota_{vac} = 0.097$

Figure 6.8: Repeated relaxation oscillations are seen in the magnetic energies of the Fourier numbers in the simulations. In the tokamak case, the equilibrium is represented with $n = 0$. When the stellarator field is turned on, Fourier numbers $n = 0, 5, 10, 15, ...$ are involved in representing the equilibrium.

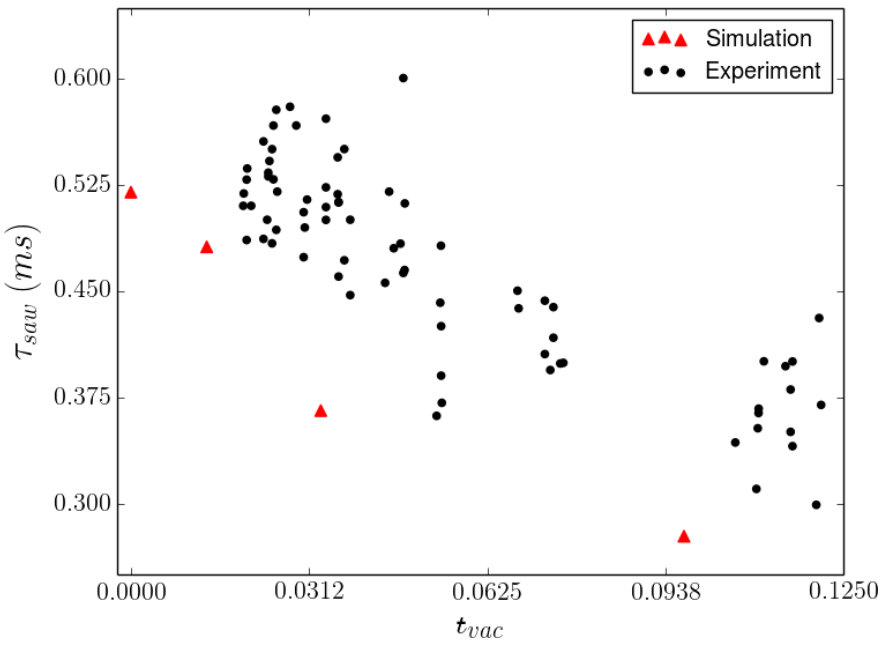

(a)

Figure 6.9: A correlation between τ_{saw} and ι_{vac} is seen in the numerical solutions and the values of τ_{saw} are quite close to what is seen experimentally. Experimental data provided by Jeffery Herfindal.

stellarator field period N_{fp} are involved in representing the equilibrium. As ι_{vac} is increased, the spacing between the magnetic energies is closer indicating that Fourier convergence is slower. A correlation between τ_{saw} and ι_{vac} from these simulations is apparent from Fig. 6.9. As ι_{vac} is increased, the sawtooth period becomes shorter which is the trend seen in the CTH experiment. Both the values of τ_{saw} and the variation of τ_{saw} with ι_{vac} are in line with what is seen experimentally, however the values of τ_{saw} from the simulation are systematically shorter than experimental values by approximately 30%. This may, in part, be due to the fact that the simulation resistivity is apparently lower than the experimental resistivity as discussed earlier.

In a resistive MHD model such as the one under consideration, several interacting phenomena are involved in a first principles consideration of τ_{saw} [56, 88]. During the ramp up phase that precedes the next relaxation, q_0 drops as the magnetic fields resistively diffuse back into the core. The diffusion of the fields is coupled to ohmic reheating in the core.

As the profile in the core evolves, the sawtooth mode becomes unstable. Given that the sawtooth mode is related to the visco-resistive kink mode, the growth rate depends on the evolving magnetic shear at the $q = 1$ surface and is proportional to $S^{-2/3}$. The nonlinear evolution of the tearing mode is to drive magnetic reconnection of the flux inside the core. Sweet-Parker reconnection proceeds at a rate proportional to $S^{-1/2}$.

When the $n = 1$ energies of each solution are plotted together, it is apparent that during the ramp phase, the $n = 1$ energy exponentiates faster for configurations with larger ι_{vac} (Fig. 6.10). This indicates that faster linear growth rates on ramp phase profiles with larger ι_{vac} account for at least part of the variation in τ_{saw} observed in the simulations. Note that the ramp phase of the numerical sawteeth is considerably longer than the non-linear relaxation phase so a modest increase γ, so that the mode exponentiates faster and is more robustly unstable, will have a larger effect on τ_{saw} than some modest change to non-linear relaxation.

To investigate the effect of helical shaping on the growth rates, approximate linear growth rates were computed for each configuration using the same method as was used for the $\iota_{vac} = 0.033$ case. The equilibrium profiles on which the growth rates were computed come from the initial rampup, after the growth rate stabilizes near the maximum value but well before the nonlinear phase is reached. Growth rates for several values of S were computed to facilitate a comparison of the growth rates between cases and to confirm that the visco-resistive kink scaling $\gamma \propto S^{-2/3}$ approximately holds for all cases. For this comparison it is better to use $S_{q=1}$ for the Lundquist number values instead of the Lundquist number at the center of the plasma S_0 because $S_{q=1}/S_0$ is different for each configuration. The result, illustrated in figure 6.11, is that γ is significantly larger for configurations with larger ι_{vac} for a given value of S. This evidence further suggests that increased linear growth rates in more strongly shaped configurations accounts for much of the correlation between τ_{saw} and S.

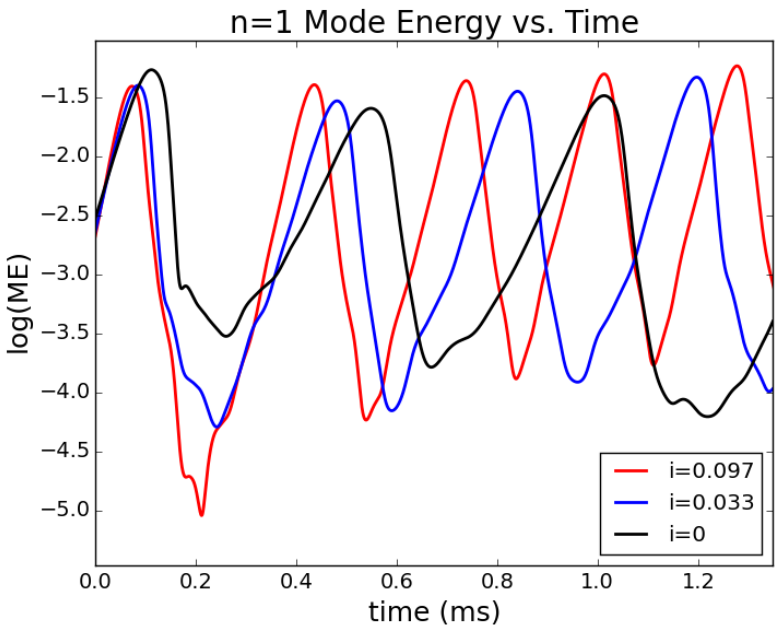

Figure 6.10: The $n = 1$ part of the magnetic energies for three configurations over several relaxations. Configurations with larger ι_{vac} have a shorter sawtooth period. It is apparent that the $n = 1$ energy of configurations with larger ι_{vac} exponentiates faster, which suggests that a faster linear growth rate at least partially accounts for the difference in τ_{saw}.

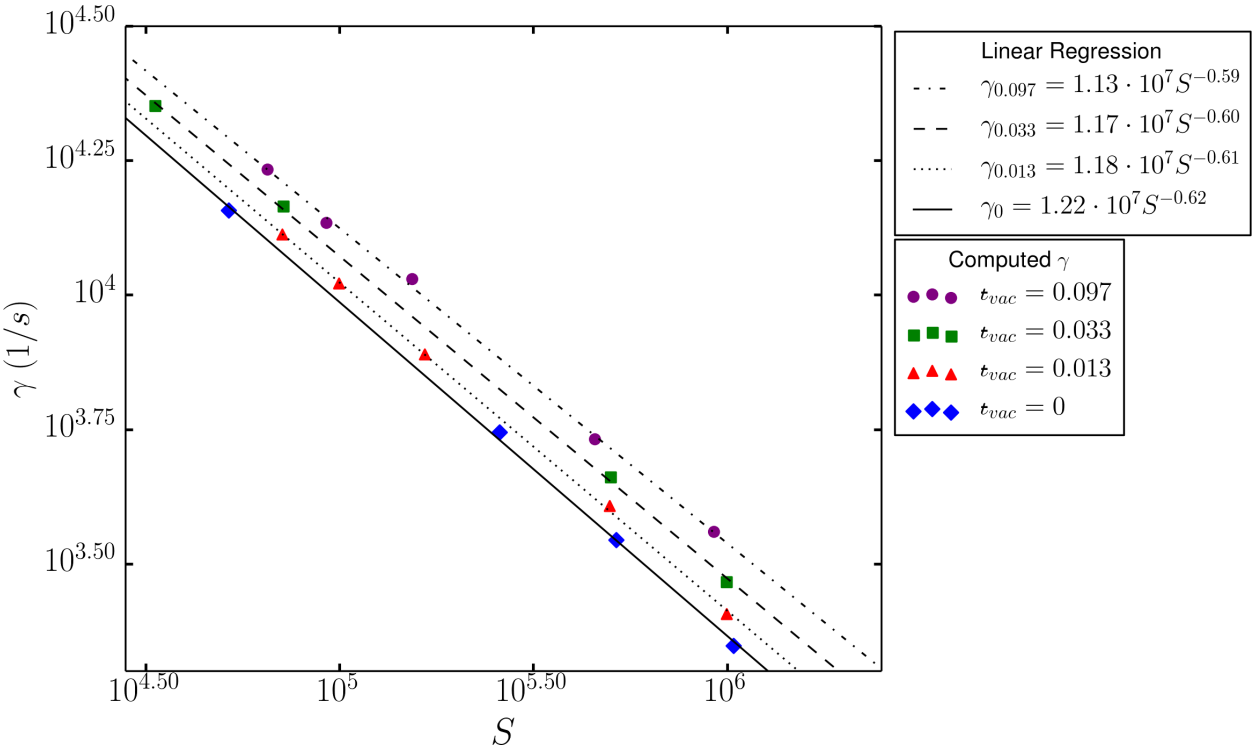

Figure 6.11: Growth rates vs. Lundquist number $S_{q=1}$ for each configuration on equilibria taken during the initial rampup after the growth rate stabilizes to near the maximum value. Configurations with a larger t_{vac} have larger γ given constant S.

Besides increased linear growth rates with stronger shaping, experimental plasmas with stronger shaping may have reduced electron temperature and therefore smaller S due to the reduced τ_E as discussed earlier. A smaller S is associated without further increased linear growth rates, faster reconnection and faster magnetic field diffusion. Data from the soft x-ray cameras does not suggest a large correlation between T_e and ι_{vac}, however a more accurate measurement of temperature from the newly installed Thompson scattering diagnostic would be needed to rule this out.

6.3 Numerical Convergence and Stability

It is convenient that, in the past, sawtooth problems in MHD have been a popular subject for convergence studies and benchmarking efforts. These past works have provided guidance in conducting the simulations. Introducing the non-axisymmetric stellarator field significantly changed the spatial, temporal and algebraic solver convergence properties of the sawtooth simulations. The poor convergence properties of cases with three-dimensional shaping was perhaps the principal obstacle to overcome in conducting the simulations and obtaining accurate numerical solutions. The experience may be valuable for future work on devices having non-axisymmetric equilibria including stellarators, RFPs in a single helicity state and perturbed tokamaks.

6.3.1 Spatial Convergence

The primary consideration in obtaining spatially converged numerical solutions of sawteeth is proper resolution of the reconnection current layer [89]. The non-axisymmetric configurations require considerably more toroidal resolution for convergence. While the axisymmetric configuration is well resolved with $n_{max} = 10$, the configuration with $\iota_{vac} = 0.0970$ requires at least $n_{max} = 85$.

For this convergence study, the toroidal resolution was scanned by restarting a converged simulation with a reduced resolution before a relaxation and advancing the solution into the

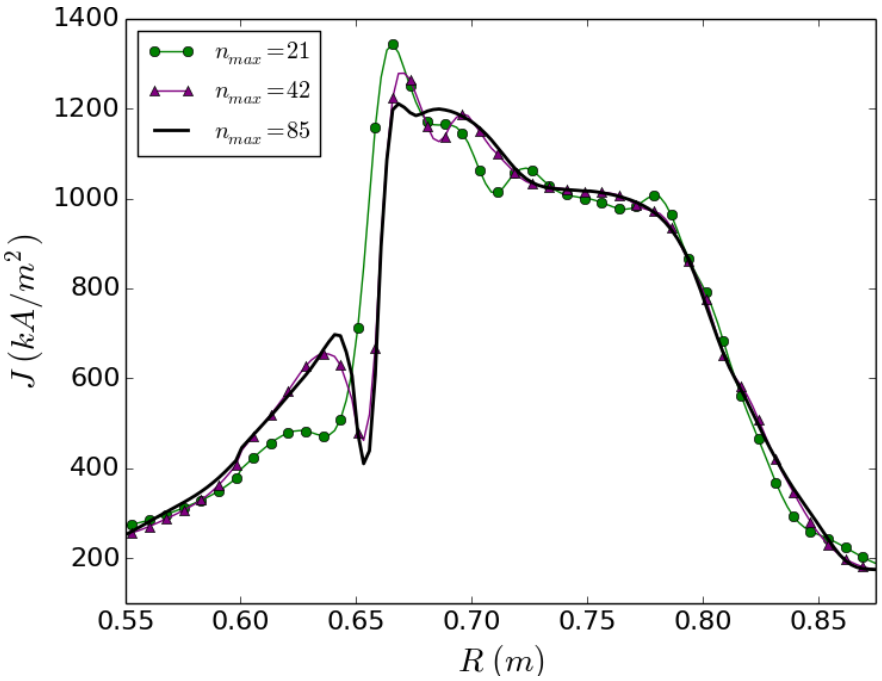

(a)

Figure 6.12: The toroidal resolution is scanned for plots of current density along $Z = 0, \phi = 0°$, which passes through the reconnection current layer for the $\iota_{vac} = 0.097$ configuration. Plots for under-resolved cases see poor resolution of the reconnection current layer with Gibbs-like oscillations.

relaxation. Plotting the current density across a chord which passes through the reconnection current layer provides a helpful visualization of the situation (Fig. 6.12). A spurious wiggling in the current density is seen when there are not enough Fourier numbers. This is likely related to the Gibbs phenomenon, as a Fourier series is involved in representing the nearly discontinuous magnetic field at the reconnection layer. In Fig. 6.13, deformed flux surfaces and spurious stochasticity are apparent in toroidally under-resolved cases.

Another consideration is having sufficient spatial resolution for accurate anisotropic heat conduction [90]. In Fig. 6.14, plots of T_e for the $\iota_{vac} = 0.0970$ case are shown. In under-resolved cases, the central temperature drops compared to the converged solution as the time is advanced. This is attributed to poorly resolved anisotropic heat conduction.

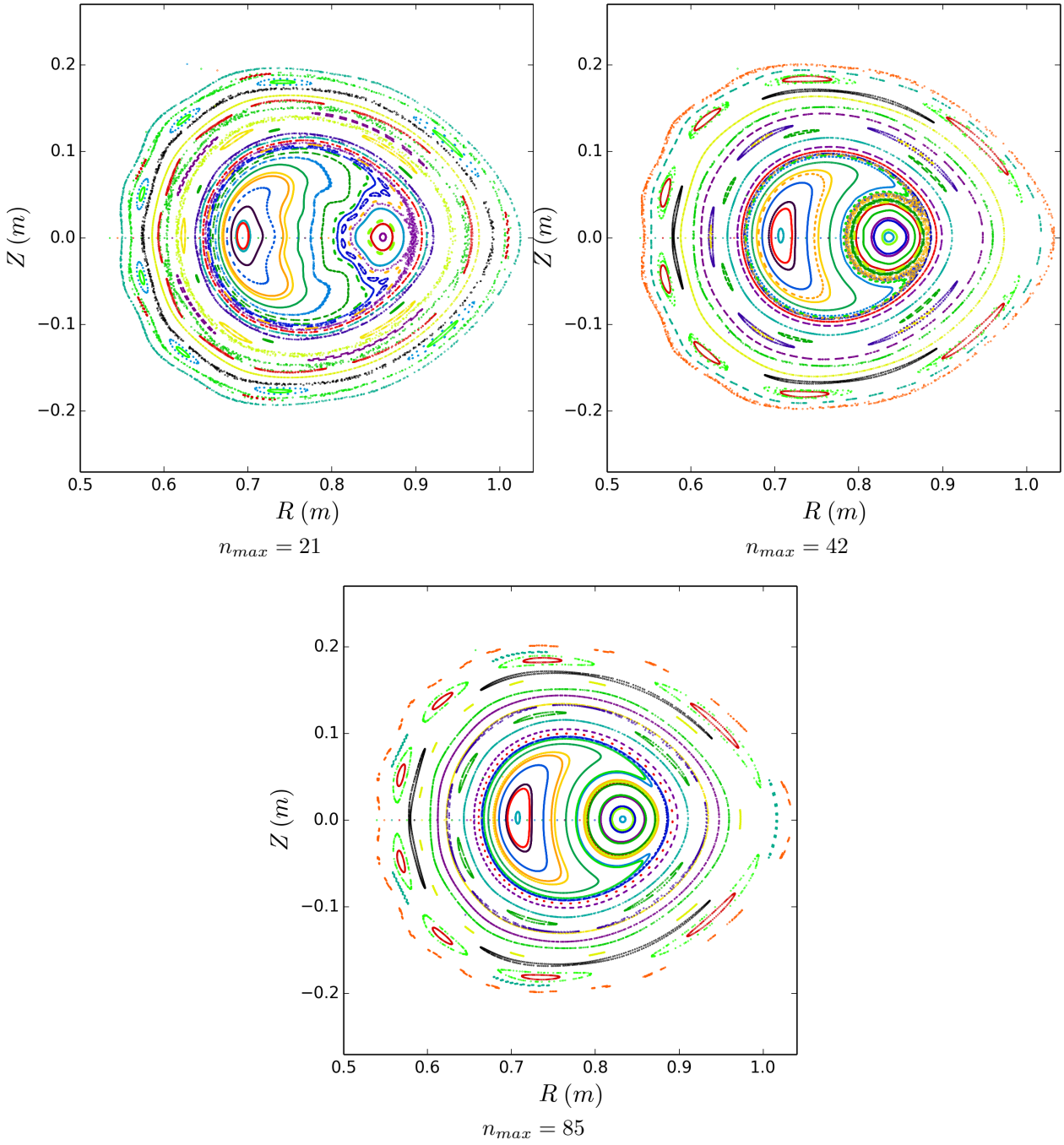

Figure 6.13: Poincaré plots are shown during a relaxation of the $\iota_{vac} = 0.097$ configuration for different toroidal resolutions. In the low resolution case $n_{max} = 21$, which is more than twice the resolution needed for convergence of the axisymmetric configuration, artificial deformation of the flux surfaces and spurious stochasticity is observed. With $n_{max} = 42$, there is spurious stochasticity near the reconnection layer.

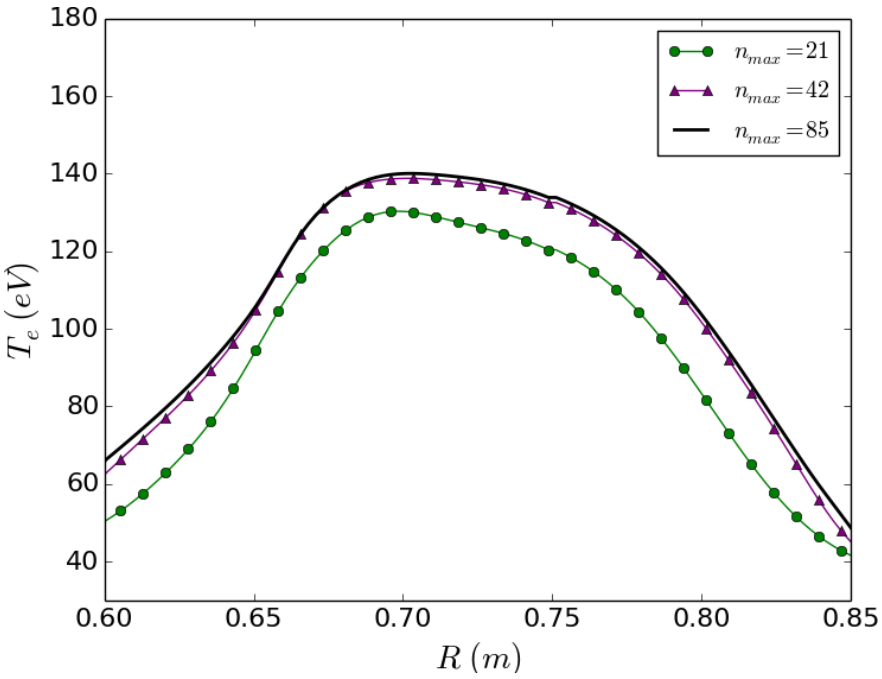

(a)

Figure 6.14: The toroidal resolution is scanned for plots of temperature along $Z = 0, \phi = 0°$ for the $\iota_{vac} = 0.097$ configuration. In the low resolution $n_{max} = 21$ plot, artificially reduced confinement is apparent due to poorly resolved anisotropic heat conduction.

6.3.2 Temporal Convergence

Special considerations are also needed for temporal convergence of non-axisymmetric configurations. Typically, NIMROD simulations use the $n = 0$ part of the solution fields in the semi-implicit operator. For the axisymmetric tokamak configuration, this approach gives numerical stability and good accuracy at large Δt in the linear phase of evolution. However for non-axisymmetric configurations a large isotropic operator is required for numerical stability if only the $n = 0$ part is used. This results in bad convergence properties, with the tearing mode having an artificially reduced growth rate unless Δt is very small compared to the characteristic Alfvén transit time $\tau_A \approx 3 \times 10^{-7}\ s$. The artificially reduced growth rate can affect whether the numerical solution reaches an oscillating steady state or a non-oscillating helical steady state. With a slower growth rate, the ramp time preceding each relaxation is longer and q_0 reaches a lower value before the relaxation. Relaxations in

temporally unconverged solutions are therefore more strongly driven than in the converged solution.

NIMROD has been modified so that the user may choose to use the full 3D solution fields in the semi-implicit operator. With the 3D semi-implicit operator, accuracy can be recovered at large Δt for non-axisymmetric configurations. When the 3D semi-implicit operator is used and significant non-axisymmetric fields are present, the velocity advance matrix is poorly conditioned. It was found that setting the isotropic semi-implicit operator coefficient, C_{nl}, to a very small value dramatically improves the conditioning of the velocity matrix without any appreciable loss in accuracy (Fig. 6.15). Improvements in computational efficiency are seen when using the 3D semi-implicit operator and a small C_{nl} over using a large isotropic Laplacian operator for stability and a small Δt for convergence.

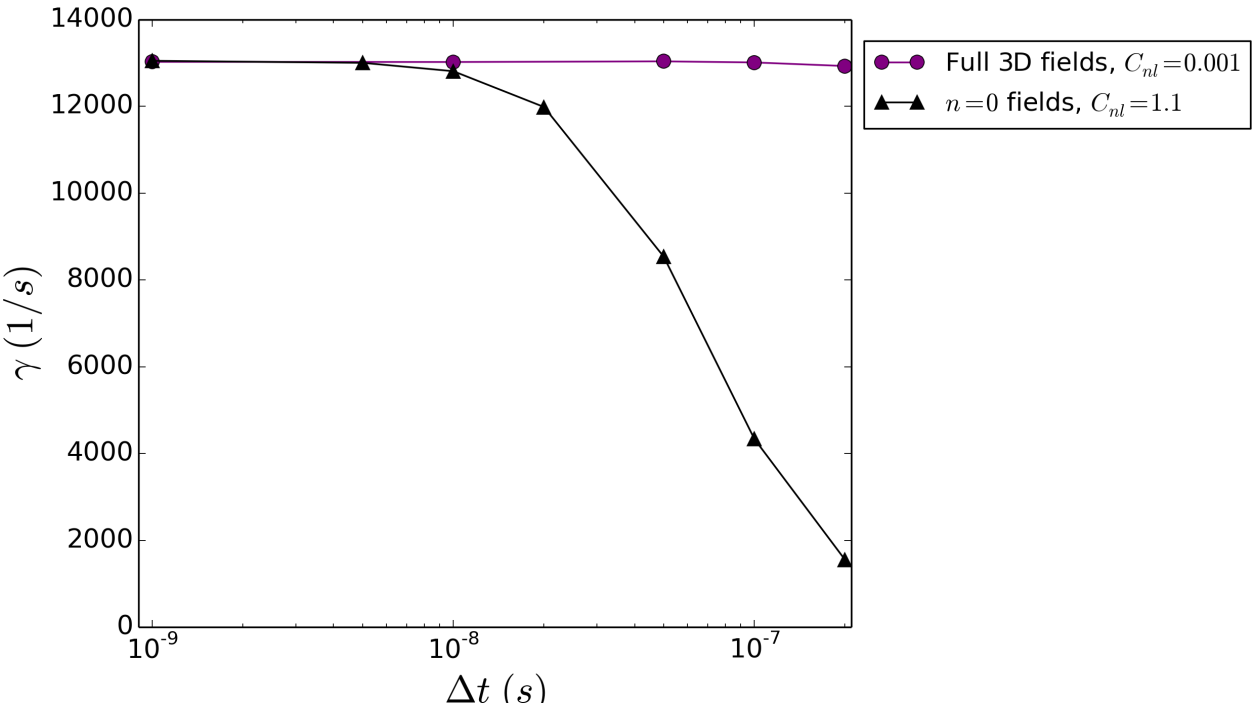

Figure 6.15: Approximate growth rates are shown for the $\iota_{vac} = 0.033$ case at some time during the initial ramp up after the tearing mode has become unstable. The size of the time step Δt is scanned for two different semi-implicit operators. When only the $n = 0$ fields are used in the semi-implicit operator, a large isotropic operator is required for numerical stability. This leads to artificially reduced growth rates at large Δt. When the full 3D fields are used, with a small isotropic term for better algebraic convergence, the temporal convergence properties are much better.

Implementation Details of 3D Semi-Implicit Operator

Here we consider the details and implementation of the semi-implicit operator term proportional to the coefficient C_{mhd} in Eq. 2.20. For convenience and clarity the term is restated here,

$$\frac{(\Delta t)^2 C_{mhd}}{\mu_0 \rho_0}\Big(\vec{B}_0 \times \nabla \times \nabla \times (\vec{B}_0 \times \Delta\vec{V})\Big). \tag{6.2}$$

A Fortran implementation of this operator term with full 3D fields is listed in appendix B. For the simulations under consideration, only this term is required for numerical stability if the full 3D fields are used in the operator.

The Galerkin method is used by NIMROD to advance the solution fields, so the contribution of this term to the weighted residual $\vec{R_{i,n}}$ must be computed,

$$\vec{R}_{i,n} = \iiint \vec{f}^*_{i,n} \cdot \vec{B}_0 \times \nabla \times \nabla \times \left(\vec{B}_0 \times \Delta\vec{V}\right)\, dV, \tag{6.3}$$

where $\vec{f}^*_{i,n}$ are the test functions, i is an index that runs over finite element basis functions and n indexes Fourier components. It is necessary to integrate by parts to reduce the maximum order of derivative in the equations. Because the continuity of the finite elements is only C^0, the weak form cannot have derivatives higher than first order. Integration by parts also allows the use of natural boundary conditions which simplifies implementation [65]. The integration by parts is accomplished by applying the following identity

$$\vec{a} \cdot (\vec{b} \times (\nabla \times \vec{c})) = \nabla \times \vec{c} \cdot (\vec{a} \times \vec{b}) \tag{6.4}$$

and divergence theorem corollary,

$$\iiint \left[\vec{b} \cdot (\nabla \times \vec{a}) - \vec{a} \cdot (\nabla \times \vec{b})\right]\, dV = \oint (\vec{a} \times \vec{b}) \cdot \hat{n}\, dS. \tag{6.5}$$

The result of this integration by parts has only first derivatives, and because a no-slip boundary condition for the velocity is used, the surface integral is taken to be zero

$$\vec{R}_{i,n} = \iiint \left[\nabla\times(\vec{f}^{*}_{i,n}\times\vec{B})\cdot\nabla\times(\Delta\vec{V}\times\vec{B})\right] dV - \cancelto{0}{\oint (\vec{f}^{*}_{i,n}\times\vec{B})\times\nabla\times(\Delta\vec{V}\times\vec{B})\cdot\hat{n}\, dS}. \quad (6.6)$$

Define $\vec{r}_{i,n}$ to be the Fourier transformed weighted residual integrand,

$$\begin{aligned}\vec{R}_{i,n} &= \iiint \left[\nabla\times(e^{-in\phi}(\hat{f}^{p}_{i}\hat{e}_R + \hat{f}^{p}_{i}\hat{e}_Z + \hat{f}^{p}_{i}\hat{e}_\phi)\times\vec{B})\cdot\nabla\times(\Delta\vec{V}\times\vec{B})\right] R\, dRdZd\phi \\ \vec{R}_{i,n} &\equiv \iint \vec{r}_{i,n} R\, dRdZ.\end{aligned} \quad (6.7)$$

Implementation involves, at a minimum, adding code to compute $\vec{r}_{i,n}$ and adding these quantities to the total weighted residuals. The semi-implicit operator term Eq. 6.2 is an implicit term because it contains the solution fields at the advanced time. Therefore, $\vec{r}_{i,n}$ should be computed in the appropriate velocity "dot" routine, where the value of $\Delta\vec{V}$ is updated every GMRES step. When only the axisymmetric solution fields are used, so that $\vec{B} = \vec{B}_0$, this is straightforward because of Fourier orthogonality. We go through the steps to implement the term with only axisymmetric fields as an example before considering implementation of the 3D operator. First the following two quantities,

$$\begin{aligned}(dbe)_n &= \nabla\times(\Delta\vec{V}_n\times\vec{B}_0) \\ (crl)_{i,n} &= \nabla\times(\vec{f}^{*}_{i,n}\times\vec{B}_0),\end{aligned} \quad (6.8)$$

are computed, where $\Delta\vec{V}_n$ is the n^{th} Fourier component of $\Delta\vec{V}$. The dot product of these quantities is computed and the values are added to the integrand array. The NIMROD framework provides tools to easily compute poloidal derivatives of $\Delta\vec{V}_n$, $\vec{f}^{*}_{i,n}$ and $\vec{B}_0$, but not the poloidal derivatives of products of these quantities. Therefore, the following vector

calculus identity is used to compute $(dbe)_n$ and $(crl)_{i,n}$,

$$\nabla \times (\vec{c} \times \vec{B}) = (\vec{B} \cdot \nabla)\vec{c} - (\vec{c} \cdot \nabla)\vec{B} - \vec{B}(\nabla \cdot \vec{c}), \tag{6.9}$$

where the equation $\nabla \cdot \vec{B} = 0$ was invoked.

Implementation with the 3D solution fields is somewhat more challenging. The solution field $\vec{B}$ and its derivatives are inverse transformed to configuration space before the integrand routine is called for the first time and is stored in an array. The change in the solution field over the current time step, $\Delta\vec{V}$, and its derivatives are inverse transformed in the integrand routine because this quantity changes every GMRES step.

The factors $\vec{a}^l$, $\vec{b}^l_j$ of the test function and its derivatives are then computed and Fourier transformed. Consider the contribution from the l^{th}-component of the test function vector,

$$\begin{aligned}\Big[\nabla \times (f_i^p \hat{e}_l e^{-in\phi} \times \vec{B}) \cdot \nabla \times (\Delta\vec{V} \times \vec{B})\Big]_j = \\ = \Big[a_1^l \hat{f}_i^p + b_{j,1}^l \frac{\partial \hat{f}_i^p}{\partial R} + b_{j,2}^l \frac{\partial \hat{f}_i^p}{\partial Z} + b_{j,3}^l (-in\hat{f}_i^p)\Big] e^{-in\phi}.\end{aligned} \tag{6.10}$$

We then have the quantities $\vec{r}_{i,n}$ by multiplying the transformed factors by the test function or appropriate derivative,

$$\vec{r}_{i,n} = \hat{f}_i^p \sum_l \int \vec{a}^l e^{-in\phi}\, d\phi + \widetilde{\nabla} f_i \cdot \sum_{l,j} \int \vec{b}_j^l e^{-in\phi}\, d\phi, \tag{6.11}$$

where

$$\widetilde{\nabla} f_i \equiv \Big(\frac{\partial \hat{f}_i^p}{\partial R}, \frac{\partial \hat{f}_i^p}{\partial Z}, -in\hat{f}_i^p\Big). \tag{6.12}$$

The values of all factors $\vec{a}^l$, $\vec{b}^l_j$ are in the fortran implementation. The first step to finding the values of these factors is to factor the test function from $\nabla \times (\vec{f}^*_{i,n} \times \vec{B})$, and as

an example the result is shown below for only the R component test function,

$$\begin{aligned}
\nabla \times (\hat{f}_i^p e^{-in\phi}\hat{e}_R \times \vec{B})_R &= \frac{\partial(\hat{f}_i^p e^{-in\phi})}{\partial\phi} B_\phi + \Big(\frac{\partial \hat{f}_i^p}{\partial Z} B_Z - \hat{f}_i^p(\frac{\partial B_R}{\partial R} + \frac{B_R}{R})\Big) e^{-in\phi} \\
\nabla \times (\hat{f}_i^p e^{-in\phi}\hat{e}_R \times \vec{B})_\phi &= \Big(- \hat{f}_i^p \frac{\partial B_\phi}{\partial R} - \frac{\partial \hat{f}_i^p}{\partial R} B_\phi\Big) e^{-in\phi} \\
\nabla \times (\hat{f}_i^p e^{-in\phi}\hat{e}_R \times \vec{B})_Z &= \Big(- \hat{f}_i^p(\frac{\partial B_Z}{\partial R} + \frac{B_Z}{R}) - \frac{\partial \hat{f}_i^p}{\partial R} B_Z\Big) e^{-in\phi}.
\end{aligned} \tag{6.13}$$

The contributions of the Z and ϕ components of the test function also have seven terms each.

6.3.3 Algebraic Convergence

Non-axisymmetric configurations can have significantly slower GMRES convergence compared to axisymmetric configurations. As mentioned earlier, when the 3D semi-implicit operator is used, the velocity advance matrix becomes more poorly conditioned as stellarator field strength is increased. A very small isotropic term in the semi-implicit operator dramatically improves the conditioning of the velocity matrix without any appreciable loss in accuracy. It should also be noted that when strongly anisotropic thermal diffusion is used, the temperature advance matrix is poorly conditioned for non-axisymmetric cases. Configurations with increasing stellarator field strength see increasingly worse matrix conditioning. This makes non-axisymmetric problems less computationally efficient.

Chapter 7

Conclusions

In this work, numerical solutions of repeated sawteeth were obtained for a family of configurations with increasing CTH helical field strength. Although the sawtooth periods τ_{saw} seen in the numerical solutions are systematically shorter than experimental values by approximately 30%, the trend in τ_{saw} vs. ι_{vac} was recovered remarkably well. It was found that the CTH helical field enhances the linear growth rate of the visco-resistive kink mode that drives the sawtooth relaxation, and that this is a first principle reason behind the correlation between τ_{saw} and ι_{vac}. Another effect of the helical field on the linear mode was to make n no longer a mode number, as expected. In the axisymmetric case, an n = 1 resistive internal kink mode drives the relaxation. However in non-axisymmetric cases, the unstable mode is represented by toroidal Fourier numbers $n = 1, N_{fp} \pm 1, 2N_{fp} \pm 1, 3N_{fp} \pm 1, ...$ The process of non-linear relaxation does not change from fundamentally from the Kadomtsev description as ι_{vac} is increased. The plasma core is radially displaced and reconnected as an island grows to eventually replace the core. The relaxations in non-axisymmetric cases differ from relaxations of the axisymmetric case in the helical deformation of the growing island and reconnecting core. Because the correlation between τ_{saw} and ι_{vac} is apparently largely due to enhanced linear growth rates, future work on the effect of the CTH helical field on sawteeth might involve doing actual linear calcluations to find the eigenmodes and growth rates on profiles that resemble experimental ramp phase profiles. Values for growth rate γ were computed in this work by nonlinear calculations, before the mode nonlinearly saturates, on the profiles before the first sawtooth relaxation. It also may be fruitful to conduct simulations of repeated sawteeth using more sophisticated model equations and closures.

The numerical convergence properties of cases having non-axisymmetric stellarator fields are different from the axisymmetric case. The standard NIMROD semi-implicit operator, which uses only the axisymmetric solution fields, has bad temporal convergence properties for non-axisymmetric cases. Given a large time step size (approaching the size of the characteristic Alfvén transit time), the resistive internal kink mode will have an artificially reduced growth rate. The standard NIMROD semi-implicit operator was modified to include the full solution fields and this allowed for improved temporal convergence properties of non-axisymmetric cases. Temporally unconverged solutions may appear to be stable or only weakly unstable due to artificially reduced growth rates. The nonlinear evolution of an unconverged solution may be qualitatively different from the converged solution. Spatial convergence was also more challenging for non-axisymmetric cases. Finer spatial resolution, especially in the toroidal direction is needed to resolve the reconnection current layer during nonlinear evolution. Numerical solutions with insufficient toroidal spatial resolution will have a Gibbs-like oscillation in the current density near the reconnection layer leading to spurious stochasticity.

Besides the numerical solutions of sawteeth, a novel variation on the Fourier-Bessel method was introduced. In this variation, the argument of the Bessel function is not the distance from the axis of the torus r, but the normalized toroidal flux s from a VMEC equilibrium. This allows known information about the magnetic fields to be used in the interpretation of the soft x-ray signals. The result is that, compared to the standard Fourier-Bessel method, the modified method gives much better accuracy for benchmark cases with realistic data in a average error sense. However, the modified method gives reconstructions that are overly broadened in the center so that it is not clear which method is better for studying sawteeth which are localized in the center. From preliminary testing, it appears that using $\sqrt{s}$ instead of s for the radial coordinate may eliminate this tendency for reconstructions to be overly broadened in the center.

Bibliography

[1] J. P. Freidberg. *Plasma physics and fusion energy*. Cambridge University Press, 2008.

[2] F. C. Díaz. An overview of the VASIMR engine: High power space propulsion with RF plasma generation and heating. In *Radio Frequency Power in Plasmas: 14th Topical Conference*, volume 595, pages 3–15. AIP Publishing, 2001.

[3] J. D. Lawson. Some criteria for a power producing thermonuclear reactor. *Proceedings of the Physical Society. Section B*, 70(1):6, 1957.

[4] JET Team et al. Fusion energy production from a deuterium-tritium plasma in the JET tokamak. *Nuclear Fusion*, 32(2):187, 1992.

[5] J. D. Strachan, H. Adler, P. Alling, C. Ancher, H. Anderson, J. L. Anderson, D. Ashcroft, C. W. Barnes, G. Barnes, S. Batha, et al. Fusion power production from TFTR plasmas fueled with deuterium and tritium. *Physical Review Letters*, 72(22):3526, 1994.

[6] K. Ikeda et al. Progress in the ITER physics basis. *Nuclear Fusion*, 47(6):S1, 2007.

[7] P. Helander, C. D. Beidler, T. M. Bird, M. Drevlak, Y. Feng, R. Hatzky, F. Jenko, R. Kleiber, JHE Proll, Y. Turkin, et al. Stellarator and tokamak plasmas: a comparison. *Plasma Physics and Controlled Fusion*, 54(12):124009, 2012.

[8] S. Von Goeler, W. Stodiek, and N. Sauthoff. Studies of internal disruptions and m= 1 oscillations in tokamak discharges with soft—x-ray techniques. *Physical Review Letters*, 33(20):1201, 1974.

[9] F. Orain, M. Bécoulet, J. Morales, G. T. A. Huijsmans, G. Dif-Pradalier, M. Hoelzl, X. Garbet, S. Pamela, E. Nardon, C. Passeron, et al. Non-linear MHD modeling of edge localized mode cycles and mitigation by resonant magnetic perturbations. *Plasma Physics and Controlled Fusion*, 57(1):014020, 2015.

[10] H. Reimerdes, A. Pochelon, O. Sauter, T. P. Goodman, H. A. Henderson, and An. Martynov. Effect of triangularity and elongated plasma shape on the sawtooth stability. *Plasma Physics and Controlled Fusion*, 42:629–639, 2000.

[11] E. A. Lazarus, F. L. Waelbroeck, et al. A comparison of sawtooth oscillations in bean and oval shaped plasmas. *Plasma Physics and Controlled Fusion*, 48:L65–L72, 2006.

[12] J. Luxon et al. Recent results from the DIII-D tokamak and implications for future devices. *Fusion Engineering and Design*, 30(1):39–52, 1995.

[13] S. Coda. Progress and scientific results in the TCV tokamak. *Nuclear Fusion*, 51:094017, 2011.

[14] T. E. Evans, M. E. Fenstermacher, R. A. Moyer, T. H. Osborne, J. G. Watkins, P. Gohil, I. Joseph, M. J. Schaffer, L. R. Baylor, M. Becoulet, et al. RMP ELM suppression in DIII-D plasmas with ITER similar shapes and collisionalities. *Nuclear fusion*, 48(2):024002, 2008.

[15] A. H. Boozer. Use of nonaxisymmetric shaping in magnetic fusion. *Physics of Plasmas*, 16(5):058102, 2009.

[16] M. C. Zarnstorff, L. A. Berry, A. Brooks, E. Fredrickson, G. Y. Fu, S. Hirshman, S. Hudson, L. P. Ku, E. Lazarus, D. Mikkelsen, et al. Physics of the compact advanced stellarator NCSX. *Plasma Physics and Controlled Fusion*, 43(12A):A237, 2001.

[17] J. T. Peterson, G. J. Hartwell, S. F. Knowlton, J. Hanson, R. F. Kelly, and C. Montgomery. Initial vacuum magnetic field mapping in the Compact Toroidal Hybrid. *Journal of Fusion Energy*, 26(1-2):145–148, 2007.

[18] J. D. Hanson, S. F. Knowlton, B. A. Stevenson, and G. J. Hartwell. Equilibrium and stability of current-carrying discharges in the non-axisymmetric CTH experiment. *Contributions to Plasma Physics*, 50(8):724–730, 2010.

[19] M. D. Pandya, M. C. ArchMiller, M. R. Cianciosa, D. A. Ennis, J. D. Hanson, G. J. Hartwell, J. D. Hebert, J. L. Herfindal, S. F. Knowlton, X. Ma, et al. Low edge safety factor operation and passive disruption avoidance in current carrying plasmas by the addition of stellarator rotational transform. *Physics of Plasmas*, 22(11):110702, 2015.

[20] M. C. ArchMiller, M. R. Cianciosa, D. A. Ennis, J. D. Hanson, G. J. Hartwell, J. D. Hebert, J. L. Herfindal, S. F. Knowlton, X. Ma, D. A. Maurer, et al. Suppression of vertical instability in elongated current-carrying plasmas by applying stellarator rotational transform. *Physics of Plasmas*, 21(5):056113, 2014.

[21] G. A. Müller, V. Erckmann, H. J. Hartfuβ, H. Laqua, H. Maassberg, U. Stroth Weller A. Rome, M. and, W VII-AS Team, and ECRH group. Shear modification by ECCD and related confinement phenomena in W7-AS. *AIP Conference Proceedings*, 355:133, 1996.

[22] M. Wakatani and S. Sudo. Overview of Heliotron E results. *Plasma Physics and Controlled Fusion*, 38(7):937, 1996.

[23] S. E. Grebenshchikov, B. I. Kornev, and I. S. Shpigel'. Soft x-ray sawtooth oscillations in the L-2 stellarator. *Soviet Journal of Plasma Physics*, 8(3):256–260, 1982.

[24] C. R. Sovenic, A. H. Glasser, T. A. Gianakon, D. C. Barnes, R. A. Nebel, S. E. Kruger, D. D. Schnack, S. J. Plimpton, A. Tarditi, M. S. Chu, and the NIMROD Team. Nonlinear magnetohydrodynamics simulation using high-order finite elements. *Journal of Computational Physics*, 195:355–386, 2004.

[25] P. M. Bellan. *Fundamentals of plasma physics*. Cambridge University Press, 2008.

[26] T. S. Hahm. Nonlinear gyrokinetic equations for tokamak microturbulence. *Physics of Fluids*, 31(9):2670–2673, 1988.

[27] S. E. Kruger, D. D. Schnack, and C. R. Sovinec. Dynamics of the major disruption of a DIII-D plasma. *Physics of Plasmas*, 12(5):056113, 2005.

[28] J. P. Freidberg. Ideal magnetohydrodynamic theory of magnetic fusion systems. *Reviews of Modern Physics*, 54(3):801, 1982.

[29] W. Park, E. V. Belova, G. Y. Fu, X. Z. Tang, H. R. Strauss, and L. E. Sugiyama. Plasma simulation studies using multilevel physics models. *Physics of Plasmas*, 6(5):1796–1803, 1999.

[30] L. L. Lao, H. St John, R. D. Stambaugh, A. G. Kellman, and W. Pfeiffer. Reconstruction of current profile parameters and plasma shapes in tokamaks. *Nuclear Fusion*, 25(11):1611, 1985.

[31] J. D. Hanson, S. P. Hirshman, S. F. Knowlton, L. L. Lao, E. A. Lazarus, and J. M. Shields. V3FIT: a code for three-dimensional equilibrium reconstruction. *Nuclear Fusion*, 49(7):075031, 2009.

[32] S. P. Hirshman and J. C. Whitson. Steepest-descent moment method for three-dimensional magnetohydrodynamic equilibria. *Physics of Fluids*, 26:3553–3568, 1983.

[33] V. S. Lukin. *Computational Study of the Internal Kink Mode Evolution and Associated Magnetic Reconnection Phenomena*. PhD thesis, Princeton University, 2008.

[34] J. Peter Goedbloed and S. Poedts. *Principles of magnetohydrodynamics: with applications to laboratory and astrophysical plasmas*. Cambridge University Press, 2004.

[35] J. Wesson and D. J. Campbell. *Tokamaks*, volume 149. Oxford University Press, 2011.

[36] B. Coppi, R. Galvao, R. Pellat, M. Rosenbluth, and P. Rutherford. Resistive internal kink modes. *Soviet Journal of Plasma Physics*, 2(6):533–535, 1976.

[37] R. J. Hastie, T. C. Hender, B. A. Carreras, L. A. Charlton, and J. A. Holmes. Stability of ideal and resistive internal kink modes in toroidal geometry. *Physics of Fluids*, 30(6):1756–1766, 1987.

[38] L. Zheng. *Advanced Tokamak Stability Theory*. Morgan & Claypool Publishers, 2014.

[39] B. Carreras, H. R. Hicks, J. A. Holmes, and B. V. Waddell. Nonlinear coupling of tearing modes with self-consistent resistivity evolution in tokamaks. *Physics of Fluids*, 23(9):1811–1826, 1980.

[40] J. A. Wesson. Hydromagnetic stability of tokamaks. *Nuclear Fusion*, 18(1):87, 1978.

[41] H. Baty, J.-F. Luciani, and M.-N. Bussac. Transition from a resistive kink mode to Kadomtsev reconnection. *Nuclear Fusion*, 31:2055–2062, 1991.

[42] P. A Sweet. The neutral point theory of solar flares. In *Symposium-International Astronomical Union*, volume 6, pages 123–134. Cambridge Univ Press, 1958.

[43] B. B. Kadomtsev. Disruptive instability in tokamaks. *Soviet Journal of Plasma Physics*, 1:389–391, 1975.

[44] J. A. Wesson. Sawtooth oscillations. *Plasma Physics and Controlled Fusion*, 28:243–248, 1986.

[45] M. Tian-Peng, H. Li-Qun, W. Bao-Nian, R. Huai-Lin, G. Xiang, Z. Xiang-Jun, Z. Li-Wu, S. You-Wen, C. Zhong-Yong, L. Shi-Yao, et al. Study of sawtooth oscillations on the HT-7 tokamak using 2D tomography of soft x-ray signal. *Chinese Physics*, 14(10):2061, 2005.

[46] A. Y. Aydemir. Nonlinear studies of m= 1 modes in high-temperature plasmas. *Physics of Fluids B: Plasma Physics*, 4(11):3469–3472, 1992.

[47] F. D. Halpern, Hinrich Lütjens, and J-F Luciani. Diamagnetic thresholds for sawtooth cycling in tokamak plasmas. *Physics of Plasmas*, 18(10):102501, 2011.

[48] D. J. Campbell, DFH Start, J. A. Wesson, D. V. Bartlett, V. P. Bhatnagar, M. Bures, J. G. Cordey, G. A. Cottrell, P. A. Dupperex, A. W. Edwards, et al. Stabilization of sawteeth with additional heating in the JET tokamak. *Physical Review Letters*, 60(21):2148, 1988.

[49] A. Sykes and J. A. Wesson. Relaxation instability in tokamaks. *Physical Review Letters*, 37:140–143, 1976.

[50] R. E. Denton, J. F. Drake, and R. G. Kleva. The m=1 convection cell and sawteeth in tokamaks. *Physics of Fluids*, 30:1448–1451, 1987.

[51] G. Vlad and A. Bondeson. Numerical simulations of sawteeth in tokamaks. *Nuclear Fusion*, 29:1139–1152, 1989.

[52] J. A. Breslau, C. R. Sovinec, and S. C. Jardin. An improved tokamak sawtooth benchmark for 3D nonlinear MHD. *Communications in Computational Physics*, 4:647–658, 2008.

[53] S. C. Jardin, N. Ferraro, and I. Krebs. Self-organized stationary states of tokamaks. *Physical Review Letters*, 115(215001), 2015.

[54] M. Wakatani. Non-linear calculation of the m= 1 internal kink instability in current-carrying stellarators. *Nuclear Fusion*, 18(11):1499, 1978.

[55] M. Wakatani, H. Shirai, H. Zushi, H. Kaneko, O. Motojima, T. Obiki, A. Iiyoshi, and K. Uo. Numerical studies of internal disruptions in Heliotron E. *Nuclear Fusion*, 23(12):1669, 1983.

[56] K. McGuire and D. C. Robinson. Sawtooth oscillations in a small tokamak. *Nuclear Fusion*, 19:505–507, 1979.

[57] A. Pochelon, F. Hofmann, H. Reimerde, C. Angioni, R. Behn, R. Duquerroy, I. Furno, P. Gomez, T. P. Goodman, M. A. Henderson, An. Martynov, P. Nikkola, O. Sauter, and A. Sushkov. Plasma shape effects on sawtooth/internal kink stability and plasma shaping using electron cyclotron wave current profile tayloring in TCV. *Nuclear Fusion*, 41:1663–1669, 2001.

[58] M. G. Schlutt, C. C. Hegna, C. R. Sovinec, S. F. Knowlton, and J. D. Hebert. Numerical simulation of current evolution in the Compact Toroidal Hybrid. *Nuclear Fusion*, 52(103023), 2012.

[59] J. D. Hebert. *Simulations of the Compact Toroidal Hybrid Using the Finite Element Extended MHD Code NIMROD*. PhD thesis, Auburn University, 2015.

[60] D. S. Harned and D. D. Schnack. Semi-implicit method for long time scale magnetohydrodynamic computations in three dimensions. *Journal of Computational Physics*, 65:57–70, 1986.

[61] E. J. Caramana. Derivation of implicit difference schemes by the method of differential approximation. *Journal of Computational Physics*, 96:484–493, 1991.

[62] D. S. Harned and W. Kerner. Semi-implicit method for three-dimensional compressible magnetohydrodynamic simulation. *Journal of Computational Physics*, 60:62–75, 1985.

[63] D. D. Schnack, D. C. Barnes, Z. Mikic, D. S. Harned, and E. J. Caramana. Semi-implicit magnetohydrodynamic calculations. *Journal of Computational Physics*, 70:330–354, 1987.

[64] K. Lerbinger and J. F. Luciani. A new semi-implicit method for MHD computations. *Journal of Computational Physics*, 97:444–459, 1991.

[65] G. Strang and G. J. Fix. *An analysis of the finite element method*. Prentice-Hall Englewood Cliffs, NJ, 1973.

[66] G. Karniadakis and S. Sherwin. *Spectral/hp element methods for computational fluid dynamics*. Oxford University Press, 2013.

[67] E. T. Meier, V. S. Lukin, and U. Shumlak. Spectral element spatial discretization error in solving highly anisotropic heat conduction equation. *Computer Physics Communications*, 181:837–841, 2010.

[68] S. Jardin. *Computational methods in plasma physics*. CRC Press, 2010.

[69] Y. Saad and M. H. Schultz. GMRES: A generalized minimal residual algorithm for solving nonsymmetric linear systems. *SIAM Journal on Scientific and Statistical Computing*, 7(3):856–869, 1986.

[70] Carl Sovinec. *A Tutorial on NIMROD Physics Kernel Code Development*. University of Wisconsin Madison, Department of Engineering Physics, 2001. `http://www.cptc.wisc.edu/reports/UW-CPTC_01-3.pdf`.

[71] J. T. Peterson. *Vacuum magnetic flux surface measurements made on the Compact Toroidal Hybrid*. PhD thesis, 2008.

[72] J. L. Herfindal, J. D. Dawson, D. A. Ennis, G. J. Hartwell, S. D. Loch, and D. A. Maurer. Design and initial operation of a two-color soft x-ray camera system on the Compact Toroidal Hybrid experiment. *Review of Scientific Instruments*, 85(11):11D850, 2014.

[73] K. Matsuoka, K. Miyamoto, K. Ohasa, and M. Wakatani. Magnetohydrodynamic instabilities in a current-carrying stellarator. *Nuclear Fusion*, 17(6):1123, 1977.

[74] Y. Nagayama. Tomography of m=1 mode structure in tokamak plasma using least-square-fitting method and fourier-bessel expansions. *Journal of Applied Physics*, 62:2702–2706, 1987.

[75] E. Jones, T. Oliphant, and P. Peterson. SciPy: open source scientific tools for Python. 2014.

[76] J. A. Stillerman, T. W. Fredian, K. A. Klare, and G. Manduchi. MDSplus data acquisition system. *Review of Scientific Instruments*, 68(1):939–942, 1997.

[77] A. P. Navarro, M. A. Ochando, and A. Weller. Equilibrium-based iterative tomography technique for soft x-ray in stellarators. *Plasma Science, IEEE Transactions on*, 19(4):569–579, 1991.

[78] D. Biskamp. *Magnetic Reconnection in Plasmas*. Cambridge Monographs on Plasma Physics. Cambridge University Press, 2000.

[79] H. R. Strauss. Velocity boundary conditions at a tokamak resistive wall. *Physics of Plasmas*, 21(3):032506, 2014.

[80] R. Paccagnella, M. Cavinato, T. Bolzonella, S. Ortolani, G. Pautasso, W. Schneider, V. Lukash, R. Khayrutdinov, and H. R. Strauss. Vertical displacement events simulations for tokamak plasmas. *Fusion Engineering and Design*, 75:589–593, 2005.

[81] H. Childs, E. Brugger, B. Whitlock, J. Meredith, S. Ahern, D. Pugmire, K. Biagas, M. Miller, C. Harrison, G. H. Weber, H. Krishnan, T. Fogal, A. Sanderson, C. Garth, W. E. Bethel, D. Camp, O. Rübel, M. Durant, J. M. Favre, and P. Navrátil. VisIt: An End-User Tool For Visualizing and Analyzing Very Large Data. In *High Performance Visualization–Enabling Extreme-Scale Scientific Insight*, pages 357–372. Oct 2012.

[82] P. Francesco. Viscous resistive magnetic reconnection. *Physics of Fluids*, 30(6):1734–1742, 1987.

[83] J. A. Breslau, S. C. Jardin, and W. Park. Three-dimensional modeling of the sawtooth instability in a small tokamak. *Physics of Plasmas*, 14, 2007.

[84] F. D. Halpern, D. Leblond, H. Lütjens, and J-F Luciani. Oscillation regimes of the internal kink mode in tokamak plasmas. *Plasma Physics and Controlled Fusion*, 53(0115011), 2011.

[85] D. Biskamp and J. F. Drake. Dynamics of the sawtooth collapse in tokamak plasmas. *Physical Review Letters*, 73(7):971, 1994.

[86] A. B. Hassam and Drake J. F. The rippling instability. *Physics of Fluids*, 26(1):133–138, 1983.

[87] D. A. Spong. 3D toroidal physics: Testing the boundaries of symmetry breaking. *Physics of Plasmas*, 22(055602), 2015.

[88] G. L. Jahns, M. Soler, B. V. Waddell, J. D. Callen, and H. R. Hicks. Internal disruptions in tokamaks. *Journal of Computational Physics*, 18:609–628, 1978.

[89] A. Y. Aydemir, J. Y. Kim, B. H. Park, and J. Seol. On resistive magnetohydrodynamic studies of sawtooth oscillations in tokamaks. *Physics of Plasmas*, 22:032304, 2015.

[90] E. T. Meier, V. S. Lukin, and U. Shumlak. Spectral element spatial discretization error in solving highly anisotropic heat conduction equation. *Computer Physics Communications*, 181(5):837–841, 2010.

[91] S. E. Attenberger, W. A. Houlberg, and S. P. Hirshman. Some practical considerations involving spectral representations of 3D plasma equilibria. *Journal of Computational Physics*, 72(2):435–448, 1987.

[92] J. D. Hanson. The virtual-casing principle and helmholtz's theorem. *Plasma Physics and Controlled Fusion*, 57:115006, 2015.

[93] S. A. Lazerson. The virtual-casing principle for 3D toroidal systems. *Plasma Physics and Controlled Fusion*, 54(12):122002, 2012.

[94] T. Hahn. Cuba—a library for multidimensional numerical integration. *Computer Physics Communications*, 176(11):712–713, 2007.

[95] R. H. Pletcher, J. C. Tannehill, and D. Anderson. *Computational fluid mechanics and heat transfer*. CRC Press, 2012.

[96] G. A. Sod. A survey of several finite difference methods for systems of nonlinear hyperbolic conservation laws. *Journal of Computational Physics*, 27(1):1–31, 1978.

[97] NPARC alliance validation archive, shock tube. `http://www.grc.nasa.gov/WWW/wind/valid/stube/stube.html`. Accessed: 2014-04-10.

[98] M. Brio and C. C. Wu. An upwind differencing scheme for the equations of ideal magnetohydrodynamics. *Journal of Computational Physics*, 75(2):400–422, 1988.

Appendices

Appendix A

VMEC

The VMEC model breaks the domain into a plasma region and surrounding vacuum region (Fig. A.1). Equilibria are constrained to have closed nested flux surfaces, even though 3D equilibria do not necessarily have nested flux surfaces. In practice, this turns out to be a reasonable approximation for many applications. The solution fields are represented in flux coordinates, which results in reduced resolution requirements and therefore better computational efficiency. An issue in loading VMEC fields into NIMROD is that the output from VMEC only includes fields in the plasma region of the domain. Loading VMEC fields into NIMROD's computational domain typically requires computation of magnetic fields in the vacuum region.

A.1 Non-orthogonal Coordinates

In an orthogonal coordinate system such as rectangular coordinates or cylindrical coordinates, one describes a given vector $\vec{A}$ in terms of its projections onto the basis vectors,

$$\begin{aligned} \vec{A} &= A_1\vec{e}_1 + A_2\vec{e}_2 + A_3\vec{e}_3 \\ A_1 = \vec{A}\cdot\vec{e}_1,\ A_2 &= \vec{A}\cdot\vec{e}_2,\ A_3 = \vec{A}\cdot\vec{e}_3. \end{aligned} \tag{A.1}$$

This is convenient, because the basis vectors are orthogonal,

$$\begin{aligned} \vec{e}_i &\equiv \frac{\dfrac{\partial\vec{r}}{\partial x^i}}{\left|\dfrac{\partial\vec{r}}{\partial x^i}\right|} \\ \vec{e}_i\cdot\vec{e}_j &= \delta_{ij}. \end{aligned} \tag{A.2}$$

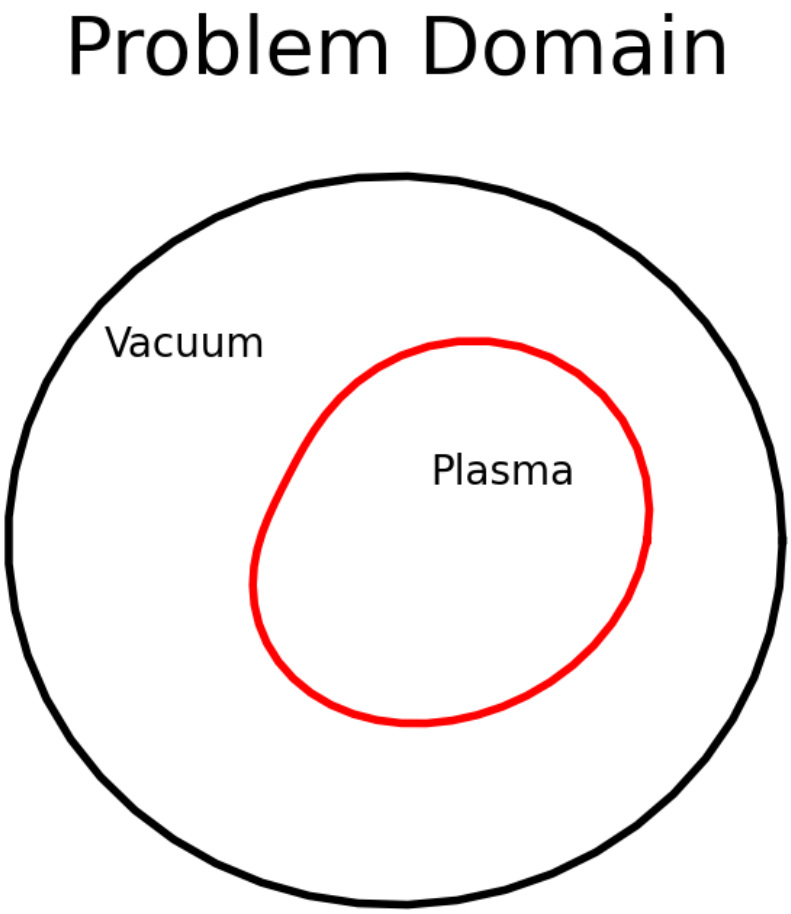

Figure A.1: The VMEC model breaks the domain into a plasma region and a surrounding vacuum region.

If we would like to use a coordinate system in which the magnetic field lines are straight, the basis vectors as defined above will generally not be orthogonal. Such a coordinate system is a non-orthogonal coordinate system. A problem with such a coordinate system is how to represent vectors. The system of representing vectors in terms of their projections onto basis functions as shown above, used for orthogonal coordinate systems, cannot be used because the components of the vector cannot be recovered by projection onto the basis functions. The solution is to use two sets of basis functions which are said to be mutually dual,

$$\vec{e}^{i} \cdot \vec{e}_j = \delta^i_j \tag{A.3}$$

The contravariant basis vectors (having superscripted indices) are defined

$$\begin{aligned} \vec{e}^{1} &= \nabla x^1 \\ \vec{e}^{2} &= \nabla x^2 \\ \vec{e}^{3} &= \nabla x^3. \end{aligned} \tag{A.4}$$

The covariant basis vectors (having subscripted indices) are defined,

$$\begin{aligned} \vec{e}_1 &= \frac{\partial \vec{r}}{\partial x^1} = J\nabla x^2 \times \nabla x^3 = J\vec{e}^{2} \times \vec{e}^{3} \\ \vec{e}_2 &= \frac{\partial \vec{r}}{\partial x^2} = J\nabla x^3 \times \nabla x^1 = J\vec{e}^{3} \times \vec{e}^{1} \\ \vec{e}_3 &= \frac{\partial \vec{r}}{\partial x^3} = J\nabla x^1 \times \nabla x^2 = J\vec{e}^{1} \times \vec{e}^{2}, \end{aligned} \tag{A.5}$$

where J is the determinant of the Jacobian matrix,

$$J = det\Big(\frac{\partial x^i}{\partial \bar{x}^j}\Big) = \frac{1}{\vec{e}^{1} \cdot (\vec{e}^{2} \times \vec{e}^{3})}. \tag{A.6}$$

The "barred" coordinates are often taken to be rectangular Cartesian coordinates.

Each vector is represented with two sets of components. A contravariant set of components which can be obtained by projection onto the contravariant basis, $A^i = \vec{A} \cdot \vec{e}^{i}$, and a

covariant set of components which can be obtained by projection onto the covariant basis vectors $A_i = \vec{A} \cdot \vec{e}_i$. It can be convenient to know that the covariant and contravariant components can be computed directly from the rectangular Cartesian vector components wherever the Jacobian matrix is known by the transformation equations

$$\begin{aligned} A^i &= \frac{\partial x^i}{\partial \bar{x}^j} \bar{A}^j \\ A_i &= \frac{\partial \bar{x}^j}{\partial x^i} \bar{A}^j, \end{aligned} \tag{A.7}$$

where the "hatted" components are the rectangular Cartesian vector components, and summations are implied over repeated indices (Einstein notation). The basis vectors can also be computed from the rectangular Cartesian basis vectors using a similar set of transformation rules involving the Jacobian and inverse Jacobian.

A.1.1 Root Finding for Coordinate Transformations

The transformation from the field aligned coordinates used by VMEC (s, u, v) to cylindrical coordinates (R, ϕ, Z) is given by a Fourier series,

$$\begin{aligned} \phi &= v \\ R(s,u,v) &= \sum_{n,m} R^{(c)}_{is,n,m} cos(mu - nv) + R^{(s)}_{is,n,m} sin(mu - nv) \\ Z(s,u,v) &= \sum_{n,m} Z^{(c)}_{is,n,m} cos(mu - nv) + Z^{(s)}_{is,n,m} sin(mu - nv), \end{aligned} \tag{A.8}$$

where is is an integer index that corresponds to a value of the radial coordinate s. The coefficients $R^{(c)}_{is,n,m}, R^{(s)}_{is,n,m}, Z^{(c)}_{is,n,m}, Z^{(s)}_{is,n,m}$ can be found in the VMEC output file which has a ".wout" extension. The inverse transformation, going from cylindrical coordinates to VMEC coordinates, can be accomplished by employing a root-finding algorithm. This inverse transformation is necessary for both loading initial data into NIMROD and for the soft x-ray tomography program when flux aligned coordinates are used. One might expect the two-dimensional Newton's method to work. However, the pathology at $s = 0$ and the periodic

nature of the u coordinate cause a naive implementation of Newton's method to fail for some points near the origin. A robust root-finding algorithm for this particular problem is given in [91] and is implemented in the VMEC utility library LIBSTELL. It should also noted that, given good initial guesses, some root-finding algorithms included in the SciPy python package work adequately and this approach is used in the modified Fourier-Bessel tomography program.

A.2 Computing Vacuum Magnetic Fields

NIMROD simulations of sawteeth in this work have initial data loaded from VMEC wout files. Typically, the NIMROD domain includes both the VMEC plasma and vacuum regions. In the plasma region part of the domain, one must do an inverse coordinate transformation from cylindrical coordinates to VMEC coordinates at every NIMROD configuration-space grid point. Computing the equilibrium quantities at NIMROD configuration-space grid points typically involves a spline interpolation of the Fourier coefficients for each quantity between VMEC radial grid points. However, VMEC does not have a grid point at the magnetic axis for the magnetic field. Computing the magnetic field at NIMROD grid points near the magnetic axis involves an extrapolation. The routines in LIBSTELL were used to perform all these functions including the inverse transformation, interpolation and extrapolation. It was found that a relatively large VMEC radial resolution, at least 100 points, was necessary for the loaded magnetic fields to be well behaved near the axis.

In the vacuum region part of the NIMROD domain, the magnetic fields must be computed. There are two established methods for computing the magnetic fields in the vacuum region: using a Biot-Savart volume integral and virtual casing [92,93]. The volume integral is easier to implement and the virtual casing offers a more computationally efficient technique to compute the vacuum fields as it only involves a surface integral over the plasma-vacuum interface. In this work, both methods were implemented. The Biot-Savart volume integral implementation uses a simple Riemann integration. For the virtual casing implementation, a

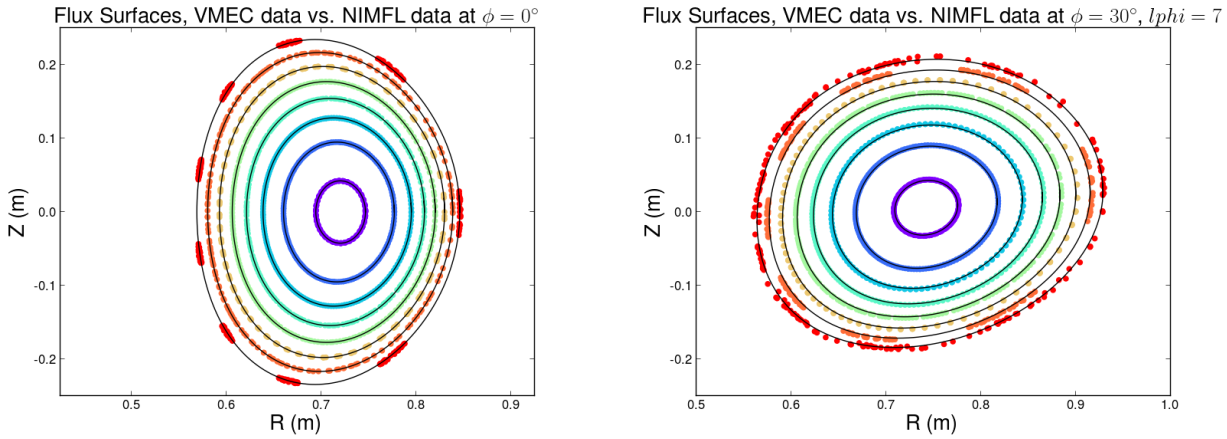

Figure A.2: Poincaré plots (colored dots) of the initial data in NIMROD compared to surfaces of constant toroidal flux from the VMEC data (black lines).

simple Riemann integration over the plasma-vacuum interface does not work well for points near the interface. An efficient, adaptive multidimensional numerical integration routine was needed, so the CUBA library was used [94]. The results of the virtual casing calculations could not be distinguished from converged volume integral calculations.

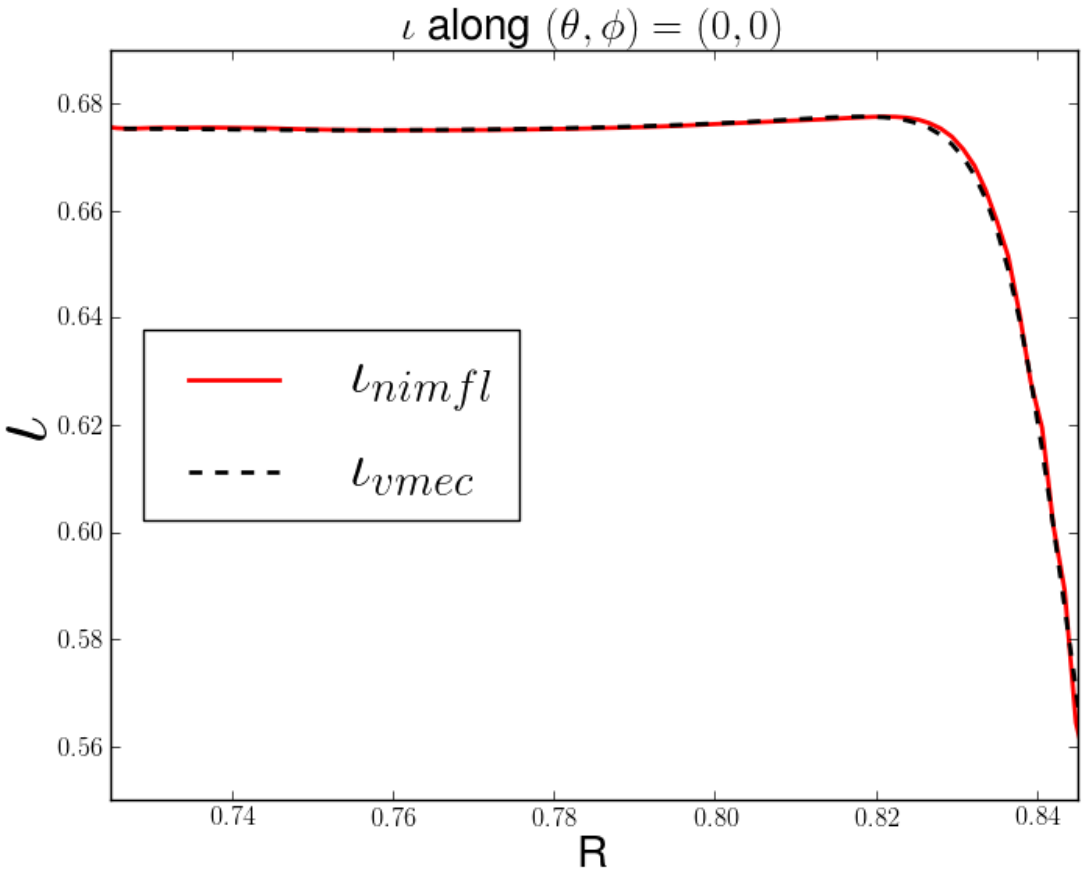

Figure A.3: Rotational transform computed from initial data in NIMROD (red) compared to the rotational transform from the VMEC data.

Appendix B

Fortran Implementation of Semi-Implicit Operator

A Fortran implementation of the semi-implicit operator Eq. 6.2 is listed here. It should be noted that the more optimized implementation of the 3D semi-implicit operator currently in NIMROD is due to Carl Sovinec and includes all the terms from Eq. 1.10. The subroutine compute_3dsi shown here is called from v_aniso_dot.

```
!-----------------------------------------------------------------------
SUBROUTINE compute_3dsi(siop,ncx,ncy,nvc,bigr,rb,tb,mps)
USE io

! Parameters
REAL(r8), DIMENSION(:,:), INTENT(IN) :: bigr
COMPLEX(r8), INTENT(OUT), DIMENSION(3,ncx,ncy,nvc,nmodes) :: siop
TYPE(rblock_type), INTENT(INOUT), TARGET :: rb
TYPE(tblock_type), INTENT(INOUT) :: tb
INTEGER(i4), INTENT(IN) :: mps,ncx,ncy,nvc
! Local variables and constants

COMPLEX(r8), DIMENSION(3,ncx,ncy,nmodes) :: ve,ver,vez,vep
REAL(r8), DIMENSION(:,:,:), POINTER :: alpha,dalpdr,dalpdz
INTEGER(i4) :: ix,iy,im,iv,i1,i2
COMPLEX(r8), DIMENSION(7,ncx,ncy,nmodes) :: afacr,afacz,afacp
REAL(r8), DIMENSION(7,mps,nphi) :: real_afacr,real_afacz,real_afacp
REAL(r8), DIMENSION(3,mps,nphi) :: real_ve,real_ver,real_vez,real_vep
REAL(r8), DIMENSION(3) :: real_dbe

!-----------------------------------------------------------------------
!     Set pointers
!-----------------------------------------------------------------------
! alpha, alphar and alphaz are the poloidal part of the test functions
! (and basis functions since the poloidal dependece is the same) and
! their poloidal derivatives.
CALL generic_alpha_eval(rb,tb%tgeom,10_i4,'rhs',alpha,dalpdr,              &
     &                        dalpdz,1_i4,poly_degree)
! ve, ver and vez are Delta V and its poloidal derivatives.
CALL generic_all_eval(rb%work4,tb%work4,rb%dxdr,rb%dydr,          &
     &                       rb%dxdz,rb%dydz,rb%xg,rb%yg,tb%tgeom,tb%ng,&
     &                       ve,ver,vez,1_i4)

!-----------------------------------------------------------------------
!     3D semi-implicit operator has form,
!     curl( conj(alpha) x B ) . curl( v x B )
!-----------------------------------------------------------------------
```

```
! Compute phi-derivatives (divided by R for toroidal geometry)
IF (geom=='tor') THEN
  DO im=1,nmodes
  DO iy=1,ncy
  DO ix=1,ncx
    IF (keff(im)==0) THEN
      vep(:,ix,iy,im) = 0
    ELSE
      vep(:,ix,iy,im) =  ve(:,ix,iy,im) * (0,1)*keff(im) / bigr(ix,iy)
    ENDIF
  ENDDO
  ENDDO
  ENDDO
ELSE
  DO im=1,nmodes
  DO iy=1,ncy
  DO ix=1,ncx
    IF (keff(im)==0) THEN
      vep(:,ix,iy,im) = 0
    ELSE
      vep(:,ix,iy,im) =  ve(:,ix,iy,im) * (0,1)*keff(im)
    ENDIF
  ENDDO
  ENDDO
  ENDDO
ENDIF

! Transform quantities to real space
CALL fft_nim('inverse',ncx*ncy,mps,nphi,3_i4,ve,real_ve,dealiase)
CALL fft_nim('inverse',ncx*ncy,mps,nphi,3_i4,ver,real_ver,dealiase)
CALL fft_nim('inverse',ncx*ncy,mps,nphi,3_i4,vez,real_vez,dealiase)
CALL fft_nim('inverse',ncx*ncy,mps,nphi,3_i4,vep,real_vep,dealiase)

! real_dbe = curl( v x B )
! Compute by using curl( v x B ) = (B.del)v - (v.del)B - B*div(v)
! This allows us to avoid explicitly taking poloidal derivative of vxB
! Note that before v_ansio_dot is called for the first time,
! the magnetic field and its derivatives from the previous time step
! are transformed to configuration space and stored in the arrays
! real_be, real_ber, real_bez, real_bep.
DO i2=1,nphi
DO i1=1,mps
  ! ----- (B.del)v ----- (without symmetric term that cancels)
  real_dbe(1) = rb%real_be(1,i1,i2)*real_ver(1,i1,i2) +                &
  &  rb%real_be(2,i1,i2)*real_vez(1,i1,i2) + rb%real_be(3,i1,i2)*real_vep(1,i1,i2)
  real_dbe(2) = rb%real_be(1,i1,i2)*real_ver(2,i1,i2) +                &
  &  rb%real_be(2,i1,i2)*real_vez(2,i1,i2) + rb%real_be(3,i1,i2)*real_vep(2,i1,i2)
  real_dbe(3) = rb%real_be(1,i1,i2)*real_ver(3,i1,i2) +                &
  &  rb%real_be(2,i1,i2)*real_vez(3,i1,i2) + rb%real_be(3,i1,i2)*real_vep(3,i1,i2)
  ! IF (geom=='tor') THEN
    real_dbe(3)=real_dbe(3)+rb%real_be_over_r(3,i1,i2)*real_ve(1,i1,i2)
  ! ENDIF

  ! ----- -(v.del)B -----
  real_dbe(1) = real_dbe(1) - real_ve(1,i1,i2)*rb%real_ber(1,i1,i2)-  &
```

```
&  real_ve(2,i1,i2)*rb%real_bez(1,i1,i2) - real_ve(3,i1,i2)*rb%real_bep(1,i1,i2)
real_dbe(2) = real_dbe(2) - real_ve(1,i1,i2)*rb%real_ber(2,i1,i2)-  &
&  real_ve(2,i1,i2)*rb%real_bez(2,i1,i2) - real_ve(3,i1,i2)*rb%real_bep(2,i1,i2)
real_dbe(3) = real_dbe(3) - real_ve(1,i1,i2)*rb%real_ber(3,i1,i2)-  &
&  real_ve(2,i1,i2)*rb%real_bez(3,i1,i2) - real_ve(3,i1,i2)*rb%real_bep(3,i1,i2)
! IF (geom=='tor') THEN
  real_dbe(3)=real_dbe(3)-rb%real_be_over_r(1,i1,i2)*real_ve(3,i1,i2)
! ENDIF

! ----- -B*div(v) -----
real_dbe(1) = real_dbe(1) - rb%real_be(1,i1,i2)*( real_ver(1,i1,i2) +   &
&  real_vez(2,i1,i2) + real_vep(3,i1,i2) )
real_dbe(2) = real_dbe(2) - rb%real_be(2,i1,i2)*( real_ver(1,i1,i2) +   &
&  real_vez(2,i1,i2) + real_vep(3,i1,i2) )
real_dbe(3) = real_dbe(3) - rb%real_be(3,i1,i2)*( real_ver(1,i1,i2) +   &
&  real_vez(2,i1,i2) + real_vep(3,i1,i2) )
! IF (geom=='tor') THEN
  real_dbe(1) = real_dbe(1) - rb%real_be_over_r(1,i1,i2)*real_ve(1,i1,i2)
  real_dbe(2) = real_dbe(2) - rb%real_be_over_r(2,i1,i2)*real_ve(1,i1,i2)
  real_dbe(3) = real_dbe(3) - rb%real_be_over_r(3,i1,i2)*real_ve(1,i1,i2)
! ENDIF

! Compute factors of the test function alpha and its derivatives
! for the equation curl( alpha x B )
! real_afacr - alpha_R equation
! real_afacz - alpha_Z equation
! real_afacp - alpha_phi equation

! R-component
real_afacr(1,i1,i2) = 0 - rb%real_ber(1,i1,i2)                          ! alpha
real_afacr(2,i1,i2) = rb%real_be(2,i1,i2)                               ! dalpdz
real_afacr(3,i1,i2) = rb%real_be(3,i1,i2)                               ! dalpdp
IF (geom=='tor') THEN
  real_afacr(1,i1,i2) = real_afacr(1,i1,i2) - rb%real_be_over_r(1,i1,i2)
ENDIF
! Z-component
real_afacr(4,i1,i2) = 0 - rb%real_ber(2,i1,i2)                          ! alpha
real_afacr(5,i1,i2) = 0 - rb%real_be(2,i1,i2)                           ! dalpdr
IF (geom=='tor') THEN
  real_afacr(4,i1,i2) = real_afacr(4,i1,i2) - rb%real_be_over_r(2,i1,i2)
ENDIF
! phi-component
real_afacr(6,i1,i2) = 0 - rb%real_ber(3,i1,i2)                          ! alpha
real_afacr(7,i1,i2) = 0 - rb%real_be(3,i1,i2)                           ! dalpdr

! R-component
real_afacz(1,i1,i2) = 0 - rb%real_bez(1,i1,i2)                          ! alpha
real_afacz(2,i1,i2) = 0 - rb%real_be(1,i1,i2)                           ! dalpdz
! Z-component
real_afacz(3,i1,i2) = 0 - rb%real_bez(2,i1,i2)                         ! alpha
real_afacz(4,i1,i2) = rb%real_be(1,i1,i2)                              ! dalpdr
real_afacz(5,i1,i2) = rb%real_be(3,i1,i2)                              ! dalpdp
! phi-component
real_afacz(6,i1,i2) = 0 - rb%real_bez(3,i1,i2)                         ! alpha
real_afacz(7,i1,i2) = 0 - rb%real_be(3,i1,i2)                          ! dalpdz
```

```
  ! R-component
  real_afacp(1,i1,i2) = 0 - rb%real_bep(1,i1,i2)                    ! alpha
  real_afacp(2,i1,i2) = 0 - rb%real_be(1,i1,i2)                     ! dalpdp
  ! Z-component
  real_afacp(3,i1,i2) = 0 - rb%real_bep(2,i1,i2)                    ! alpha
  real_afacp(4,i1,i2) = 0 - rb%real_be(2,i1,i2)                     ! dalpdp
  ! phi-component
  real_afacp(5,i1,i2) = 0 - rb%real_bep(3,i1,i2)                    ! alpha
  real_afacp(6,i1,i2) = rb%real_be(1,i1,i2)                         ! dalpdr
  real_afacp(7,i1,i2) = rb%real_be(2,i1,i2)                         ! dalpdz
  IF (geom=='tor') THEN
    real_afacp(5,i1,i2) = real_afacp(5,i1,i2)-rb%real_be_over_r(1,i1,i2)
  ENDIF

  ! Inner product of curl( I x B ) with dbe
  real_afacr(1,i1,i2)=real_afacr(1,i1,i2)*real_dbe(1)
  real_afacr(2,i1,i2)=real_afacr(2,i1,i2)*real_dbe(1)
  real_afacr(3,i1,i2)=real_afacr(3,i1,i2)*real_dbe(1)
  real_afacr(4,i1,i2)=real_afacr(4,i1,i2)*real_dbe(2)
  real_afacr(5,i1,i2)=real_afacr(5,i1,i2)*real_dbe(2)
  real_afacr(6,i1,i2)=real_afacr(6,i1,i2)*real_dbe(3)
  real_afacr(7,i1,i2)=real_afacr(7,i1,i2)*real_dbe(3)

  real_afacz(1,i1,i2)=real_afacz(1,i1,i2)*real_dbe(1)
  real_afacz(2,i1,i2)=real_afacz(2,i1,i2)*real_dbe(1)
  real_afacz(3,i1,i2)=real_afacz(3,i1,i2)*real_dbe(2)
  real_afacz(4,i1,i2)=real_afacz(4,i1,i2)*real_dbe(2)
  real_afacz(5,i1,i2)=real_afacz(5,i1,i2)*real_dbe(2)
  real_afacz(6,i1,i2)=real_afacz(6,i1,i2)*real_dbe(3)
  real_afacz(7,i1,i2)=real_afacz(7,i1,i2)*real_dbe(3)

  real_afacp(1,i1,i2)=real_afacp(1,i1,i2)*real_dbe(1)
  real_afacp(2,i1,i2)=real_afacp(2,i1,i2)*real_dbe(1)
  real_afacp(3,i1,i2)=real_afacp(3,i1,i2)*real_dbe(2)
  real_afacp(4,i1,i2)=real_afacp(4,i1,i2)*real_dbe(2)
  real_afacp(5,i1,i2)=real_afacp(5,i1,i2)*real_dbe(3)
  real_afacp(6,i1,i2)=real_afacp(6,i1,i2)*real_dbe(3)
  real_afacp(7,i1,i2)=real_afacp(7,i1,i2)*real_dbe(3)

ENDDO
ENDDO

! Transform to Fourier space
CALL fft_nim('forward',ncx*ncy,mps,nphi,7_i4,afacr,real_afacr,dealiase)
CALL fft_nim('forward',ncx*ncy,mps,nphi,7_i4,afacz,real_afacz,dealiase)
CALL fft_nim('forward',ncx*ncy,mps,nphi,7_i4,afacp,real_afacp,dealiase)

! Multiply by (conjugated) test function / test function derivative
! factors in Fourier space to compute the contribution to the weighted
! residual integrand. Fourier orthgonality explicitly invoked here.
! The array siop must be added to the array int in v_aniso_dot.
DO im=1,nmodes
DO iv=1,nvc
  siop(1,:,:,iv,im)=alpha(:,:,iv)*(afacr(1,:,:,im)+afacr(4,:,:,im)+afacr(6,:,:,im))
  siop(1,:,:,iv,im)=siop(1,:,:,iv,im)+dalpdr(:,:,iv)*(afacr(5,:,:,im)+afacr(7,:,:,im))
  siop(1,:,:,iv,im)=siop(1,:,:,iv,im)+dalpdz(:,:,iv)*afacr(2,:,:,im)
```

```
  IF (geom=='tor'.AND.keff(im)/=0) THEN
    siop(1,:,:,iv,im)=siop(1,:,:,iv,im)-(0,1)*alpha(:,:,iv)*keff(im)*                    &
&                     afacr(3,:,:,im)/bigr(:,:)
  ELSE IF (keff(im)/=0) THEN
    siop(1,:,:,iv,im)=siop(1,:,:,iv,im)-(0,1)*alpha(:,:,iv)*keff(im)*                    &
&                     afacr(3,:,:,im)
  ENDIF


  siop(2,:,:,iv,im)=alpha(:,:,iv)*(afacz(1,:,:,im)+afacz(3,:,:,im)+afacz(6,:,:,im))
  siop(2,:,:,iv,im)=siop(2,:,:,iv,im)+dalpdr(:,:,iv)*afacz(4,:,:,im)
  siop(2,:,:,iv,im)=siop(2,:,:,iv,im)+dalpdz(:,:,iv)*(afacz(2,:,:,im)+afacz(7,:,:,im))
  IF (geom=='tor'.AND.keff(im)/=0) THEN
    siop(2,:,:,iv,im)=siop(2,:,:,iv,im)-(0,1)*alpha(:,:,iv)*keff(im)*                    &
&                     afacz(5,:,:,im)/bigr(:,:)
  ELSE IF (keff(im)/=0) THEN
    siop(2,:,:,iv,im)=siop(2,:,:,iv,im)-(0,1)*alpha(:,:,iv)*keff(im)*                    &
&                     afacz(5,:,:,im)
  ENDIF

  siop(3,:,:,iv,im)=alpha(:,:,iv)*(afacp(1,:,:,im)+afacp(3,:,:,im)+afacp(5,:,:,im))
  siop(3,:,:,iv,im)=siop(3,:,:,iv,im)+dalpdr(:,:,iv)*afacp(6,:,:,im)
  siop(3,:,:,iv,im)=siop(3,:,:,iv,im)+dalpdz(:,:,iv)*afacp(7,:,:,im)
  IF (geom=='tor'.AND.keff(im)/=0) THEN
    siop(3,:,:,iv,im)=siop(3,:,:,iv,im)-(0,1)*alpha(:,:,iv)*keff(im)*                    &
&                     (afacp(2,:,:,im)+afacp(4,:,:,im))/bigr(:,:)
  ELSE IF (keff(im)/=0) THEN
    siop(3,:,:,iv,im)=siop(3,:,:,iv,im)-(0,1)*alpha(:,:,iv)*keff(im)*                    &
&                     (afacp(2,:,:,im)+afacp(4,:,:,im))
  ENDIF

ENDDO
ENDDO

END SUBROUTINE compute_3dsi
```

Appendix C

Shocktube Problems

One-dimensional shocktube problems are popular as benchmark cases for validating numerical CFD and MHD codes. The initial conditions in a shocktube problem have a single discontinuity in some of the solution fields at the middle of the domain. Shocktube problems are sometimes said to be Riemann problems. There are a class of numerical solvers called Riemann solvers, which essentially treat the solution as a series of piecewise discontinuities and use the exact or an approximate solution to the Riemann problems to advance the solution fields for each time step. Riemann solvers can work quite well for solutions having shocks and rarefactions. Examples of Riemann solvers are the Godunov scheme which uses the exact solution to the Riemann problem, and the Roe scheme which uses an approximate solution to the Riemann problem [95]. Here, NIMROD is used to solve the Sod shocktube and Brio-Wu MHD shocktube problems. This is believed to be the first time NIMROD was used to solve these problems.

C.1 Sod Shocktube

The Sod shocktube is a classic problem for validating CFD codes [96]. The initial conditions (Fig. C.1) are characterized by discontinuous pressure and density. It is customary to use normalized units where the Boltzmann constant and the ion mass are unity $k_B = m_i = 1$. The ratio of specific heats used is $\Gamma = 1.4$ which approximates air, since air is composed of mostly diatomic molecules. Although NIMROD was never intended for either non-MHD CFD problems or for problems involving shocks and rarefactions, a numerical solution very close to the exact solution is recovered. The exact solution is computed iteratively using a program from the NASA website [97].

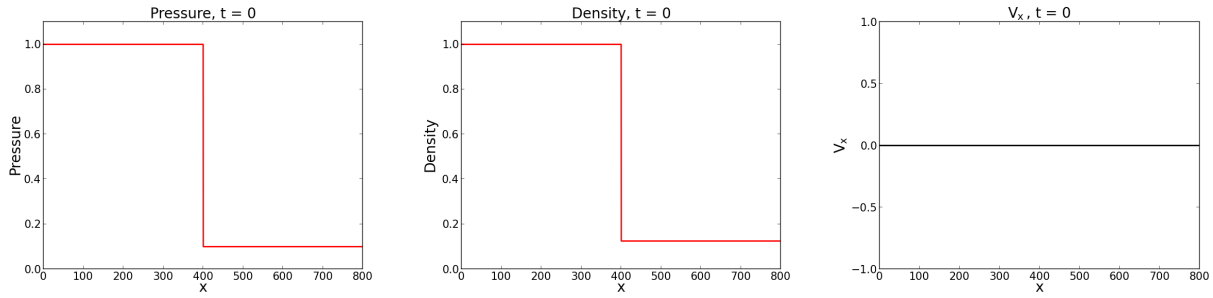

Pressure Density V_x

Figure C.1: Initial conditions for the Sod shocktube.

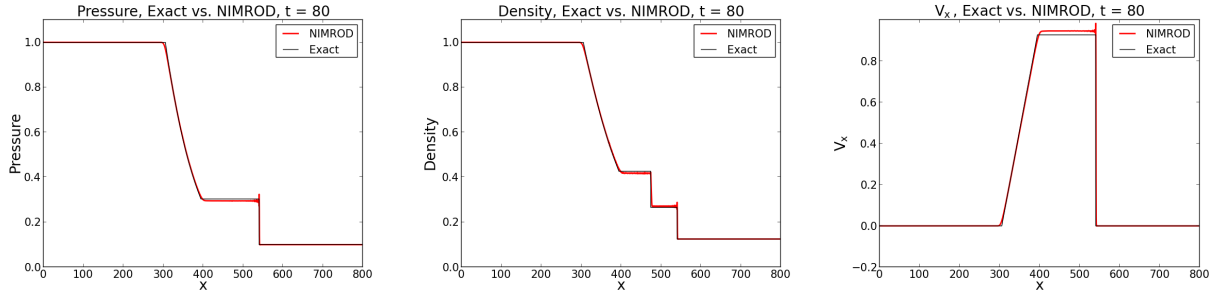

Pressure Density V_x

Figure C.2: Exact solution (black) compared to the NIMROD solution (red) of the Sod shocktube.

Parameter Name	Value
nd_dart_upw	0.01
t_dart_upw	0.01
iso_visc	0.1
elecd	10^5
be0	10^{-15}

Table C.1: Values of key parameters in the NIMROD input file for the Sod shocktube. The parameters *be*0 and *elecd* were set to turn off the electric field and make the fluid a poor electrical conductor because this is not an MHD problem. The parameters *nd_dart_upw* and *t_dart_upw* control the upwind smoothing.

C.2 Brio-Wu MHD Shocktube

The Brio-Wu shocktube problem is an ideal MHD generalization of the Sod shocktube problem [98]. Normalized units are used in which the permeability of free space, the Boltzmann constant and the ion mass are unity, $\mu_0 = k_B = m_i = 1$. The ratio of specific heats $\Gamma = 2$ is used which is different from the Sod shocktube. Additionally the initial conditions, shown in Figure C.3, include discontinuous magnetic fields. The simulations of the Brio-Wu shocktube conducted with NIMROD are two-dimensional, so only the $n = 0$ Fourier number is used, in a rectangular geometry.

Unlike the Sod shocktube problem, the exact solution to the Brio-Wu shocktube problem cannot be computed. Images of the solution from Brio and Wu's original paper, which is generally accepted as a good approximate solution, are situated next to images of the NIMROD solution as a means of comparison in figures C.4 and C.5. The NIMROD solution is surprisingly good, considering NIMROD was never intended to handle problems with shocks and rarefactions. The key to getting good solutions of the shocktube problem is using NIMROD's upwind smoothing. In figure C.6, the NIMROD solution of the Brio-Wu shocktube is shown when upwind smoothing is not used.

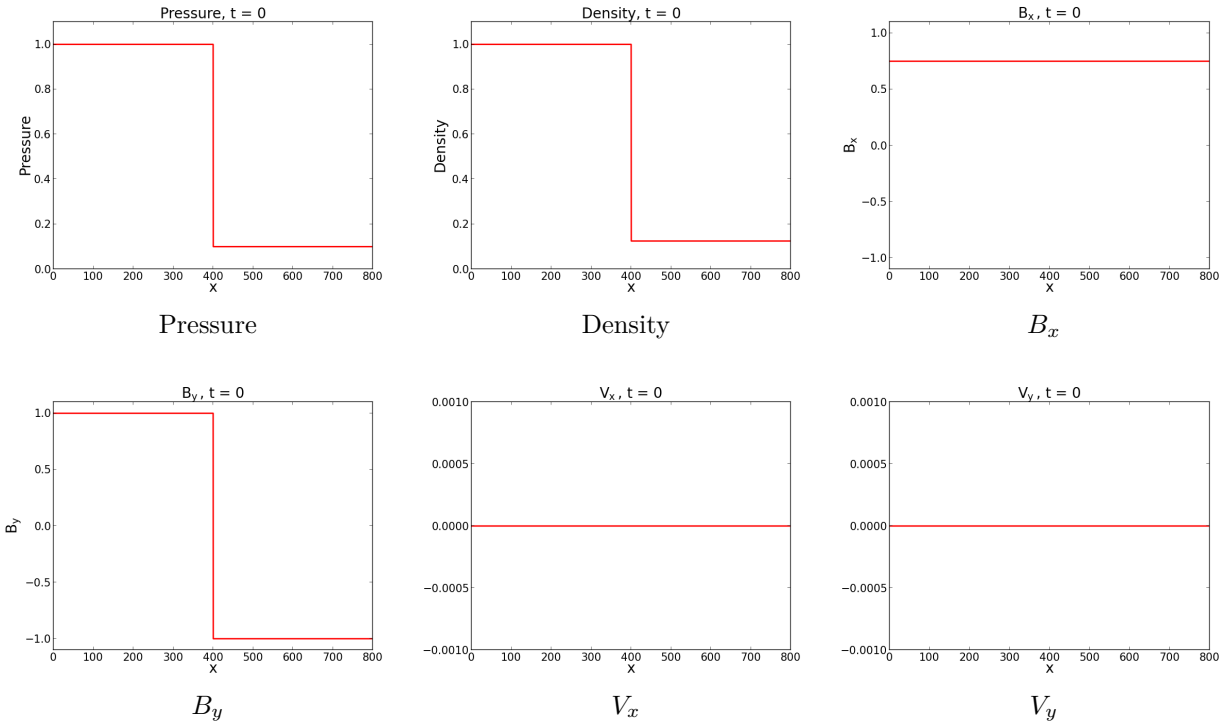

Pressure Density B_x

B_y V_x V_y

Figure C.3: Initial conditions for the Brio-Wu shocktube.

Parameter Name	Value
nd_dart_upw	10
t_dart_upw	10
iso_visc	0.1
elecd	0
poly_degree	3
Δx	1
CFL_{flow}	0.9
lphi	1

Table C.2: Values of key parameters in the NIMROD input file for the Brio-Wu shocktube.

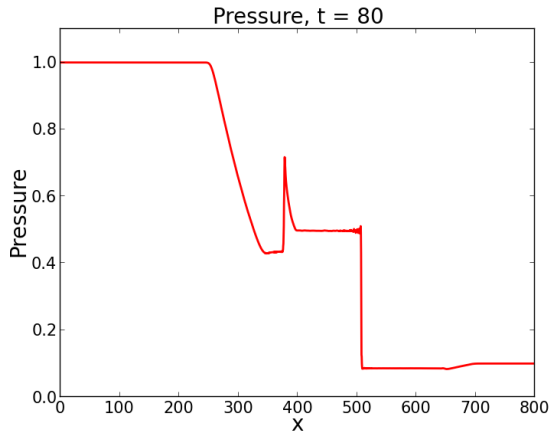

Pressure, NIMROD

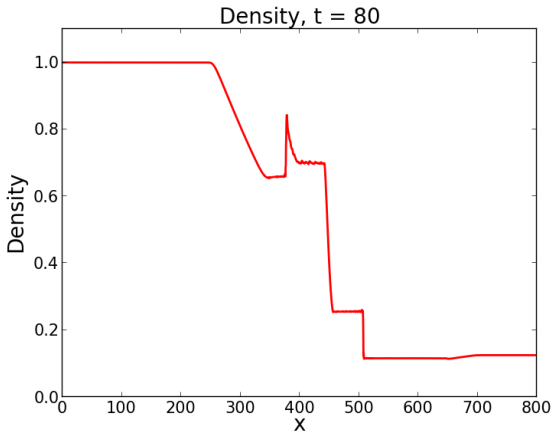

Density, NIMROD

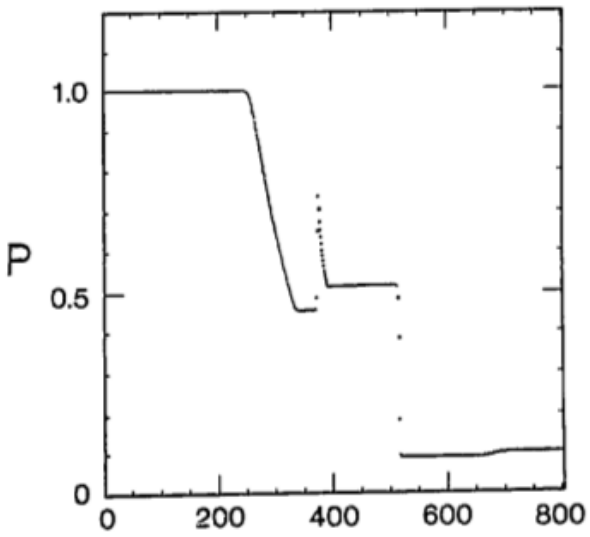

Pressure, Benchmark

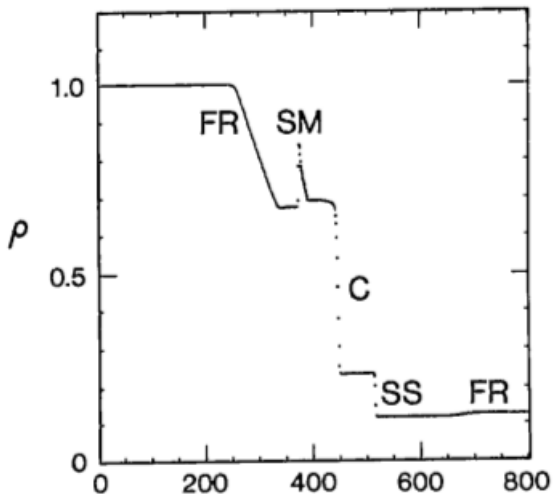

Density, Benchmark

Figure C.4: Brio-Wu shocktube solution from NIMROD (top) compared to the solution from Brio and Wu's original paper (bottom).

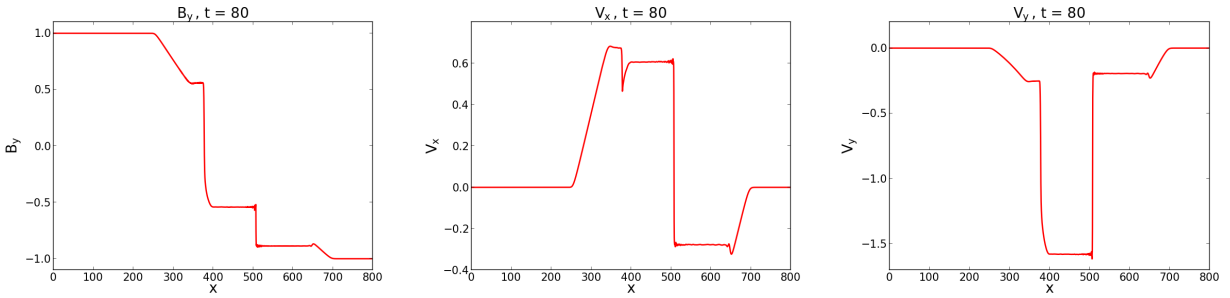

B_y, NIMROD V_x, NIMROD V_y, NIMROD

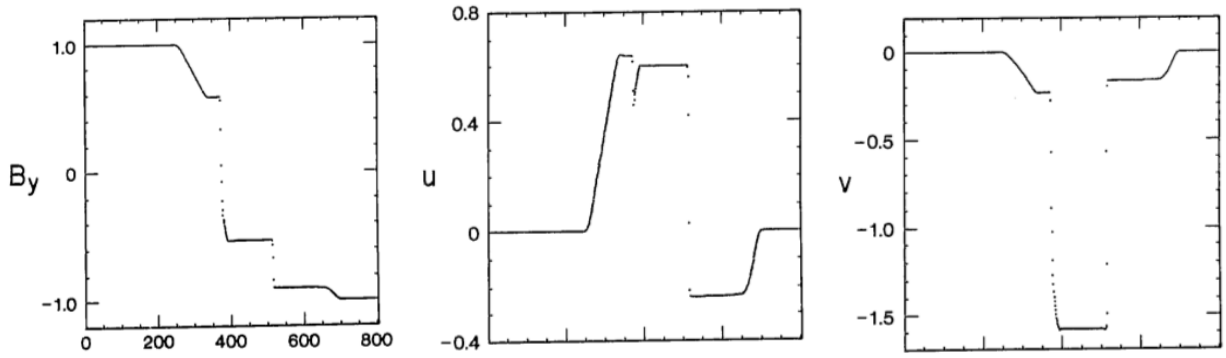

B_y, Benchmark V_x, Benchmark V_y, Benchmark

Figure C.5: Brio-Wu shocktube solution from NIMROD (top) compared to the solution from Brio and Wu's original paper (bottom).

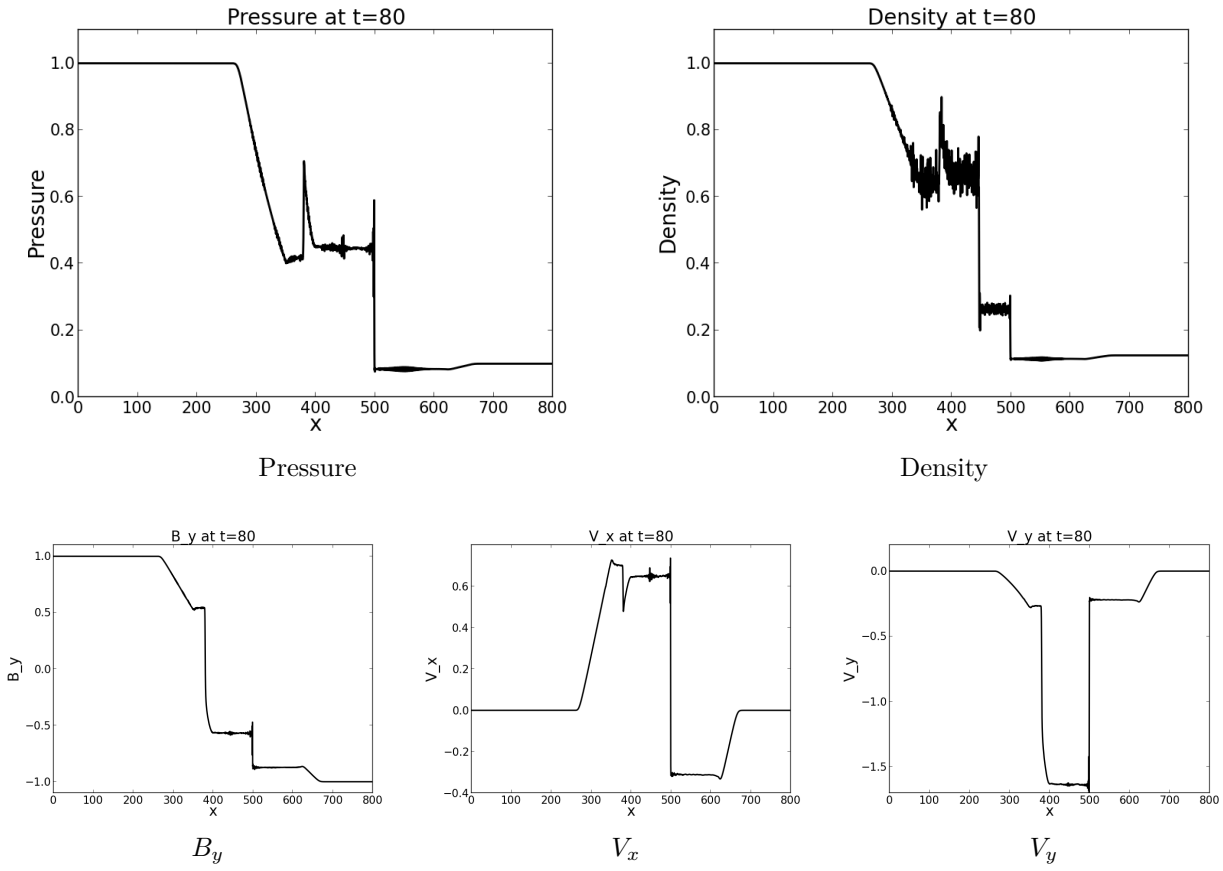

Pressure Density

B_y V_x V_y

Figure C.6: Brio-Wu shocktube solution from NIMROD when upwind smoothing is not used.